Modulated Backscatter for Low-Power High-Bandwidth Communication

by

Stewart J. Thomas

Department of Electrical and Computer Engineering
Duke University

Date: _____

Approved:

_____
Matthew S. Reynolds, Supervisor

_____
Steven Cummer

_____
Jeffrey Krolik

_____
Romit Roy Choudhury

_____
Gregory Durgin

Dissertation submitted in partial fulfillment of the requirements for the degree of Doctor of Philosophy in the Department of Electrical and Computer Engineering in the Graduate School of Duke University
2013

Abstract

Modulated Backscatter for Low-Power High-Bandwidth Communication

by

Stewart J. Thomas

Department of Electrical and Computer Engineering
Duke University

Date: _____

Approved:

_____
Matthew S. Reynolds, Supervisor

_____
Steven Cummer

_____
Jeffrey Krolik

_____
Romit Roy Choudhury

_____
Gregory Durgin

An abstract of a dissertation submitted in partial fulfillment of the requirements for the degree of Doctor of Philosophy in the Department of Electrical and Computer Engineering
in the Graduate School of Duke University
2013

Abstract

This thesis re-examines the physical layer of a communication link in order to increase the energy efficiency of a remote device or sensor. Backscatter modulation allows a remote device to wirelessly telemeter information without operating a traditional transceiver. Instead, a backscatter device leverages a carrier transmitted by an access point or base station.

A low-power multi-state vector backscatter modulation technique is presented where quadrature amplitude modulation (QAM) signalling is generated without running a traditional transceiver. Backscatter QAM allows for significant power savings compared to traditional wireless communication schemes. For example, a device presented in this thesis that implements 16-QAM backscatter modulation is capable of streaming data at 96 Mbps with a radio communication efficiency of 15.5 pJ/bit. This is over 100x lower energy per bit than WiFi (IEEE 802.11).

This work could lead to a new class of high-bandwidth sensors or implantables with power consumption far lower than traditional radios.

To my amazing wife Rebecca who encouraged me to finish and my sweet daughter Daelynn who, by being born, encouraged me to not.

Contents

List of Tables

List of Figures

List of Abbreviations and Symbols

Symbols

$\boldsymbol{E}$	Electric Field
$\boldsymbol{E}^t$	Transmitted electric field
$\boldsymbol{E}^i$	Incident electric field
$\boldsymbol{E}^s$	Scattered electric field
$\boldsymbol{E}^r$	Radiated electric field
$\boldsymbol{E}^i_{\text{rcv}}$	Incident electric field at receiving antenna
$\boldsymbol{E}^s_{\text{Env}}$	Unmodulated scattered field
$\boldsymbol{\ell}_e$	Antenna effective (or equivalent) length
$\boldsymbol{\ell}^b_e$	Antenna effective (or equivalent) length in the back direction
$\boldsymbol{\ell}^s_e$	Antenna effective (or equivalent) length in the scattering direction
$\boldsymbol{\ell}^{\text{tx}}_e$	Antenna effective (or equivalent) length from the transmitting antenna
$\boldsymbol{I}_m$	Conjugate matched antenna currents
$\boldsymbol{I}_r$	Antenna radiating current
$\Delta\boldsymbol{E}^s$	Differential scattered field
$\boldsymbol{E}_{\text{Stationary}}$	Stationary scattered field
$\boldsymbol{E}_{\text{Modulated}}$	Modulated scattered field
$\boldsymbol{E}^{s'}$	Distance attenuated scattered field
$\boldsymbol{E}^{r'}$	Distance attenuated radiated field

$\boldsymbol{I}_m^{'}$	Distance attenuated conjugate matched current
$\boldsymbol{I}_r^{'}$	Distance attenuated radiating current
σ	Radar cross section
P_t	Transmit power
G_t	Transmit antenna gain
G_r	Receive antenna gain
P_r	Receive power
λ	Signal wavelength
Γ^*	Conjugate reflection coefficient
$\Delta\sigma$	Differential radar cross section
β	Wavenumber (propagation constant)
A_s	Antenna effective area
v	Velocity

Abbreviations

AC	alternating current
ADC	analog-to-digital converter
AM	amplitude modulation
AP	access point
ASK	amplitude-shift keying
AWGN	additive white gaussian noise
BER	bit error rate
BPSK	binary phase shift keying
CMOS	complementary metal-oxide-semiconductor
CW	continuous wave

DAC	digital-to-analog converter
DC	direct current
DFE	decision feedback equalizer
EIRP	effective isotropic radiated power
EMG	electromyography
EM	electromagnetic
EVM	error vector magnitude
FM	frequency modulation
FSK	frequency-shift keying
IC	integrated circuit
IF	intermediate frequency
ISI	inter-symbol interference
ISM	Industrial Scientific and Medical
LMS	least mean squares
LMS	least mean squares
LNA	low-noise amplifier
LOS	line of sight
LO	local oscillator
MIMO	multiple-in and multiple-out
MMSE	minimum mean square error
MUX	multiplexer
OFDM	orthogonal frequency division multiplexing
PAM	pulse amplitude modulation
PCB	printed circuit board
PHY	physical layer
PM	phase modulation

PR-ASK	phase-return amplitude shift keying
PSK	phase-shift keying
QAM	quadrature amplitude modulation
RCS	radar cross section
RFID	radio frequency identification
RF	radio-frequency
RLS	recursive least squares
SNR	signal-to-noise ratio
UHF	ultra-high frequency
VNA	vector network analyzer

Acknowledgements

I have been truly blessed to be able to work with and learn from so many people over the last 5 years. I must first start off by thanking my advisor, Matthew S. Reynolds, for his guidance and support during this process. Matt, thank you for the candid discussions, aid in the lab, and helping me run with ideas. I also want to earnestly thank you for the amount of time and effort you've taken in securing grant money for myself and the rest of the lab. I recognize grant money does not grow on trees, but thank you for letting me be tricked into thinking that for our lab it does! Thank you, more importantly, for understanding family (i.e. puppy and baby and wife, and totally in that order) commitments. I really have enjoyed working with you, look forward to more collaboration in the future, and am quite satisfied that I never met your original graduation criterion.

Thank you also to the rest of the lab — Daniel Arnitz, Jordan Besnoff, Joshua Ensworth, Chris Tralie, "Biology" Kris Spaeth, and former member Travis Deyle. Thank you for all of your help, discussions, and code. I especially want to thank Daniel for sharing his hard-earned channel data set, letting me ask endless questions and helping me work through some of the more difficult issues. Daniel, you have been a *tremendous* aid and resource for me, and I would not have been able to complete this work without your help. I also owe a huge debt of gratitude to Arnak Aleksanyan. Arnak, you also were a great source of knowledge and resource for me and are an excellent chip designer. To Daniel and Arnak — I cannot thank you

enough for the help you have provided.

I also want to thank all funding agencies who have supported me (National Science Foundation, Howard Hughes Medical Institute, Ricoh Innovations) as well as my collaborators — Reid Harrison, Anthony Leonardo, Ken Gudan, Sergey Chemishkian, and Jochen Teizer. Thank you so much for your help and support. To everyone involved with the annual IEEE RFID conference, you are an excellent group of reserachers, and every year I look forward to seeing what you are investigating.

Thank you to all my friends at Duke — Zac Harmany, Chris Ratto, Jason Yu, Alex Mrozack, Jonathan Odom, Ken Colwell, all the chefs, and anyone else I've mistakenly forgotten. You guys are great! You're the best group of friends I have ever camped in a tent and RV with for basketball tickets. One day, maybe I'll hang out in Durham after dark with everyone.

Thank you to all my friends at North Carolina State University's (though not part of the name) Graduate IV group. You have been an *amazing* group of friends and source of encouragement, love, and family here in North Carolina. Rebecca and myself would would not be where we are now were it not for your support. I thank each and every one of you — Dr. Brian Gonzales, Laura Fitzwater Gonzales, Dr. Benjamin Redelings, Dr. Eric Butler, Bryan Klingenberg, Susanna Klingenberg, Dr. Erich Bain, Karli Lytle, Dr. Casey Davenport, Keegan Davenport, Emily Ransom, Jared Barnes, Dr. Christina Ludema, Sam Boldenow, David Williams. I cannot say thank you enough for your encouragement and family you have provided me and Rebecca.

Mom and Dad — Thank you for encouraging my academic pursuits. It sure has been a winding road to get here! After (mistakenly?) winning the math award in elementary school, look where I am now: a doctor who still struggles with basic arithmetic! Although you may not have understood the Ph.D. process, you have been there to support me all the way through.

Lastly, but most certainly not least, I want to wholeheartedly thank my amazing and wonderfully intelligent wife, Dr. Rebecca Thomas. She has encouraged me and helped me more than I ever thought possible or will probably know. Thank you for our daughter, and thank you for being so loving. Thank you for putting up with me taking my time and all my annoyances. Thank you for reading this thesis. You are awesome. Two terminal degrees and a combined 21 years of college between us, I can't wait to see where we go next together!

1

Introduction

1.1 The relation between power and communication

Though great advances and innovations over the last 30 years have allowed low-power remote devices and sensors to be deployed in various scenarios, the power efficiency of the wireless uplink has forced a trade off between communication bandwidth and processing power or device lifetime. Low-power wireless communication for remote sensors remains problematic and even somewhat of a misnomer with measured power draw for "ultra-low power" communication subsystems consuming more than 3 mW while transmitting only 50 kbps (60 nJ/bit) [1]. For many remote sensing applications this power demand is excessive due to limitations in the capacity of available on-chip bulk-storage components such as a battery or super-capacitor. This is especially impairing for implantable biosensors where any excess heat generated by the sensor must be kept minimal in order to avoid damaging the surrounding tissue [2].

Poor uplink efficiency has led to a longstanding assumption in the sensor network community that power consumption of a wireless communication subsystem must account for a large portion, if not the majority, of total system power. This

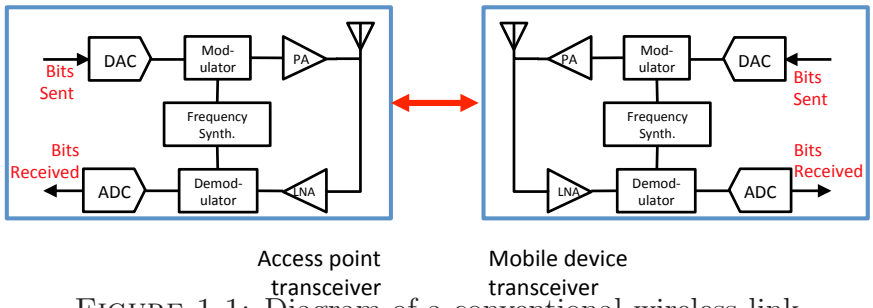

FIGURE 1.1: Diagram of a conventional wireless link

assumption is illustrated by the following excerpts.

> Power consumption can be hence divided into three domains; sensing, communication and data processing ... Of the three domains, **a sensor node expends maximum energy in data communication.** [3, *Emphasis Added*]

> A significant fraction of sensor network research has addressed the problem of energy-efficiency, **primarily by exploiting the fact that computation is many orders of magnitude less expensive than radio communication.** This computation vs. communication trade-off has had a tremendous influence both on algorithm design as well as on sensor network platform design. [4, *Emphasis Added*]

In this thesis, we challenge this assumption by introducing and describing a modulation technique capable of high-bandwidth wireless communication at a fraction of the power-cost of conventional techniques.

1.2 Conventional sensor data links

For low-power sensors and devices, careful power management and power conservation are critical to device lifetime and effectiveness. As outlined above, it is generally

assumed that power consumed by the wireless link will account for a significant portion, if not the majority, of total system power. While complete power breakdowns are rarely provided in the literature, examples are given in Fig. 1.2.

In one simulation of a wireless sensor, the radio subsystem accounted for a majority ($> 50\%$) of the total system power as shown in Fig. 1.2(a) [5]. Even in a modified system explicitly optimized for low-power operation, the simulated power usage by the communication subsystem still accounts for 27% of the total system power (Fig. 1.2(b)). In contrast, the power breakdown for a remote sensor employing low-power communication techniques we will describe shows that wireless communication can be achieved while only using a very small ($\approx 2\%$) portion of the total system power (Fig. 1.2(d)) This is reduced from $\approx 27\%$ in a similar device employing conventional communication methods (Fig. 1.2(c)). To reduce power usage in remote wireless devices, we propose re-examining the physical layer of the wireless link.

1.2.1 Symmetry in conventional radio communication

In general terms, the radio architecture and transceiver design of mobile communication systems have not significantly changed in the last 30+ years. Power and circuit complexity are distributed more or less evenly in the form of each node operating its own transceiver. Therefore, the conventional point-to-point radio link may be considered symmetric with each transceiver being responsible for performing identical tasks at each node. This symmetry is made clear in Fig. 1.1.

The radio transceiver performs two distinct functions — data reception and data transmission. For the transmit chain, a frequency synthesizer generates a high-frequency radio-frequency (RF) signal that is then modulated by a data stream controlled by a digital bit stream passed through a digital-to-analog converter (DAC) block, amplified by a power amplifier and radiated out by an antenna into the propagation channel. Common modulation schemes include amplitude modulation

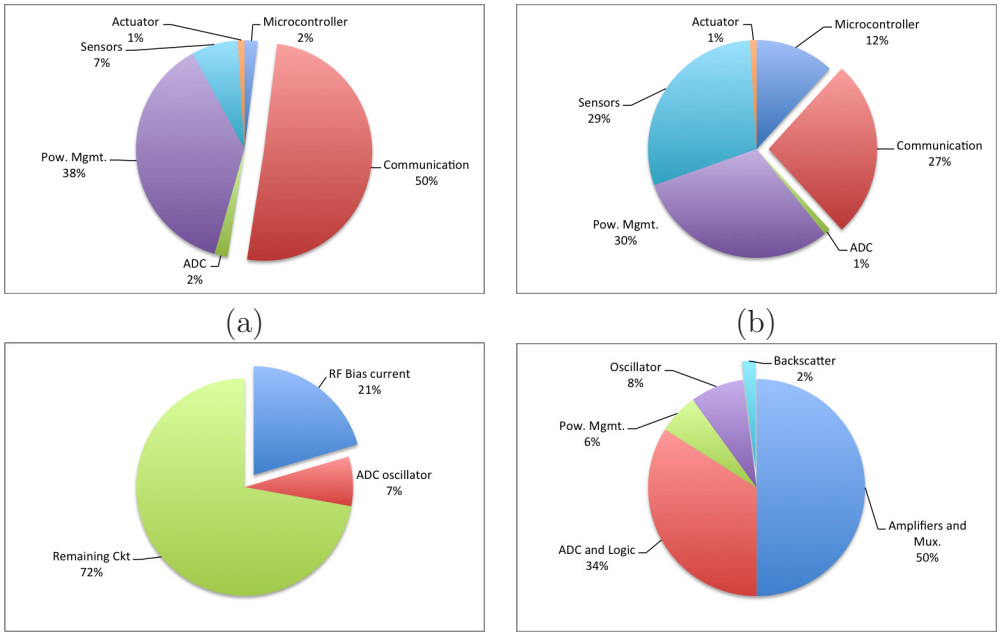

FIGURE 1.2: Power usage by subystem for remote biopotential sensing devices: (A) Simulated device using COTS chips [5], (B) simulated device optimized for low-power [5], (C) Reported values for multi-channel sensor [6], and (D) Measured values of a multi-channel system using radio-frequency (RF) backscatter [7, 8]

(AM), frequency modulation (FM), phase modulation (PM), their keyed counterparts: amplitude-shift keying (ASK), frequency-shift keying (FSK), phase-shift keying (PSK), and combinations including quadrature amplitude modulation (QAM).

For the receive chain, the signal captured by the antenna is passed through a low-noise amplifier (LNA) in order to improve overall signal-to-noise ratio (SNR) performance of the system, next mixed with the local oscillator (LO) output from the frequency synthesizer and then either a direct-to-baseband conversion is performed or the incoming signal is mixed to an intermediate frequency (IF) before conversion to baseband. In either case, the baseband data is filtered and then sampled by an analog-to-digital converter (ADC) for digital baseband processing and data recovery.

Though specific details may vary, the main observation is that this link is *symmetric* in terms of both power and circuit complexity distributed across nodes. Each

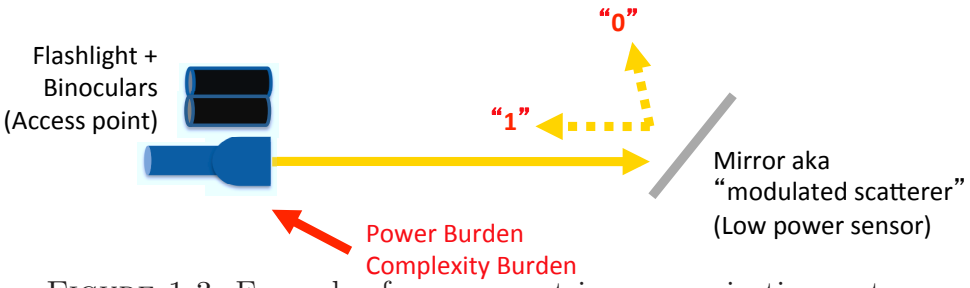

FIGURE 1.3: Example of an asymmetric communication system

individual node operates a local frequency synthesizer used by the transmitting and receiving functions as well as a dedicated power amplifier for wireless data transmission. Stated alternatively, in a typical WiFi (IEEE 802.11) system the (immobile) wireless access point (AP) uses *the same radio architecture or chipset* as a mobile phone or other mobile device. Motivated by the power cost of biasing transistors for ultra-high frequency (UHF) and RF frequencies, we examine the benefits gained for a remote or mobile device when the symmetry for the conventional wireless link is broken. Breaking this symmetry could lead to a reduction in complexity and power consumption of the remote device.

1.3 Asymmetric communication through scattering

Breaking the symmetry of the conventional wireless communication link allows the remote device to offload complexity and power by pushing this burden (power and circuit complexity) onto the access point or base station. Such an asymmetric communication system can be understood through the example of a flashlight and signalling mirror.

Consider two individuals separated by some distance where one person has access to a battery-powered flashlight and the other only has access to a signalling mirror as shown in Fig. 1.3. By aiming the flashlight toward the person holding the mirror and pulsing the light on and off, a coded message (i.e. *Morse code*) may be transmitted. If the light is left on at the end of a message transmission, the signalling mirror

can then be used to alternate between reflecting light toward and away from the person holding the flashlight, allowing for a coded reply. In this scenario, two-way communication is achieved though only one person has access to an illumination source.

Continuing the analogy a bit further, intuition would inform us that as the range is increased, a much stronger flashlight, and perhaps binoculars, would be needed to maintain accurate communication. The key observation is that the person holding the flashlight has absorbed the power and complexity burden while still allowing the second person holding the signalling mirror to communicate. This phenomenon where incident energy is reflected back to a signal source is known as *backscatter*.

1.3.1 Understanding backscatter

Though the principles of backscatter will be examined in detail in Chapter 3 and 4, a brief overview and definition of a backscatter link is provided below.

All reflective objects have a radar cross section (RCS), generally designated as σ. Though the units of RCS are an area with units m^2, RCS is not a physical area, but rather a description of the reflective efficiency of an object. The RCS of an object is defined as the ratio of the incident electric field to the scattered electric field. When the transmitting energy, wavelength, and base station antenna gains are known, the RCS of an object can be used to predict backscatter (return) power or identify an object based on RCS characteristics. This is a basic principle behind all radar systems.

An object with a large RCS will reflect back a large portion of the incident electric field back toward the transmitter/receiver[1]. An object with a small RCS will reflect a small portion of the incident electric field back toward the transmitter/receiver

[1] Commonly, radar systems are monostatic or operate with a sufficiently small bistatic angle such that the receiver and transmitter may be assumed to be co-located. While other bistatic setups exist, this work assumes monostatic operation.

whether by isotropically scattering the received power in all directions or by absorbing the incident energy. A major topic of research in the last century has been investigation of methods to reduce RCS in order to avoid detection by radar systems and remain hidden [9, 10]. However, in this work we are interested in manipulating and controlling the fluctuations of an object's RCS in order to convey information.

1.3.2 Controlled fluctuations to convey information

Traditional radar systems are concerned with interaction between the radar base station and an *un-cooperative* target[2]. A target is illuminated and the reflected signal analyzed to determine the type or shape of the object in view [12,13]. Research has led both to new identification techniques through signal processing and system design as well as materials and geometry engineered for object concealment [10, 11]. Generally speaking, for a radar system the target is *a priori* unknown and is either actively attempting to remain concealed or at best simply not aiding in identification.

A backscatter communication system may be viewed as a radar system where one or more objects in front of the radar's field of view are acting as *cooperative* targets. The objects, by modulating their RCS and therefore reflected field in a structured manner, are attempting to be identified and recognized by the radar base station. Using a mutually agreed upon protocol, the structured, time-varying RCS fluctuations carry the coded message from the object to the radar base station.

1.3.3 Antennas as scatterers

An illustrative backscatter uplink data exchange is shown in Fig. 1.4. In its simplest form, the backscatter tag (also called a transponder) consists of an antenna whose terminals are connected by a single transistor in series with a capacitance. As the transistor switches on and off, the antenna is de-tuned by the capacitive load causing

[2] It should be noted that other types of *un-cooperative* targets have been examined in the literature, but are not considered within the scope of this document[11].

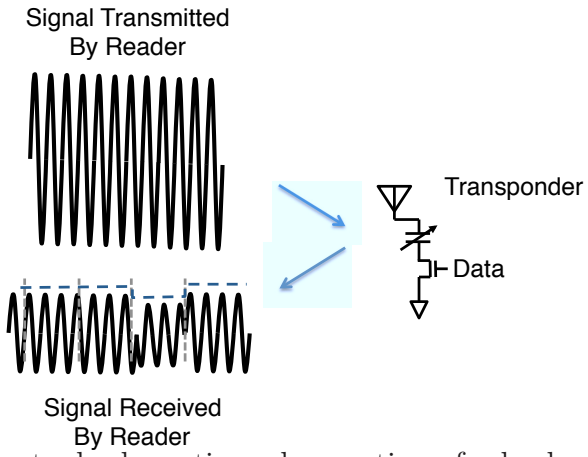

FIGURE 1.4: Conceptual schematic and operation of a backscatter uplink circuit

the RCS to be modulated. The reflected portion of the carrier signal incident on the tag antenna is impressed with an envelope (altering amplitude, phase, or both) carrying the binary backscatter data.

Modulation of the scattered field from the antenna between multiple states using a FET switching at baseband frequencies allows for a transponder to wirelessly telemeter information without operating a local high-frequency synthesizer or power amplifier. In this circuit, it is important to note that no transistors are biased for gain at the carrier (i.e. UHF) frequency allowing for tremendous savings in terms of power.

1.3.4 The backscatter link

A backscatter link is comprised of two or more devices — the reader (also called an interrogator or access point) and the tag. The reader is responsible for transmission of the high-frequency carrier signal to the tag and demodulation of the return signal reflected from the tag. In most protocols, the reader may also send commands for addressing the tags in view [14]. Commands sent to the tags (downlink) are modulated using low data rate ASK, or phase-return amplitude shift keying (PR-ASK) in which a simple envelope detector implemented on the tag is capable of demodulating

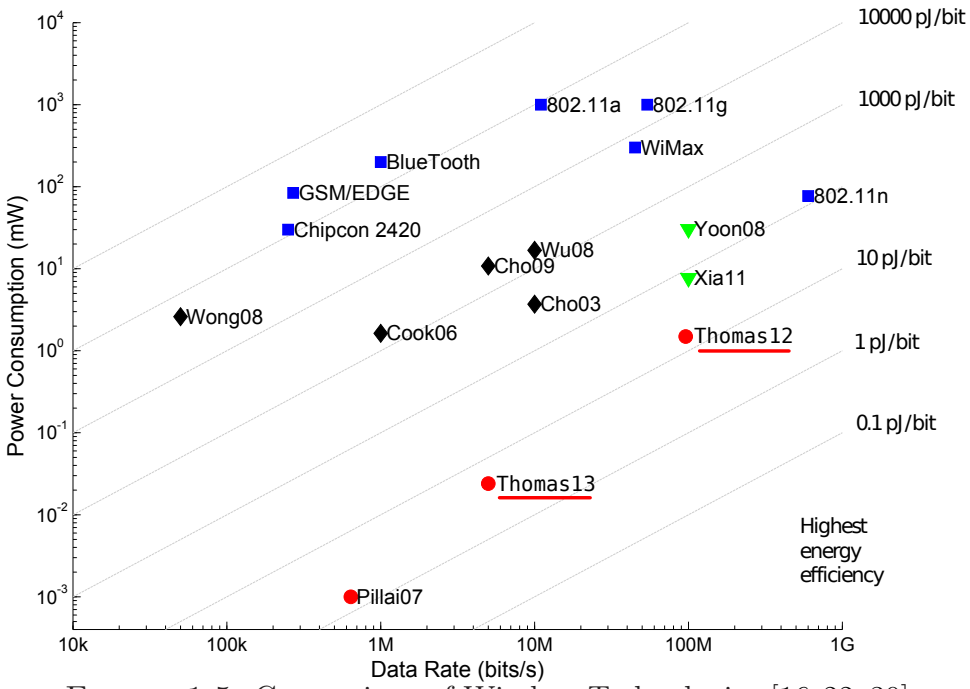

FIGURE 1.5: Comparison of Wireless Technologies [16, 22–30]

and interpreting the downlink signal. Binary signalling from the tag to the reader (uplink) is modulated using binary ASK, PSK, or a combination. Typical data rates, as supported by common backscatter protocols, are 40 kbps but may be as high as 640 kbps. While the backscatter link has been assumed incapable of supporting high data rates or vector signalling modulation schemes, recent work has challenged this assumption [7, 8, 15–17].

1.4 Original contributions

In this work, the physical link will be re-examined and the principles of backscatter communication exploited to design a low-power vector modulator capable of data rates comparable to existing wireless standards. Compared to these standards, however, backscatter modulation requires only a fraction of the communication power. A comparison of wireless communication efficiency is summarized in Fig. 1.5. Using techniques we will describe, uplink data rates comparable IEEE 802.11 (WiFi) are

possible at greatly reduced power levels.

The original contributions of this thesis are:

- A technique for low-power generation of vector modulated backscatter (i.e. QAM backscatter).
- Simulation of M-ary QAM and first experimental confirmation of 4-pulse amplitude modulation (PAM), 4-QAM/4-PSK, 16-QAM modulated backscatter.
- Highest reported to date backscatter data rate (96 Mbps, 15.5 pJ/bit).
- Backscatter based wirelessly powered system for wireless, in-flight multichannel biosignal recording of freely-moving insects.
- First demonstration of a "rich-media" backscatter tag capable of streaming multichannel digital audio and image transmission (5 Mbps, 4 pJ/bit)
- First integrated circuit (IC) implementation of QAM backscatter modulator.
- Demonstrated use of channel equalizer to compensate for frequency deviation, tag motion and channel multipath effects in QAM backscatter communication.

1.5 Document organization

Chapter 1 provides the motivation for low-power communication and offers an introduction to backscatter communication.

Chapter 2 provides a history of backscatter communication and introduction to UHF radio frequency identification (RFID) technology. The field of backscatter communication and wireless sensors is introduced and the state-of-the-art is described.

Chapter 3 provides the theory of modulated backscatter. Starting from a general scattering matrix, the load-dependent scattered field for an antenna is described. This is then used to develop formulas for the differential scattered field as well as

differential RCS which serve as the basic equations for backscatter communication. Multi-state vector backscatter modulation is introduced along with implementation methods for passive R, L, and C lumped element components as well as R and C lumped element components.

In chapter 4, a reader-tag system that forms a backscatter communication link is described. A vector baseband system model is provided that is useful in analyzing channel impairments on the backscatter communication link. The effect of Doppler spread on the communication link is analytically derived and shown graphically. A general backscatter channel gain matrix is provided as well as a description of vector signal quality metrics.

The first experimental demonstration of wideband QAM backscatter from a discrete component device is provided in Chapter 5. This includes results from a 4- and 16-QAM backscatter device. These devices are used to backscatter data at rates of 2 Mbps and 96 Mbps, respectively. These results were measured in an indoor lab environment.

An investigation of channel effects on the receiver performance is provided in Chapter 6. A receiver for backscatter QAM signalling that implements nonlinear adaptive channel equalization is presented. Performance of the system is evaluated in statistically derived, simulated channel models as well multiple locations in a measured indoor backscatter channel. The measured indoor channel includes multipath from highly reflective surfaces, attenuation, and phase rotation. This work shows the real-world feasibility of QAM backscatter.

A fully integrated, high-data rate backscatter sensor is presented in Chapter 7. The fully-passive sensor operates at a data rate of 5 Mbps. The modulator implements the first digitally configurable, user-selectable variable-depth binary backscatter modulator. The system is designed for remote biosignal acquisition from a freely-moving insect. Results from the first experimental wireless transfer of multichannel

high-fidelity digital audio and image over a backscatter link are also presented.

Based on previous results from the discrete component modulator and the single-chip binary backscatter modulator, a single-chip integrated 16-QAM backscatter modulator is designed, fabricated, and tested. In Chapter 8 a description of the integrated chip that includes the QAM modulator is provided. This is the first single-chip implementation of a multi-state backscatter vector modulator. A discussion of the modulator characterization setup and results are provided. Data in chapter confirms feasibility of single-chip backscatter QAM modulators and provides a roadmap for future devices.

Finally, a conclusion and discussion of future work is provided in Chapter 9.

2

Backscatter communication

2.1 History

In the literature, investigation of communication by scattering extends as far back as 1880 when Alexander Graham Bell introduced the *photophone* — a passive device for wireless audio communication [31]. The photophone communicated speech by focusing ambient light onto a mirrored reflecting surface. Sound waves caused the mirror to vibrate and thereby modulated the reflected beam of light. The photophone's companion receiver used a photo-sensitive material to demodulate the incident modulated light beam and drive a time-varying current into an earphone. This resulted in reproduction of the transmitted audio signal. This device was capable of transmitting speech over a reported distance of 214 meters.

This principle of modulated backscatter was then further developed at RF frequencies, replacing Bell's ambient light source with an RF transmitter collocated with the backscatter receiver. A photophone-like device operating in the UHF frequency regime was developed by Leon Theremin in the form of the "Great Seal Bug" [32]. In what is perhaps the first fully-passive long-range audio backscatter system, the Great Seal Bug telemetered speech by using sound waves to deform a thin wall of a cavity

resonator which de-tuned a monopole whip antenna. Although the exact timing of Theremin's invention is unclear in the literature, around the same time, Stockman presented a series of backscatter experiments including audio transfer over microwave frequencies using modulated corner reflectors [33]. In this paper from 1948, it was noted that backscatter was an interesting phenomenon but the author was uncertain of applications where it would be employed. Other early researchers envisioned use of a backscattering device as a covert satellite communications technique [34].

The controlled scattering of electromagnetic fields remained under investigation. The fields scattered from a resonant antenna presented a special case and were analyzed in detail from an analytical perspective [35, 36], a graphical perspective [37], and later expanded to include all possible matching conditions [38]. The general theory of loaded scatterers was also examined [39] as well as research into controlling the scattering of objects by reactive loading [9, 40]. This led to some limited experimental use of modulated scatterers in amplitude and phase field-probing [41].

In the 1970's, the idea of reflected power for communication was revived in the development of an animal tracking system [42]. Though greatly limited by fabrication techniques and leaky diodes available at the time, this work is the first description of a fully passive (battery-free) identification and sensing system. When interrogated by a backpack-mounted reader, tags worn by animals responded with a unique digital code used for identification and tracking as well as analog temperature information embedded in the sub-carrier oscillation frequency.

With the widespread availability and accessibility of complementary metal-oxide-semiconductor (CMOS) processes in the late 1990s–early 2000s, the first single-chip UHF RFID tags were introduced. These early designs formed battery-free devices employing on-chip RF-to-DC converters to supply system operating power and utilized modulated backscatter for wireless transfer of short codes (e.g. 96-bit) containing ID information [43, 44]. Other systems focused on transmission of short

codes for identification along with very low-bandwidth, low-resolution sampled sensor data such as temperature information [45–47]. These systems operated in the UHF, 900 MHz Industrial Scientific and Medical (ISM) band and were later formally defined with an international air protocol, ISO 18000-6C designed for short unique-ID and data block transmission using a randomized algorithm that results in non-deterministic throughput [14, 48].

2.2 UHF RFID

The development of worldwide air protocols governing UHF backscatter communication boosted both industry and academic research. While many devices are designed to support this protocol, a side effect has been that backscatter communication is sometimes *assumed synonymous with* the EPC Class-1 Gen-2 (ISO 18000-6C) UHF RFID air protocols. These assumptions includes protocol mandated bandwidth limitations and other handshake overhead [14].

The modern origins of UHF RFID can be traced to the work by Karthaus and Fischer in one of the first published descriptions of a fully-integrated passive transponder [43]. Though the technology was originally designed to function as a "wireless barcode," the inclusion of sensor data was a natural next step [45]. At its heart, however, existing protocols for UHF RFID air communication were designed for simple object identification *(i.e. identifying cardboard boxes)*.

There exists in the literature a large body of work intending to modify or work within the existing EPC protocol to enable transmission of sensor data. Largely owing to the protocol handshake requirements and randomized slots that result non-determenistic throughpout [48], the sensor data is limited to low bandwidth, low-data rate streams.

The WiSP is a discrete-component device designed to operate with a standard UHF RFID reader while remaining easily programmable and extendable. Its first

application was wireless temperature recording [46]. Other applications include cryptography and secure identification [49] as well as wireless biosignal acquisition [50]. However, a major challenge for researchers using this device is overcoming the limited data throughput. For cryptography applications, there are a limited number of bits available for secure keys. Neuronal signal recordings are limited to transmission of "spike" events as opposed to full-wave neural recordings. More recently, the WiSP has been used to stream recorded audio using an analog microphone and custom protocol [51, 52]. The audio stream is limited to a single channel with sufficient bandwidth for human speech. Furthermore, since the audio is transmitted using analog backscatter, as opposed to digital backscatter, it is susceptible to channel effects and noise.

Other work has also investigated an extension to the standard EPC protocol to support digital audio streaming [53]. In this work, the backscatter link has been ignored for audio data transfer, however, and instead audio information is sent to the remote device in the form of standard ASK modulated data. As such, no audio information is transferred via the backscatter link.

2.3 Low-power wireless communication

A research field where extreme reduction of power consumed by the radio link is important is *remote biosignal acquisition*. While several techniques have been employed with a goal of reducing overall power consumption, generally all rely on very low-duty cycle radio usage. State-of-the-art exemplary systems designed for wireless bio-telemetry in freely-moving small animals consume 1.0 mW of power while recording 2 signals (300Hz – 5.2kHz neural, 20Hz – 280Hz EMG) [6]. The system operates using digital FSK over a 905 MHz link. Other systems employ analog FM modulation to telemeter three neural channels (50Hz – 9.1kHz) while consuming 2.2 mW [54] or telemeter 2 EMG signals (200Hz – 2kHz) while consuming 3.6 mW [55].

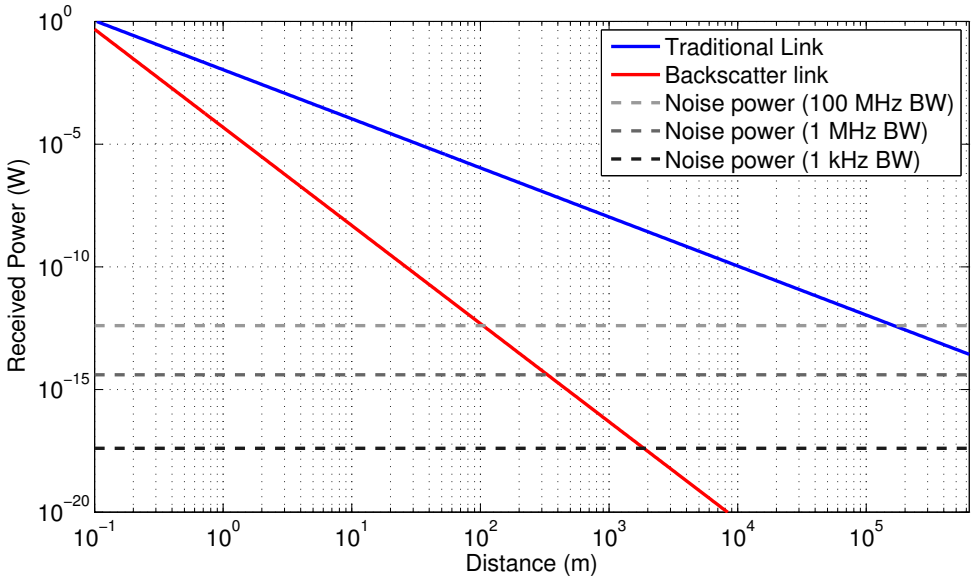

FIGURE 2.1: Range tradeoff in a hypothetical backscatter link versus a hypothetical traditional link

Comparatively, a high-bandwidth backscatter system presented later in this document simultaneously telemeters 10 neural channels (250Hz – 10kHz), 4 EMG (5Hz – 700Hz) and 2 general purpose dc channels while consuming 1.23 mW.

2.4 Range tradeoff in backscatter communication

Signal attenuation, or path loss, in a wireless link occurs as an electromagnetic signal propagates through free space. For single path one way transmissions, the Friis transmission model describes the path loss [56]

$$P_r = \frac{P_t G_t G_r \lambda^2}{(4\pi r)^2} \tag{2.1}$$

where P_r is the received power, P_t is the transmitted power, G_t is the transmitter antenna gain, G_r is the receive antenna gain, λ is the wavelength, and r is the separation distance between the transmit and receive antenna. In a point-to-point link, the one-way attenuation is dominated by the $1/r^2$ term.

However in a backscatter communication link, a round trip path loss is incurred.

The signal is attenuated by both forward (reader to tag) and return (tag to reader) path loss. For a backscatter link, the power at the receiver is described by the radar equation

$$P_r = \frac{P_t G_t G_r \lambda^2 \sigma}{(4\pi)^3 r^4} \tag{2.2}$$

where G_t and G_r are the transmit and receive antenna gains at the reader and σ is the RCS of the tag which describes the portion of incident power that is reflected back to the reader. Contrary to the traditional link, in a backscatter communication system path loss is dominated by the $1/r^4$ term. Comparing the traditional link to a backscatter link, the higher attenuation in a backscatter link results in a lower received power for a given separation distance. This increase in signal attenuation reduces the achievable wireless communication range.

In Fig. 2.1 the received power in a hypothetical traditional link is compared to the received power in a hypothetical backscatter link. For the traditional link, this comparison assumes 6 dBi transmit and receive antennas, 1 W transmitted power, a carrier frequency of 915 MHz, and free space propagation. The separation distance describes the distance between the transmit antenna and the receive antenna. For the backscatter link, this comparison assumes 6 dBi transmit and receive antennas co-located at the reader, 1 W transmitted power, a carrier frequency of 915 MHz and free space propagation. A tag RCS of -12.5 dBsqm models a typical UHF RFID tag [57]. In the backscatter link, separation distance describes the distance between the reader and the tag. Also shown are thermal noise power levels at the receive antenna for 1 kHz, 1 MHz and 100 MHz bandwidths. For a modulation scheme with a spectral efficiency of 1 bps/Hz, these bandwidths correspond to data rates of 1 kbps, 1 Mbps, and 100 Mbps, respectively.

At any given data rate, the signal-to-noise ratio of the backscatter link decreases much faster with distance. Thus a backscatter link has an inherent range disadvan-

tage compared to a traditional link. But, as we will see in the following chapters, the backscatter link has a significant potential power advantage at the tag side of the link. This is an important tradeoff which we exploit in this thesis.

3

Modulated scattering from antennas

In this chapter, the fundamental equations describing the field scattered from an antenna are derived. This equation is then used to compute the differential scattered field. The differential scattered field fully describes the field changes for two separate loads attached to the antenna. This observation is used to generate QAM over a backscatter link. A method for scaling the network to fit within passive network constraints is included. The equations in this chapter may be used to define and build a passive backscatter vector modulator.

Contributions in this chapter:

- Extending binary backscatter modulation to QAM and generalized vector backscatter signaling
- Method for passive implementation of vector backscatter signaling
    1. When resistors, inductors and capacitors are available
    2. When resistors and capacitors are available and inductors are not (e.g. CMOS)

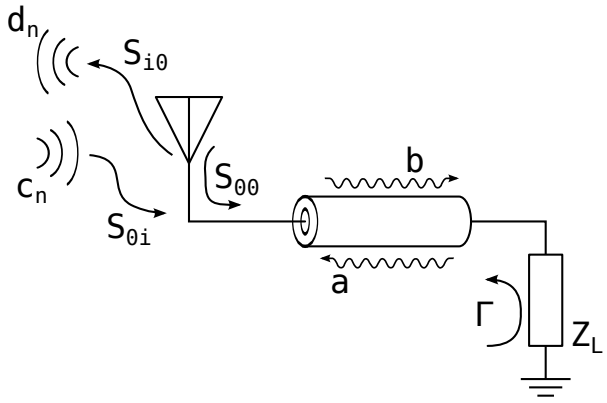

FIGURE 3.1: Antenna with feed line and load shown

3.1 Fields scattered from a loaded antenna

This derivation closely follows that of Collin [36] and Hansen [38] and will use Hansen's notation. An antenna may be viewed as a one port device that converts a single-mode wave in its feed line to a multi-mode wave in space. This is analogous to a single-mode waveguide connected to a multi-mode waveguide through a junction. The antenna is a single port device (though this could be expanded and applied to M antenna elements) attached to a feed line that supports a single-mode and converts the wave into N spatial modes of spherically expanding fields in space. In actuality, countably infinite number of modes may be supported and they need not be assumed spherically expanding. The relation is described by the scattering matrix

$$\begin{bmatrix} b \\ d_1 \\ \vdots \\ d_N \end{bmatrix} = \begin{bmatrix} S_{00} & S_{01} & \dots & S_{0N} \\ S_{10} & S_{11} & & \\ \vdots & & \ddots & \\ S_{N0} & & & S_{NN} \end{bmatrix} \times \begin{bmatrix} a \\ c_1 \\ \vdots \\ c_N \end{bmatrix} \tag{3.1}$$

where d_n and c_n are the respective outgoing (or reflected) and incident electric fields, $\boldsymbol{S}$ is the scattering matrix, and a and b are the complex applied and reflected (from the antenna's perspective) wave amplitudes in the feed line. This is shown in Fig. 3.1.

Radiation only

In the case of radiation only, where the antenna is fed from a generator, the incident wave is $c_n = 0$ and reflected wave in the feed line is $b = S_{00}a$. S_{00} is therefore the reflection coefficient looking into the antenna from the generator (or feed line). In this scenario, the i^{th} radiated mode has amplitude $d_i = S_{i0}a$. It is clear that knowledge of S_{i0} fully describes the antenna radiation pattern and radiated power.

Antenna absent fields and total fields

With the antenna removed, for the incident and reflected fields must remain finite at the origin the incoming and outgoing waves are equivalent ($c_n = d_n$) and the scattering matrix reduces to

$$\boldsymbol{S^0} = \left[\begin{array}{c:cc:c} 0 & 0 & 0 & \\ \hdashline 0 & 1 & 0 & \\ 0 & 0 & 1 & \\ \hdashline & & & \ddots \end{array}\right]. \tag{3.2}$$

The difference between the total fields when the antenna is present and absent will describe the fields scattered by the antenna.

According (3.1), the total fields from the tag are defined as

$$b = S_{00}a + \sum_{m=1}^{N} S_{0m}c_m \tag{3.3}$$

$$d_n = S_{n0}a + \sum_{m=1}^{N} S_{nm}c_m. \tag{3.4}$$

In the case of the antenna being driven by external waves, the incident fields are converted into a single wave amplitude on the feed line. This wave is reflected at the load resulting in $a = \Gamma b$ where Γ is the reflection coefficient looking into the load impedance from the feed line. The reflected feed line voltage is

$$b^s = \frac{\sum_{m=1}^{N} S_{0m}c_m}{1 - \Gamma S_{00}} \tag{3.5}$$

where the b^s represents the scattering wave on the feed line. The total fields become

$$d_n^t = S_{n0}\Gamma b^s + \sum_{m=1}^{N} S_{nm}c_m \tag{3.6}$$

where d_n^t represents a set of equations.

Scattered field

The scattered fields are the difference between the total fields and the antenna absent field. Alternatively, they may be viewed as the difference between the total field and the incident field. Either way, the scattered field is

$$d_n^s = d_n^t - \underbrace{\boldsymbol{S^0} \times \boldsymbol{c_n^0}}_{c_n} \tag{3.7}$$

where $\boldsymbol{c_n^0}$ is a matrix defined as the rightmost side of (3.1) with $a = 0$

$$\boldsymbol{c_n^0} = \begin{bmatrix} 0 \\ c_1 \\ \vdots \\ c_N \end{bmatrix}. \tag{3.8}$$

Rewriting and combining with equations (3.5), (3.6) and (3.7), the field becomes

$$d_n^s = \frac{S_{n0}\Gamma}{1 - \Gamma S_{00}} \sum_{m=1}^{N} S_{0m}c_m + \left(\sum_{m=1}^{N} S_{nm}c_m \right) - c_n \tag{3.9}$$

Shorted antenna and the scattered field

When the antenna is connected to a short-circuit, the reflection coefficient looking into the load is $\Gamma = -1$ and the scattered field is

$$d_n^{s,0} = \frac{-S_{n0}}{1 + S_{00}} \sum_{m=1}^{N} S_{0m}c_m + \left(\sum_{m=1}^{N} S_{nm}c_m \right) - c_n. \tag{3.10}$$

For an antenna radiating, excited by current I_a, the total antenna voltage is

$$a + b = a + aS_{00} \tag{3.11}$$

$$= a(1 + S_{00}) \tag{3.12}$$

$$= I_a Z_a \tag{3.13}$$

where Z_a is the antenna resonant impedance. The applied wave amplitude is then

$$a = \frac{Z_a I_a}{1 + S_{00}}. \tag{3.14}$$

Since the total radiation-only fields are

$$d_n^r = S_{n0} a \tag{3.15}$$

they may rewritten as

$$d_n^r = \frac{I_a Z_a S_{n0}}{1 + S_{00}} \tag{3.16}$$

by including the radiation-only applied wave amplitude. Solving this for S_{n0}

$$\implies S_{n0} = \frac{d_n^r}{I_a Z_a} \left(1 + S_{00}\right). \tag{3.17}$$

The radiated field is used to eliminate the S_{n0} term in the scattered field equation (3.9). After substituting for the term $\left(\sum_{m=1}^{N} S_{nm} c_m\right)$ from the shorted scattered field equation (3.10),

$$\left(\sum_{m=1}^{N} S_{nm} c_m\right) = d_n^{s,0} + \frac{S_{n0}}{1 + S_{00}} \sum_{m=1}^{N} S_{0m} c_m + c_n, \tag{3.18}$$

the scattered field is expressed as

$$d_n^s = d_n^{s,0} + d_n^r \frac{\sum_{m=1}^{N} S_{0m} c_m}{I_a Z_a} \left(\frac{\Gamma + 1}{1 - \Gamma S_{00}}\right). \tag{3.19}$$

The total short-circuit current in the transmission line feeding the antenna is

$$I_0 = \frac{1}{Z_0} \left(a - b\right) = \frac{-2b}{Z_0} \tag{3.20}$$

where $a = \Gamma b$, Z_0 is the feed line characteristic impedance and a and b are subtracted since the currents are flowing in opposing directions. From the initial scattering matrix (3.1), the reflected transmission line current is

$$b = S_{00} a + \sum_{m=1}^{N} S_{0m} c_m. \tag{3.21}$$

For a short-circuit load, the expanded short-circuit current is

$$I_0 = \frac{-2}{Z_0\,(1 + S_{00})} \sum_{m=1}^{N} S_{0m} c_m. \tag{3.22}$$

After substitution, the final scattered field is written as

$$d_n^s = d_n^{s,0} - d_n^r \frac{I_0 Z_0 (1 + S_{00})(\Gamma + 1)}{2 I_a Z_a (1 - \Gamma S_{00})} \tag{3.23}$$

where no normalizing currents or unit current excitation have been assumed as in previous derivations [35, 36, 38].

The antenna reflection coefficient

The reflection coefficient looking into the load from the feed line is

$$\Gamma = \frac{Z_L - Z_0}{Z_L + Z_0} \tag{3.24}$$

for characteristic impedance Z_0. Likewise, the reflection coefficient looking into the antenna from the feed line is

$$S_{00} = \frac{Z_a - Z_0}{Z_a + Z_0} \tag{3.25}$$

where Z_L is the load impedance. After expansion, the right hand side of equation (3.23) is

$$\frac{(1 + S_{00})(\Gamma + 1)}{(1 - \Gamma S_{00})} = \frac{2 Z_a Z_L}{Z_0\,(Z_a + Z_L)}. \tag{3.26}$$

The equation describing the fields scattered from an antenna can now be written as

$$d_n^s = d_n^{s,0} - d_n^r \frac{I_0 Z_L}{I_a\,(Z_a + Z_L)} \tag{3.27}$$

where the scattered field is fully described by the antenna short-circuit scattering and the fields scattered when the antenna is driven by current I_a. The second term

is scaled by the relation between antenna impedance and load impedance. It is worth pointing out that while the transmission line impedance does not appear in this equation, its effect is inherently included in the short-circuit scattered field term and the short-circuit current.

The antenna reflection coefficient, Γ_a, can now be defined as the reflection coefficient looking into the antenna from the load

$$\Gamma_a = \frac{Z_a - Z_L}{Z_a + Z_L}. \tag{3.28}$$

The scattered field becomes

$$d_n^s = d_n^{s,0} - d_n^r \frac{I_0\,(1 - \Gamma_a)}{2I_a}. \tag{3.29}$$

This equation represents a series of equations corresponding to the N expanding spatial modes. Since the electric field is a summation of each of the modes, the electric field scattered from the antenna is

$$\boldsymbol{E}^s = \boldsymbol{E}^s(Z_L = 0) - \boldsymbol{E}^r \frac{I_0\,(1 - \Gamma_a)}{2I_a} \tag{3.30}$$

or

$$\boldsymbol{E}^{\text{scat}} = \boldsymbol{E}_0^{\text{scat}} - \boldsymbol{E}^{\text{ant}} \frac{I_0\,(1 - \Gamma_a)}{2I_a} \tag{3.31}$$

where the fields have been spelled out. This result is equivalent to Collin, and Hansen, and is the basic starting equation of Green.

3.2 The scattered field as a function of load impedance, Z_L

The scattered field in (3.30) assumes knowledge of the incoming (incident) wave spectrum, the short-circuited scattered field, antenna currents, and the antenna radiated fields when excited by current I_a. Hansen simplifies the equation to

$$\frac{\boldsymbol{E}^s}{I_0} = \left[\frac{\boldsymbol{E}^s(Z_L = 0)}{I_0} - \frac{\boldsymbol{E}^r}{2\boldsymbol{I}_r}\right] + \Gamma_a \frac{\boldsymbol{E}^r}{2\boldsymbol{I}_r} \tag{3.32}$$

where radiating current, $\boldsymbol{I}_r$, is equivalent to applied current I_a. In this form, it is clear that the scattered field is composed of a constant term and a term dependent on the load attached to the antenna. Load dependence is contained within Γ_a.

However, the scattered field does not need to be referenced to the short-circuit scattering. Solving equation (3.27) for the conjugate match impedance and eliminating the short-circuit scattered field from equation (3.27), the scattered electric field referenced to the conjugate-match is

$$\boldsymbol{E}^s = \boldsymbol{E}^s(Z_a^*) + \frac{\boldsymbol{E}^r I_0}{I_a}\left[\frac{Z_a^*}{Z_a + Z_a^*} - \frac{Z_L}{Z_a + Z_L}\right]. \tag{3.33}$$

After simplifying,

$$\boldsymbol{E}^s = \boldsymbol{E}^s(Z_a^*) + \frac{\boldsymbol{E}^r I_0 Z_a}{\boldsymbol{I}_r}\frac{Z_a^* - Z_L}{2R_a(Z_a + Z_L)} \tag{3.34}$$

where R_a is the real part of the antenna impedance. Defining the conjugate reflection coefficient

$$\Gamma^* = \frac{Z_a^* - Z_L}{Z_a + Z_L} \tag{3.35}$$

allows the scattered to field to be rewritten

$$\boldsymbol{E}^s = \boldsymbol{E}^s(Z_a^*) + \Gamma^*\frac{\boldsymbol{E}^r I_0 Z_a}{2R_a \boldsymbol{I}_r}. \tag{3.36}$$

The short-circuit current is eliminated from the equation by using the conjugate match current. In the Thévenin equivalent circuit of the receiving antenna, for a constant voltage the loop currents are

$$I_0 Z_a = \boldsymbol{I}_m(Z_a + Z_a^*). \tag{3.37}$$

Substituting this into equation (3.36),

$$\frac{\boldsymbol{E}^s}{\boldsymbol{I}_m} = \frac{\boldsymbol{E}^s(Z_a^*)}{\boldsymbol{I}_m} + \Gamma^*\frac{\boldsymbol{E}^r}{\boldsymbol{I}_r} \tag{3.38}$$

where the scattered electric field from an antenna is fully described by the scattered field in the conjugate match condition and the radiated field. The radiated field is normalized by the radiating current and scaled by the load-dependent conjugate-match reflection coefficient. A similar derivation can also describe the scattered field in terms of the matched load ($Z_L = Z_a$) and match currents. The conjugate match reflection coefficient is equivalent to a $-1 \cdot \rho$ where ρ is the *power reflection coefficient* described by Kurokawa [58]. Both the power reflection coefficient and conjugate match reflection coefficient use a similarly modified Smith chart to graphically describe impedance effects on a circuit.

3.3 Relation of the scattered field to the radar cross section

RCS is defined for any target as the area of an isotropic scatterer which would produce, at the receiver, a power density equal to that of the actual target. This is expressed mathematically as [13]

$$\sigma = \lim_{r\to\infty}\left[4\pi r^2 \frac{P_s}{P_i}\right] \tag{3.39}$$

$$= \lim_{r\to\infty}\left[4\pi r^2 \frac{|E^s|^2}{|E^i|^2}\right] \tag{3.40}$$

where r is the separation distance, $P_{s,i}$ are the scattered and incident power densities at the target, and $E^{s,i}$ are the scattered and incident electric fields at the target. The RCS of a target can be used to predict the amount of received power at the receiver of a radar system using the radar equation.

To determine the RCS of an antenna, first the open circuit voltage induced at the terminals when the antenna is in receiving mode is found

$$V_{OC} = \boldsymbol{\ell}_e \cdot \boldsymbol{E}^i \tag{3.41}$$

where $\boldsymbol{\ell}_e$ is the antenna equivalent length or effective length and $\boldsymbol{E}^i$ is the electric field incident on the antenna. By examining a Thévenin equivalent antenna circuit

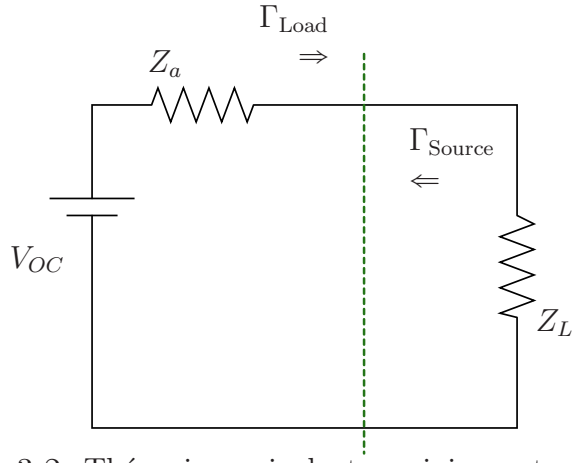

FIGURE 3.2: Thévenin equivalent receiving antenna circuit

comprised of a voltage source (V_{OC}) connected to the antenna impedance (Z_a) and load impedance (Z_L) in series, the current supplied to the load is found. While this Thévenin circuit is not valid as a general model for analyzing the radiated power from antennas, it may be used for predicting the power supplied to the load. The limitations of this model are further discussed in the literature [35,59,60]. When the load impedance is the conjugate of the antenna impedance ($Z_l = Z_a^*$), the current is

$$\begin{aligned} \boldsymbol{I}_m &= \frac{V_{OC}}{2R_a} \\ &= \frac{\boldsymbol{\ell}_e \cdot \boldsymbol{E}^i}{2R_a}, \end{aligned} \tag{3.42}$$

where R_a is the real part of the antenna impedance.

The electric field radiated by the antenna when supplied by current $\boldsymbol{I}_r$ is

$$\boldsymbol{E}^r = -j\frac{\eta}{2\lambda}\boldsymbol{I}_r\boldsymbol{\ell}_e\frac{e^{-j\beta r}}{r} \tag{3.43}$$

where λ is the wavelength, η is the impedance of the medium ($\approx 377\Omega$ for free-space) and β is the propagation constant or wavenumber defined as $2\pi/\lambda$ (assuming freespace propagation and no attenuation).

After substituting, the scattered electric field (3.38) becomes

$$\boldsymbol{E}^s = -j\frac{\eta\boldsymbol{I}_m\boldsymbol{\ell}_e}{2\lambda}\frac{e^{-j\beta r}}{r}\left(1+\Gamma^*\right). \tag{3.44}$$

Combining this result with (3.42), the scattered field is

$$\boldsymbol{E}^s = -j\frac{\eta}{4\lambda R_a}\left(\boldsymbol{\ell}_e \cdot \boldsymbol{E}^i\right)\boldsymbol{\ell}_e \frac{e^{-j\beta r}}{r}\left(1+\Gamma^*\right). \tag{3.45}$$

From the definition given in (3.40), the antenna RCS is

$$\sigma = \frac{\pi\eta^2}{4\lambda^2 R_a^2}\left|1+\Gamma^*\right|\left|\boldsymbol{\ell}_e\right|^2\left|\boldsymbol{\ell}_e \cdot \boldsymbol{E}^i\right|^2 \frac{1}{\left|\boldsymbol{E}^s\right|^2}. \tag{3.46}$$

Relating the antenna equivalent height with the antenna gain G,

$$\left|\ell_e\right|^2 = \frac{G\lambda^2 R_a}{\pi\eta} \tag{3.47}$$

it is seen that

$$\sigma = \frac{\lambda^2}{4\pi}G^2\left|1+\Gamma^*\right|^2 \tag{3.48}$$

where no polarization losses have been assumed and all angles and aspect ratios are either known and accounted for or positioned optimally. This result is equivalent to common textbook definitions but has been derived analytically from the vector scattered field [13].

Confusion exists within the RFID literature concerning the contribution of the structural scattering term possibly due to the simplified antenna RCS form provided in most antenna textbooks (equation (3.48)) without the derivation from the vector scattered field. The observed total backscatter power can be maximized or minimized by choosing a specific load such that the constant structural mode either interferes constructively or destructively with the antenna mode scattering. While this seems straightforward since the argument of the absolute value can be reduced to zero indicating a null-valued RCS, the fields resulting from structural mode scattering are never truly reduced to zero or removed but always present. However, through destructive interference the structural term may be effectively cancelled for a specific antenna load, observation angle and antenna environment.

In the literature, structural mode scattering of RFID tags is typically measured within an anechoic environment. This has contributed to the structural scattering confusion since an anechoic environment is not a realistic model of typical tag environments. Most experimental descriptions are not careful to describe the supporting structure (if any) used in test setups within the anechoic chamber [60–63]. These structures may further affect the scattering measurements of the antenna under test. In practice, RFID tags are not deployed in anechoic environments but in locations with close proximity to other objects and strong multipath interference. Even the idea of 'tagging' objects implies additional environmental scattering influence not considered in the published data listed above.

Whereas the vector electric field equations describe the complete complex value of the field scattered by the tag, the antenna RCS is useful only for scalar power analysis. The exact relationship of amplitude and phase with respect to the incident wave is lost as RCS is defined as a scalar value. Even so, this representation of the signal magnitude is useful for studying the operating range in radar or backscatter communication setup as the greater RCS magnitude, the greater the average power of the antenna scattering term. The importance of the complex nature of the scattered fields is shown next.

3.4 Differential RCS and the differential scattered electric field

The field scattered from an antenna when connected to a load has been previously described. The key observation is that the scattered field is a combination of a constant **load-independent** structural mode scattering term and a **load-dependent** antenna mode scattering term whose electric field varies with load. Choice of the load impedance can greatly affect the magnitude of the observed backscatter [40]. Use of a time-varying load impedance connected to an antenna for communication, as shown in Fig. 3.3, is shown.

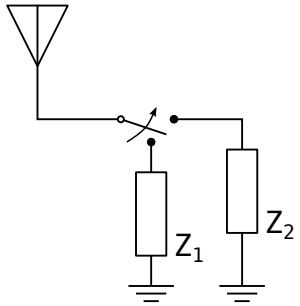

FIGURE 3.3: Binary backscatter signalling circuit

Most analyses of loading an antenna for a desired scattering characteristic tend towards a discussion of average backscattered power by examining the antenna RCS for given loads [9, 10, 37, 39, 40]. However, Green includes an example of selectively loading an illuminated antenna for minimum and maximum backscattered energy in a binary communication scheme by minimizing and maximizing the total RCS of the tag [35]. The RFID community remains interested in similar problems for more efficient use of a backscatter binary communication channel [60, 61, 64].

As previously derived, the expression for the scattered field referenced to the conjugate match (3.38) is dependent on the antenna reflection coefficient Γ^*. In this equation, there are no restrictions on values for the load impedance and all complex relations are retained. As the circuit shown in Fig. 3.3 switches between two different loads connected to the antenna, two conjugate reflection coefficients, Γ_1^* when load Z_1 is connected and Γ_2^* when load Z_2 is connected, are defined from equation (3.35). The time-varying reflection coefficient produces a time-varying binary modulated scattered electric field (i.e. binary signalling) with changes in its real or imaginary part which are detectable at a receiver as binary data. The modulated field, or differential electric field, is defined as the difference between the two scattered field states at the tag

$$\Delta \boldsymbol{E}^s = (\Gamma_1^* - \Gamma_2^*) \frac{\boldsymbol{E}^r \boldsymbol{I}_m}{\boldsymbol{I}_r}. \tag{3.49}$$

The load independent structural term is cancelled in this expression since it is constant in both scattering states.

During data transmission from a scattering antenna, the receiver responds to changes of the scattered field and not solely backscatter magnitude (i.e. $|\Gamma_1^* - \Gamma_2^*|$). This is due in part to the coherent nature of the backscatter system. Distance-dependent phase changes in the received signal are preserved since the phase of the transmitted signal is known exactly at the receiver. This observation is of key importance to understanding backscatter communication.

In the literature, ranging from Green's first analytical description of binary backscatter signaling to recently published articles, phase coherence has been mostly ignored and research has focused on communication via backscatter magnitude change [35, 59, 60]. Work presented in this thesis is the first to challenge this assumption and offer a new paradigm in backscatter communication using vector backscatter signaling [15–17].

However, the differential RCS remains a useful tool for analyzing and comparing the backscatter magnitude difference for two loads and the relation between the differential scattered and the differential RCS is shown. The differential electric scattered field equation (3.49) is rewritten in a form similar to the radiated field expression given in (3.43):

$$\Delta \boldsymbol{E}^s = (\Gamma_1^* - \Gamma_2^*)\frac{-j\eta}{4\lambda R_a}\ell_e(\ell_e \cdot E^i)\frac{e^{-j\beta r}}{r}. \tag{3.50}$$

Applying the definition given in (3.40), the differential RCS is

$$\Delta\text{RCS} = \frac{\pi\eta^2}{4\lambda^2 R_a^2}|\Gamma_1^* - \Gamma_2^*|^2|\ell_e|^2|\ell_e \cdot E^i|^2\frac{1}{|E^i|^2} \tag{3.51}$$

and after simplification is

$$\Delta\sigma = \frac{\lambda^2}{4\pi}G^2|\Gamma_1^* - \Gamma_2^*|^2. \tag{3.52}$$

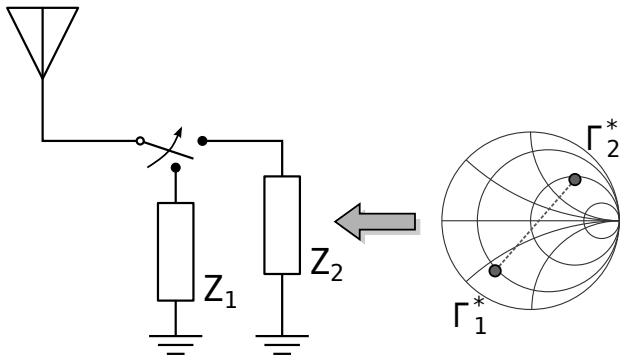

FIGURE 3.4: Relation between load impedance and location on the Smith chart (normalized to the conjugate match)

This assumes no polarization losses and that all angles and aspect ratios are either known and accounted for or positioned optimally. This result which is derived analytically from the vector scattered field is equivalent to the differential RCS first proposed in [59].

The differential RCS is typically employed to determine minimum distance between reflection coefficient symbols (and thereby load impedance values) for achievable communication at a given distance or, conversely, in determining the maximum achievable communication distance for a given symbol spacing under a specified receiver sensitivity. Whereas the differential RCS (3.52) describes the magnitude change between backscatter symbols, the differential scattered field (3.49) more completely describes the electric field changes between symbols by preserving all complex relations.

3.5 Mapping from the Smith chart to the scattered electric field

Green [35] and Tauritz [37] present a graphical method for analyzing the backscatter signal for any load attached to the antenna by using modified Smith charts similar to that of Kurokawa [58].

By rearranging the equation for conjugate reflection coefficient (3.35), the load

impedance is found

$$Z_L\Big|_{Z_a} = \frac{Z_a^* - Z_a\Gamma^*}{1+\Gamma^*}. \tag{3.53}$$

This impedance is referenced to the antenna impedance, as shown in the equation.

This relation provides a means of mapping a reflection coefficient, Γ^*, to a complex impedance, Z_L. For a given carrier frequency, f_c, the impedance may be mapped to a corresponding set of lumped elements to achieve the desired scattered electric field by

$$R\,[\Omega] = \mathrm{Re}\,\{Z_L\} \tag{3.54}$$

and

$$C\,[F] = \frac{1}{2\pi f_c}\cdot\frac{1}{\mathrm{Im}\,\{Z_L\}} \qquad \text{, for } \mathrm{Im}\,\{Z_L\} < 0 \tag{3.55}$$

$$L\,[H] = \frac{1}{2\pi f_c}\cdot\mathrm{Im}\,\{Z_L\} \qquad \text{, for } \mathrm{Im}\,\{Z_L\} \geqslant 0 \tag{3.56}$$

for capacitive or inductive loads. Lumped elements, however, are not the only means of producing the desired impedance and microwave techniques such as open/short stubs and transmission lines yield the same results.

3.6 Mapping the scattered electric field to an IQ signalling constellation

The trigonometric functions sine and cosine are orthogonal over the interval $[0, 2\pi]$, since

$$\int_o^{2\pi} \cos(x)\sin(x)\,\mathrm{d}x = 0, \tag{3.57}$$

and serve as basis functions which allow the real part of the complex exponential (i.e. $\cos x$) and the imaginary part (i.e. $\sin x$) to be independently controlled or

modulated. Commonly, the cosine basis function is called the inphase component and abbreviated I. The sine basis function, being an integrated version of the cosine signal, is called the quadrature component and abbreviated Q. This combination of basis functions forms the IQ plane.

The complex point

$$Z = x + jy \tag{3.58}$$

forms a point in the IQ plane that represents a time-domain signal defined as[1]

$$x(t) = \mathrm{Re}\{Z\}\cos(2\pi f_c t) - \mathrm{Im}\{Z\}\sin(2\pi f_c t) \tag{3.59}$$

for a given carrier frequency.

As a trigonometric identity, the sum of two sinusoids with the same period (or frequency) that differ by a phase shift form a third sinusoid with a new amplitude and phase

$$a\cos(x) + b\sin(x) = \sqrt{a^2 + b^2} \cdot sin(x + \phi) \tag{3.60}$$

where

$$\phi = \mathrm{sgn}(b)\cos^{-1}\left(\frac{a}{\sqrt{a^2 + b^2}}\right) \tag{3.61}$$

with $\mathrm{sgn}(b)$ equal to 1 for $b \geqslant 0$ and to -1 for $b < 0$. It follows that both the amplitude and phase of the signal are controllable by Z. Choosing a set of points in the IQ plane will yield a set of impedances that produce the desired amplitude and phase change in the scattered electric field. This allows for transmission of arbitrary IQ constellation (i.e. the set of points in the complex signaling plane) data. This observation is the basis for vector backscatter modulation.

The scattered electric field is extended such that a signaling constellation in the IQ plane may be defined and mapped to the scattered electric field from an antenna.

[1] In this equation, baseband pulse-shaping is ignored. The pulse-shaping filter ($g_{T_{\{I,Q\}}}$) appears as a time-domain filter applied to the symbols [65, ch. 7].

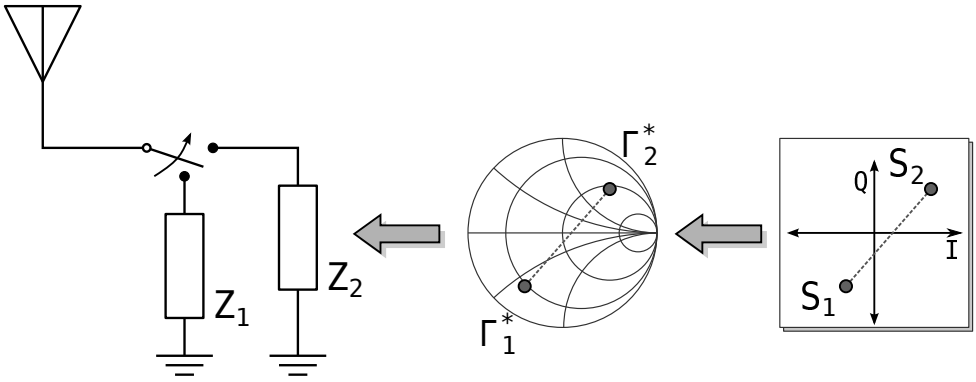

FIGURE 3.5: Relation between load impedance, location on the Smith chart (normalized to the conjugate match) and a signalling constellation in the IQ plane

This mapping is illustrated in Fig. 3.5. A set of points in the IQ plane is defined as a set of complex coordinates

$$\boldsymbol{S} = x_i + jy_i \tag{3.62}$$

where (x_i, y_i) represent the coordinates of a symbol location in IQ space. This set of complex points may be directly applied to the Smith chart.

3.7 Scaling the scattered field to fit passive networks

QAM is an IQ modulation technique that operates by independently modulating the amplitudes of the inphase and the quadrature components. For M total symbols in the constellation, a single point then represents $k = \log_2 M$ bits of information and is termed M-ary QAM. Transmission of QAM generally requires an active transmitter to generate a high-frequency carrier signal and a phase-shifted version that is then actively modulated to generate the M symbols.

Though low-power binary transmission techniques were known, it was not previously considered possible for a low-power device to employ QAM signaling without on-board carrier generation [43, 66]. Following the signal constellation mapping presented in the above sections will result in impedances that require active amplifiers

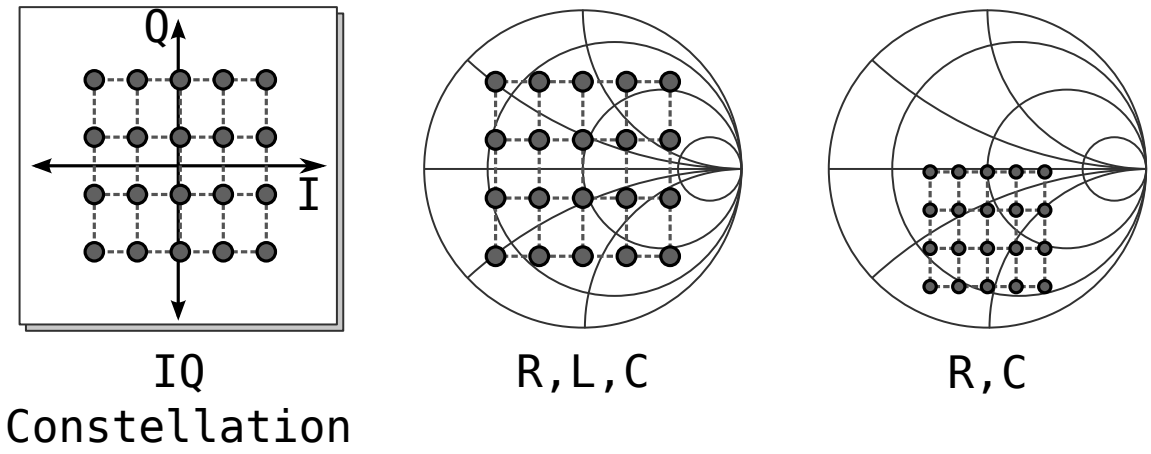

FIGURE 3.6: Signal constellation in IQ plane, scaled for R, L and C components, and scaled for R and C only components

for standard QAM constellations. Therefore, it is important to scale the scattered field to fit within the constraints of passive networks.

For the set of conjugate reflections, Γ^*, to be realizable using passive components, the set of coefficients and symbols must be confined to be within a circle centered on the conjugate match with magnitude $\leqslant 1$. These reflection coefficients are then scaled by a constant $0 < \alpha \leqslant 1$

$$\Gamma_i^* = \alpha \cdot \frac{\boldsymbol{S}_i}{\max|\boldsymbol{S}|}. \tag{3.63}$$

Values of α closer to 1 reflect increasing amounts of the incident electric field back to the transmitter/receiver and result in great backscatter signal strength. In order to maximize communication distance, as the case would be for devices that do not rely on scavenging power from the incident field for circuit system power, α is set to unity. For other devices that make use of RF-to-direct current (DC) conversion circuits, selecting smaller α will yield improved power conversion at the expense of backscatter strength [64, 67].

Most UHF RFID antennas are designed to include significant amounts of inductance in order to conjugate match a capacitive tag IC impedance. For such antennas,

the scaled constellation of equation (3.63) will yield impedances that realizable using only resistive (R) and capacitive (C) components. However, for a resonant antenna with approximately real valued impedance Z_a, the scaled reflection coefficients will require R, L, and C (resistive, inductive, and capacitive) components. This creates a problem for monolithic implementation of the backscatter modulator as standard CMOS processes yield good quality resistors and capacitors but physically large and low-Q inductors. To make CMOS integration feasible through elimination of L components, a further transformation is applied to the constellation to reduce the RLC set of impedances to RC-only by enforcing the constraint that

$$\Gamma^*_{i_{\text{[RC-Only]}}} = \beta\big(\Gamma^*_i - j \min\left[\text{Re}\left\{\Gamma^*\right\}\right]\big) \tag{3.64}$$

where

$$\beta = \frac{\max\left(\text{Im}\left\{Z_L\right\}\right)}{\max\left(\text{Im}\left\{Z_L\right\}\right) - \min\left(\text{Im}\left\{Z_L\right\}\right)}. \tag{3.65}$$

This transformation scales and translates the reflection coefficients by the portion of impedances that lie above the real line in the area that requires inductance. This also has the effect of compressing the IQ vector space of the constellation, reducing the average signal power. The result is a tradeoff of reduced backscatter magnitude compared to the RLC implementation but yielding the desired QAM constellation with a CMOS process.

In Fig. 3.6, the IQ vector constellation is compared to a RLC constellation and RC-only constellation. The constellation has been reduced to fit within the passive network requirements in the RLC case and further reduced and translated in the RC-only case.

3.8 Chapter conclusion

Starting from a general scattering model, the fields scattered from an antenna have been described. The scattered field is the combination of a load-independent struc-

tural scattering term and a load-dependent antenna-mode scattering term. The scattered field differences for two separate loads are fully described by the differential scattered electric field. As opposed to the differential RCS which only describes magnitude difference between states, the differential scattered electric field is complex.

This observation has been used to design a backscatter modulator capable of transmitting QAM signals. A method to scale the signal to fit with passive network constraints has been provided. A method for further scaling the backscatter QAM modulator to be built using only R and C components is also presented. This allows for single-chip integration of the modulator.

4

Backscatter communication links

This chapter defines a reader-tag system and provides insight into how backscatter communication works. An analytical description of Doppler spread in a backscatter context is provided along with mathematical descriptions of the general MIMO backscatter channel.

This chapter provides:

- A baseband signal model of a backscatter communication system
- Description of Doppler spread in backscatter communication
- A general backscatter channel model

4.1 The reader-tag system

A backscatter communication system consists of two key devices. A reader is responsible for generating and transmitting a carrier signal to the tag. A tag, which is in essence an antenna with a time-varying load impedance connected, responds to the incident field by modulating its reflection coefficient. The modulated, scattered

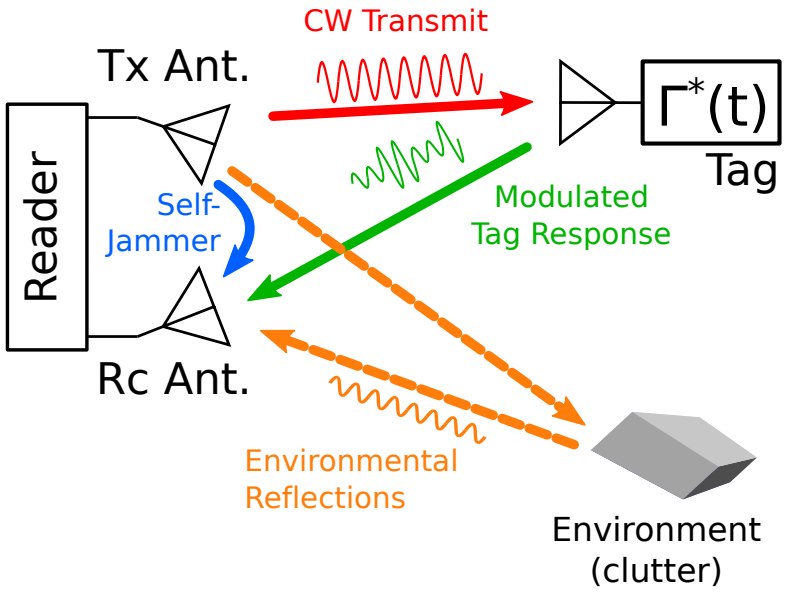

FIGURE 4.1: An exemplary reader tag system showing environmental reflections

field is then detected at the reader's receiver and passed through analog and digital processing components to higher application layers. A typical tag implements an envelope detector to demodulate the downlink (reader-to-tag) data. The reader usually transmits data to the tag by modulating its transmitted signal using simple ASK techniques. For the tag to transmit uplink (tag-to-reader) data, the reader emits a single-tone continuous wave (CW) wave. The tag modulates this incident carrier signal by time-varying changes in the antenna scattering as described in the previous chapter.

A diagram of a simplified reader-tag system is shown in Fig. 4.1. The reader emits a single-tone CW signal which the tag modulates. At the reader's receiver, the fields detected include the self-jammer signal, the modulated tag response and time-delayed environmental reflections. Though the diagram depicts a bistatic receiver setup, in a monostatic setup a self-jammer leakage signal will also appear at the receiver's front end due to non-ideal coupling and isolation of the reader components. The electric

field detected at the receiver is expressed as

$$\boldsymbol{E}^{i}_{\text{rcv}} = \boldsymbol{E}^{s}_{\text{Env}} + \boldsymbol{E}^{s'}(Z_L) + N \tag{4.1}$$

where $\boldsymbol{E}^{s'}(Z_L)$ represents the portion of the field scattered by the tag that is incident on the receiving antenna (i.e. includes scaling and phase shifts due to separation distance modeled by $\exp(j\beta r)/r$ where β is the wavenumber), $\boldsymbol{E}^{s}_{\text{Env}}$ is a vector representing the sum of all possible environment signal paths including multipath reflections from nearby scatterers as well as the self-jammer leakage signal, and N is a noise term which includes thermal noise, noise arising from the object motion, and channel-induced inter-symbol interference (ISI). After expanding this equation, the received field is

$$\boldsymbol{E}^{i}_{\text{rcv}} = \underbrace{\boldsymbol{E}^{s}_{\text{Env}} + \boldsymbol{E}^{s'}(Z^{*}_{a})}_{\boldsymbol{E}_{\text{Stationary}}} + \overbrace{\Gamma^{*}\frac{\boldsymbol{E}^{r'}\boldsymbol{I}'_{m}}{\boldsymbol{I}'_{r}}}^{\boldsymbol{E}_{\text{Modulated}}} + N \tag{4.2}$$

$$= \boldsymbol{E}_{\text{Stationary}} + \boldsymbol{E}_{\text{Modulated}} + N \tag{4.3}$$

where $\boldsymbol{E}_{\text{Stationary}}$ represents the load-independent fields including the summation of all possible multipath signals in the environment as well as the antenna structural scattering term. The $\boldsymbol{E}_{\text{Modulated}}$ field, which is the antenna-mode scattering term detected at the receiver, is determined by the tag load impedance and carries the data payload. In this initial analysis, time-delayed reflections of the modulated tag signal are assumed negligible or ignored. Unless the environment is explicitly known, the interaction between the stationary, or load-independent, fields and the modulated, or load-dependent, fields cannot be accurately predicted *a priori*.

Though the antenna structural scattering is present in the received fields, for a typical environment with strong multipath, the antenna structural scattering cannot be distinguished from the environmental scattering. Additionally, for a receiving system that is alternating current (AC) coupled the $\boldsymbol{E}_{\text{Stationary}}$ term will be rejected

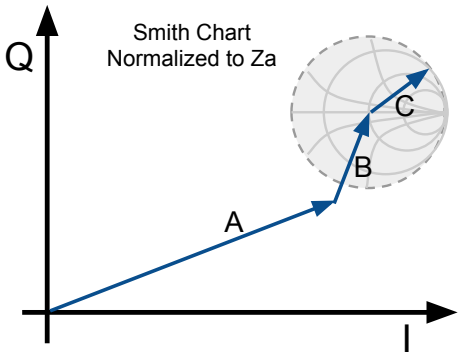

(a)
Received signal at one time instant

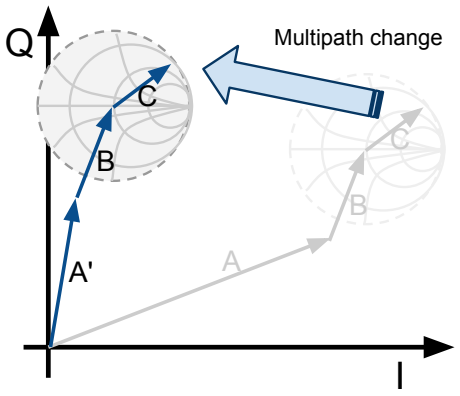

(b)
Received signal after change in environmental multipath

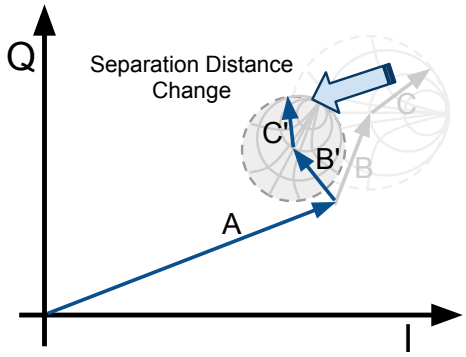

(c)
Received signal after change in separation distance.

FIGURE 4.2: DC coupled demodulated baseband showing the impact of each component of the received backscatter signal under multipath/environmental scattering changes as well as distance change

by the AC coupling or DC offset compensation loop since it is assumed constant for the duration of a symbol period. In this case, the receiver responds only to the load-dependent, modulated component, $\boldsymbol{E}_{\text{Modulated}}$, of the scattered field. While the assumption of maximizing antenna backscatter magnitude through constructive interference from the antenna structural scattering term only holds true for anechoic environments, it is clear that load selection need not be optimized with regard to the structural scattering as previous reports claim [60].

4.1.1 Vector baseband backscatter signaling model

The baseband received fields in equation (4.2) can be expressed as a sum of complex vectors

$$E_{\text{rcv}} = \boldsymbol{A} + \boldsymbol{B} + \boldsymbol{C} + \boldsymbol{N} \tag{4.4}$$

composed of contributions from environmental multipath ($\boldsymbol{A}$), antenna structural scattering ($\boldsymbol{B}$), and load-dependent antenna mode scattering ($\boldsymbol{C}$).

The data rate (and therefore symbol rate) of the modulated backscatter is assumed much greater than the rate of physical motion of the tag or nearby objects, and since load-dependent vector $\boldsymbol{C}$ changes with the data rate, the contributions from environmental scattering and structural scattering ($\boldsymbol{A} + \boldsymbol{B}$, or $\boldsymbol{E}_{\text{Stationary}}$) may be assumed constant during a particular symbol.

The noise-free case is shown in Fig. 4.2(a). In this figure, a modified Smith chart normalized to $Z_0 = Z_a^*$ is positioned to show the range of the load-dependent antenna-mode scattering contribution ($\boldsymbol{C}$) when only passive load impedances are considered.

Movement of nearby scatterers results in a change in the environmental multipath contribution. This translates the tag's total scattered field ($\boldsymbol{B} + \boldsymbol{C}$) within the IQ plane as represented in Fig. 4.2(b). In contrast, as shown in Fig. 4.2(c), changing the tag-to-reader separation distance rotates total scattered field ($\boldsymbol{B} + \boldsymbol{C}$) due to the distance-dependent phase shift and scales it in amplitude because of changing path loss. In the multipath case, as well as the moving-tag case, there is a fixed phase relationship between structural and antenna-mode scattering which is desirable because it preserves the transmitted constellation.

4.2 Doppler spread in backscatter communication

The effect of motion and resulting Doppler spread of the received backscatter signal is now described.

Assuming a time-harmonic (sinusoidal) CW source radiating from the reader shown in Fig. 4.1, and current $\boldsymbol{I}_r$ driving the reader transmit antenna, the resulting far radiated electric field at distance r is

$$\boldsymbol{E}^r = -j\frac{\eta}{2\lambda}\boldsymbol{I}_r\boldsymbol{\ell}_e^{\text{tx}}\frac{e^{-j\beta r}}{r} \tag{4.5}$$

where $\boldsymbol{\ell}_e^{\text{tx}}$ is the effective length of the reader transmit antenna evaluated in the forward direction of the tag.

The electric field incident on the tag antenna ($\boldsymbol{E}^i$) at distance r_{tag} is scattered due to the structural scattering and the antenna-mode scattering. This scattered field is written

$$\boldsymbol{E}^s = \boldsymbol{E}^s(Z_a^*) + \Gamma^*\frac{\boldsymbol{E}^r\boldsymbol{I}_m}{\boldsymbol{I}_r} \tag{4.6}$$

where

$$\boldsymbol{E}^r(Z_a^*) = -j\frac{\eta}{2\lambda}\boldsymbol{I}_m\boldsymbol{\ell}_e^s\frac{e^{j\beta r}}{r}, \tag{4.7}$$

$$\frac{\boldsymbol{E}^r}{\boldsymbol{I}_r} = -j\frac{\eta}{2\lambda}\boldsymbol{\ell}_e^s\frac{e^{j\beta r}}{r} \tag{4.8}$$

and the positive exponential argument in (4.7) indicates a reversal of direction. The tag antenna effective length for scattering is evaluated in the back direction toward the receiver. Typically in backscatter communication applications, a monostatic receiver or receiver with a bistatic angle of zero (co-located transmitter and receiver) is assumed and the incident angle and scattering angle to the receiver is equivalent.

As previously found by Thévenin analysis, the conjugate current is written as

$\boldsymbol{I}_m = \frac{\boldsymbol{\ell}_e^b \cdot \boldsymbol{E}^i}{2R_a}$. Combining, the scattered field is then

$$\boldsymbol{E}^s = -j\frac{\eta}{2\lambda}\left(\frac{\boldsymbol{\ell}_e^b \cdot \boldsymbol{E}^i}{2R_a}\right)\boldsymbol{\ell}_e^s \frac{e^{j\beta r}}{r}\left(1+\Gamma^*\right). \tag{4.9}$$

Expanding this equation with the incident field $\boldsymbol{E}^i$

$$\boldsymbol{E}^s = \frac{-\eta^2}{4r^2\lambda^2}\frac{\boldsymbol{I}_r \boldsymbol{\ell}_e^{\text{tx}} |\boldsymbol{\ell}_e^b|^2}{2R_a}\left(1+\Gamma^*\right) \tag{4.10}$$

where radial path r defines the reader-to-tag separation distance and the tag antenna effective length in the forward direction, $\boldsymbol{\ell}_e^s$, and back direction, $\boldsymbol{\ell}_e^b$, are equal. This assumes a monostatic or co-located bistatic with zero bistatic angle radar setup. The induced voltage on the terminals of the receiving antenna at the reader is

$$V_{rc} = \frac{-\eta^2}{4r^2\lambda^2}\frac{\boldsymbol{I}_r \boldsymbol{\ell}_e^{\text{rcv}} \boldsymbol{\ell}_e^{\text{tx}} |\boldsymbol{\ell}_e^b|^2}{2R_a}\left(1+\Gamma^*\right) \tag{4.11}$$

$$= \boldsymbol{K}(\boldsymbol{r})\left(1+\Gamma^*\right) \tag{4.12}$$

where $\boldsymbol{\ell}_e^{\text{rcv}}$, $\boldsymbol{\ell}_e^{\text{tx}}$, and $\boldsymbol{\ell}_e^b$ are the antenna effective lengths of the reader receiving antenna evaluated in the direction of the backscattering tag, the reader transmitting antenna evaluated in the direction of the backscattering tag, and the tag antenna evaluated in the direction of the reader. At distance r, the left half of the expression will be constant and is represented as a constant complex vector $\boldsymbol{K}(\boldsymbol{r})$.

In the receiver, a direct to baseband conversion is performed by mixing a copy of the transmit signal (LO) with the received signal as shown in Fig. 4.3. This produces a copy of the tag baseband signal at DC and twice the carrier frequency. A low-pass filter designed to reject data above the carrier signal removes these components from the baseband signal. The signal output from the frequency mixing operation are

$$V_{\text{out}} = \left[\boldsymbol{K}'(r)\left(1+\Gamma^*\right)\right]\left(1+e^{j2\omega t}\right) \tag{4.13}$$

and

$$V_{\text{bb}} = \boldsymbol{K}'(r)\left(1+\Gamma^*\right) \tag{4.14}$$

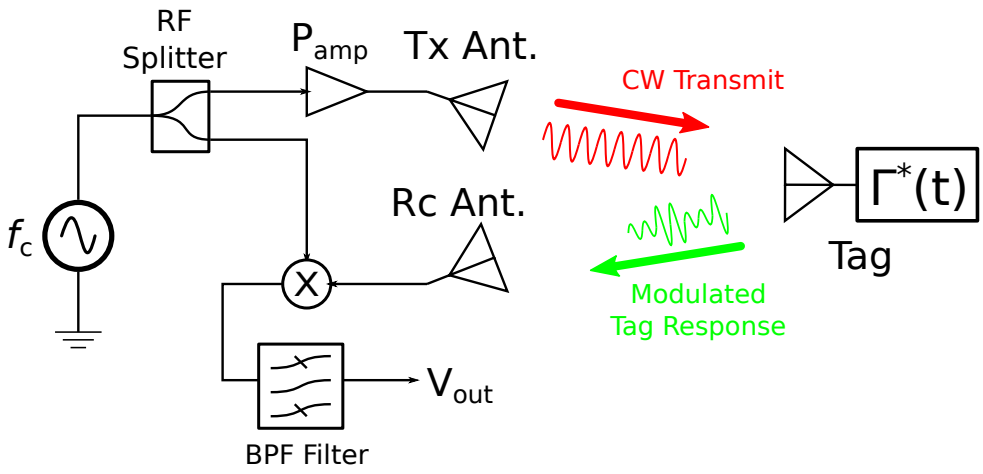

FIGURE 4.3: Basic backscatter communication system (multipath reflections not shown)

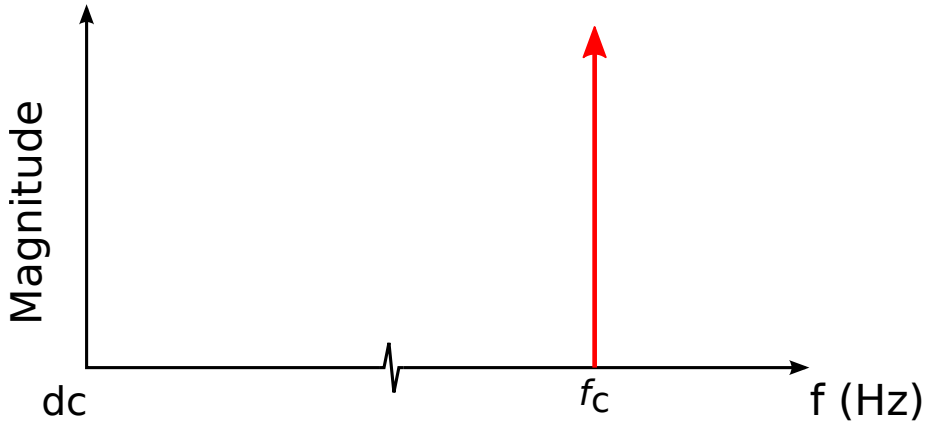

FIGURE 4.4: Frequency domain view of CW transmit signal

after low-pass filtering has been applied, where $\boldsymbol{K}'(r)$ is a complex constant determined by the LO amplitude and phase relative to the incident field that scales the vector $\boldsymbol{K}(\boldsymbol{r})$. This value is constant for a given distance. When a time-varying input is applied to the complex reflection coefficient Γ^*, this data message can be recovered from the V_{bb} voltage, though at a DC offset of $\boldsymbol{K}$.

One potential source of error in the received data is physical motion causing a Doppler shift. Assuming a stationary reader and a tag moving radially outward at

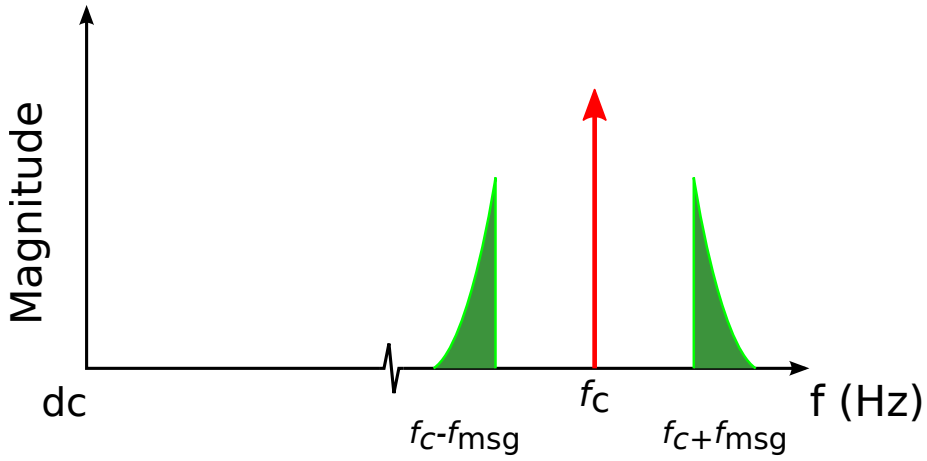

FIGURE 4.5: Modulated signal from tag

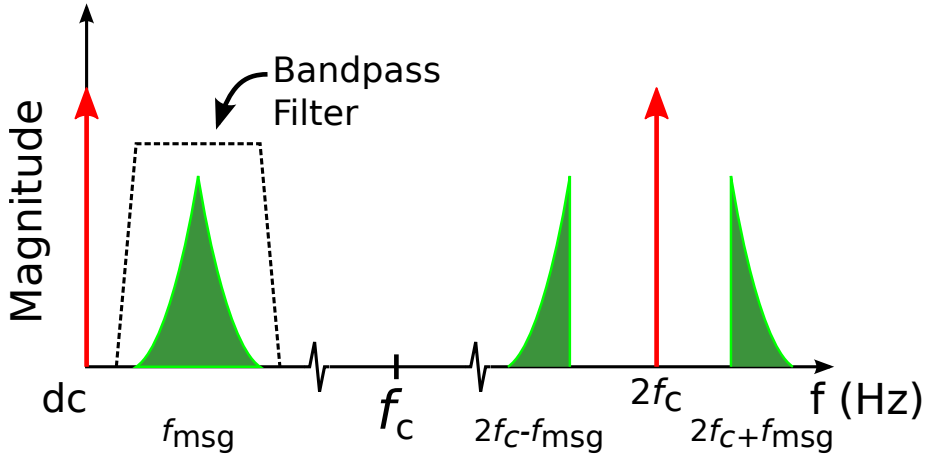

FIGURE 4.6: Signal output from mixing operation

velocity v, the reader voltage signals are

$$V_{\text{out}} = \boldsymbol{K}(r)\,(1+\Gamma^{*})\left(e^{j\omega t\frac{1}{2\pi}\left(\frac{1-\frac{v}{c}}{1+\frac{v}{c}}\right)}\right). \tag{4.15}$$

Mixing with the transmit LO yields

$$V_{\text{out}} = \boldsymbol{K}'(r)\,(1+\Gamma^{*})\left(e^{jt\left(\frac{1}{2\pi}\frac{2v}{c+v}\right)} + e^{jt\left(\omega+\frac{\omega}{2\pi}\left(\frac{1-\frac{v}{c}}{1+\frac{v}{c}}\right)\right)}\right)... \tag{4.16}$$

After filtering and removing high-frequency components greater than the carrier

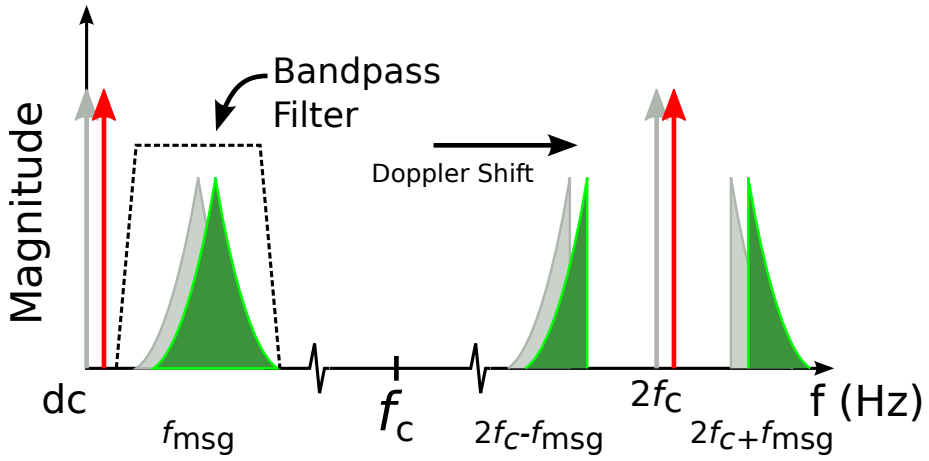

FIGURE 4.7: Signal output from mixing operation with Doppler spread shown

frequency, the result is

$$V_{\text{bb}} = \boldsymbol{K}'(r)\,(1+\Gamma^*)\left(e^{jt\left(\frac{1}{2\pi}\frac{2v}{c+v}\right)}\right). \tag{4.17}$$

where

$$\omega_{\text{dp}} = \left(\frac{1}{2\pi}\frac{2v}{c+v}\right) \tag{4.18}$$

is the Doppler shift frequency in units of radians per second for an object moving radially away from a reader at velocity v meters per second. The velocity is doubled as the Doppler penalty is incurred in the forward trip (reader-to-tag) and the return trip (tag-to-reader).

Under the assumption of a stationary reader and tag, no Doppler effect is present and the baseband output signals consist of a DC constant and the message signal applied to the tag reflection coefficient. This assumes that signals with frequency components above the carrier frequency have been removed. When motion is involved and a tag is moving with relative velocity v away from the reader, the baseband output consists of a constant located at the Doppler frequency and the message signal shifted in frequency each with a distance dependent, and therefore time-varying, complex vector $\boldsymbol{K}'(r)$ applied. The Doppler shift of the message signal is either

towards or away from DC depending on tag motion either being away from or towards the reader, respectively.

In general, object velocity remains well below the data rate of the of the message signal ($v << f_{\text{Data Rate}} << c$). For a typical UHF RFID system operating with a carrier frequency of 915 MHz, a tag velocity of 1 m/s results in a Doppler shift of only $\simeq$ 6 Hz. Data rates for a common UHF RFID tag employing the EPC Class-1 Generation-2 protocol are between 40–640 kHz with symbol rates up to 20 MHz recently reported [16]. Doppler spread for such velocities does not pose a problem and is easily removed by bandpass filters as Figures 4.4 – 4.7 illustrate.

4.3 The general backscatter channel model

There are many examples and detailed investigations of the UHF backscatter channel available in the literature [68–74]. In general terms, the backscatter channel is a set of complex gains applied to the system and easily extendable to multiple-in and multiple-out (MIMO) backscatter systems as well. The backscatter channel model presented in this section is based on the backscatter gain matrix used by Arnitz [75].

The backscatter channel is modeled as the concatenation of the forward channel gain, the differential backscatter reflection coefficient and the return channel [75]. A backscatter system with L transmit antennas, N receive antennas, n backscattering devices evaluated over k frequency components is defined. A wave at frequency f_k sent from transmitting antenna TX_l to the backscattering tag (BT) BT_m is attenuated by the complex forward channel gain $c_{lm,k}$. In simulation, the complex channel gains are modelled using a random variable with distribution determined by the fading model. For modeling an indoor backscatter channel, generally a complex Rcian distribution is assumed [69–74, 76]. The tag BT_m modulates the incident carrier using a time-varying reflection coefficient and we define $\Delta\Gamma^*$ as a differential reflection coefficient between two loads. The modulated signal then returns to

a receiving antenna and is attenuated by channel gain $c_{mm,k}$. Combining these, a complex backscatter gain matrix is formed

$$\boldsymbol{B_{m,k}} = \begin{bmatrix} c_{1m,k}\Delta\Gamma^*_{m,k}c_{m1,k} & \dots & c_{Lm,k}\Delta\Gamma^*_{m,k}c_{m1,k} \\ \vdots & \ddots & \vdots \\ c_{1m,k}\Delta\Gamma^*_{m,k}c_{mN,k} & \dots & c_{Lm,k}\Delta\Gamma^*_{m,k}c_{mN,k} \end{bmatrix}. \tag{4.19}$$

Note that the channel gains are a complex vector that represent the channel gain for a particular frequency of interest. The value takes into account the multipath channels, antenna gains/directivities, cable losses and transmit/receiver band limitations. Since all gains have been accounted for, it then follows that $\Gamma^*_{m,k}$ is a constant for the gain matrix and may be moved outside. The result then is the differential reflection coefficient gain applied to the outer product of the forward channel gain and the return channel gain, or

$$\boldsymbol{B_{m,k}} = \Delta\Gamma^*_{m,k} \begin{bmatrix} c_{m1,k} \\ \vdots \\ c_{m,N,k} \end{bmatrix} \times \begin{bmatrix} c_{1m,k} & \dots & c_{Lm,k} \end{bmatrix} \tag{4.20}$$

where separation of the forward channel frequency response from the return channel frequency response is clear.

The forward and return channel gains for a particular tag, $\mathrm{BT_m}$, form the forward and return channel frequency response over the bandwidth represented by the k carriers. In taking the inverse Fourier transform of the forward and return channel gains, the time-domain impulse response is obtained. This is applied to the time-varying reflection coefficient presented to the tag antenna, $\Gamma^*(t)$, using a time-domain filter. In this way, tag performance is evaluated in a real-world measured channel to characterize performance in the presence of multipath, ISI and noise.

Later in this work, an indoor backscatter channel will be measured by forming the forward and return complex channel gain matrices for varying backscatter tag locations in an indoor environment. Measured QAM backscatter impedances will

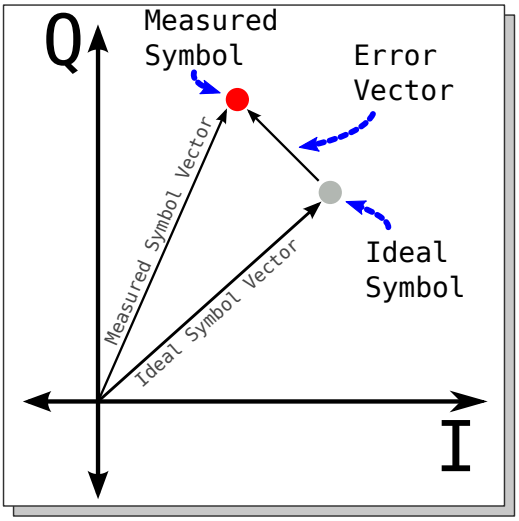

FIGURE 4.8: Vector description of error vector magnitude

then be applied, through pulse-shaping, to form the time-domain $\Gamma^*(t)$. In this way, real-world performance of QAM backscatter will be evaluated through use of the backscatter channel impulse response.

4.4 Signal quality evaluation

A common signal quality metric of a digital communication system is the bit error rate (BER). BER represents the ratio of number of bit errors to total bits transmitted. This can be seen in most communications textbook where graphs plotting BER for varying signal-to-noise ratio conditions are shown. The BER curves will vary for differing modulation schemes. While most textbooks treat the channel as only an additive white gaussian noise (AWGN) model, BER curves for other channels (i.e. Rayleigh, Rician, etc.) may also be computed.

The BER metric takes what is essentially a binary view of a communications system. A bit either is successfully received or is not. It is not useful in describing *how incorrect* a symbol is. For this reason, it is useful to use the error vector magnitude (EVM) metric to measure device performance in noisy conditions. EVM represents

the mean of the error vector magnitude normalized by the average ideal symbol power. It is is defined as

$$\text{EVM} = \sqrt{\frac{\frac{1}{N}\sum_{i=1}^{N}\left(I_i - \hat{I}_i\right)^2 + \left(I_i - \hat{I}_i\right)^2}{\frac{1}{N}\sum_{i=1}^{N}\left(\hat{I}_i^{\,2} + \hat{Q}_i^{\,2}\right)}} \tag{4.21}$$

where I_i and Q_i represent the in-phase (i.e. real) and quadrature (i.e. imaginary) components of the received, demodulated symbol, $\hat{I}_i$ and $\hat{Q}_i$ are the ideal in-phase and quadrature symbol locations, and N is the total number of symbols [77, 78].

4.5 Chapter conclusion

In this chapter, a reader-tag communication system has been defined and described. This has been used to analyze the basics of bacskcatter communication. A vector baseband signal model including the structural scattering term, environmental reflections, self-jammer, and data-carrying modulated term has been presented. This model will be experimentally verified in the next chapter.

The effect of Doppler spread in backscatter communications has also been examined. For a tag moving radially outward from a reader operating at a carrier of 915 MHz, a Doppler shift of 6 Hz will be preset for a tag moving at 1 m/s. Such a small shift is negligible compared to typical backscatter data rates.

5

Demonstration of wideband QAM backscatter

This chapter provides experimental validation of wideband vector backscatter using a discrete component device. Using this device, a 4-QAM/4-PSK backscatter modulator and 16-QAM backscatter modulator is demonstrated. Using the 16 state modulator, the highest reported backscatter link rate to date of 96 Mbps (raw link rate) is shown. Experimental results are taken in an indoor channel with minimal clutter.

This chapter is based on collaborative work by the author [15–17]. The author's contributions to the publications presented include design, construction, modeling, and performance evaluation of the circuits as well as receiver design, transmitter design, firmware and software and the associated hardware elements.

Contributions in this Chapter:

- Experimental validation of QAM backscatter using two modulators
    1. Discrete component 4-QAM/4-PSK modulator
    2. Discrete component 16-QAM modulator

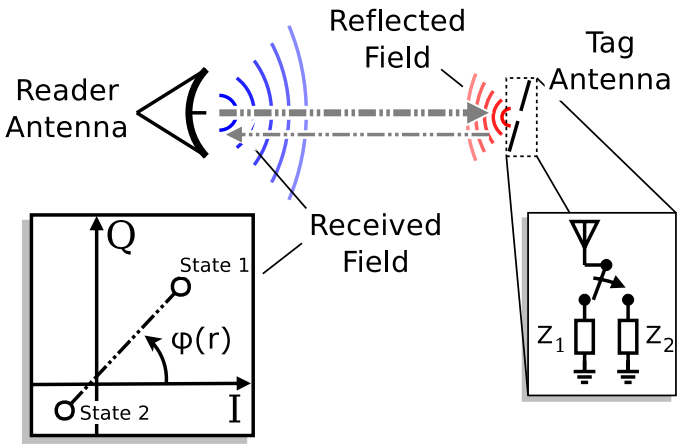

FIGURE 5.1: Typical UHF RFID system with binary load modulation yielding ASK or PSK binary demodulated signal [©2012 IEEE]

- Experimental demonstration of the highest reported to date backscatter data rate (96 Mbps, 15.5 pJ/bit)

5.1 Introduction to the discrete component QAM device

UHF RFID systems employing modulated backscatter communication links, such as those based on the widely deployed ISO18000-6c or EPC Global Class 1 Generation 2 specification[14], have traditionally been analyzed using techniques first developed to analyze radar systems. This chapter[1] demonstrates that scalar valued differential RCS techniques are unnecessarily limiting for RFID system analysis because of the inherent coherence of the backscatter link and the complex-valued nature of load dependent scattering from an RFID tag's antenna.

In most commonly deployed UHF RFID systems, the UHF backscatter link employs a simple binary modulation scheme, such as ASK or PSK backscatter generated by a two-state modulation of the impedance presented to a tag's antenna (Fig. 5.1). Because tag to reader distance is generally unknown *a priori*, most readers employ

[1] Portions of this chapter are a derivative of previously published work, ©2012 IEEE. Reprinted, with permission, from Thomas et al., "Quadrature amplitude modulated backscatter in passive and semipassive UHF RFID systems," IEEE Transactions on Microwave Theory and Techniques, April 2012.

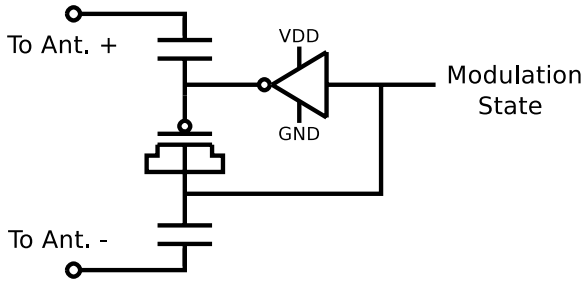

FIGURE 5.2: Example PSK modulation circuit typical of current generation RFID tags. Figure derived from [43, Fig. 3] [©2012 IEEE]

homodyne I/Q demodulation and rotate the received constellation until it falls on the real axis before demodulating as if the signal were ASK regardless of whether the tag's modulator is configured to generate ASK or PSK modulation. In this paper, we exploit multi-state complex-valued load dependent scattering to yield QAM backscatter that is compatible with the homodyne reader architecture.

This chapter, based on the author's previous work [17], demonstrates the use of load dependent scattering to generate QAM backscatter with a simple modulator suitable for single-chip CMOS implementation. The modulator has a static power consumption of only 115 nW. Related work has presented a vector modulator based on a PIN diode phase shifter controlled by bias currents generated by two DACs [79]. The latter circuit has a static power consumption of 80 mW, which is prohibitively high power consumption for either passive or semi-passive tags. In contrast to the present approach, it is not suitable for monolithic implementation because PIN diodes and wideband quadrature hybrids are not available in standard CMOS processes.

The use of QAM in passive and semi-passive UHF RFID opens up many new avenues for UHF RFID, including higher spectral efficiency than is possible with ASK or PSK and improved data throughput with reduced on-chip symbol clock rate.

In the simplest implementation, an M-ary QAM modulation scheme can be im-

plemented with M distinct load impedances that are switched across the terminals of the tag's antenna, although other implementations are possible, including a simple impedance DAC where weighted arrays of inductors, capacitors, and resistors are used to reduce the number of lumped elements to fewer than M. In a monolithic implementation this translates to a reduction in die area and thus a cost and yield improvement. For many types of antennas it is possible to design such an impedance DAC with only resistors and capacitors, which makes the approach particularly suitable for CMOS integration.

5.2 Demodulation in passive and semi-passive UHF RFID systems

Current passive and semi-passive RFID tag modulators are designed either to modulate the real part of the tag IC's reflection coefficient, yielding ASK backscatter, or the imaginary part, yielding PSK backscatter. The most common circuit implementation of ASK for passive devices switches between a matched state, which maximizes power delivered to the passive tag's power rectifier circuitry, and a load resistance that introduces a deliberate mismatch to produce a backscatter signal. A binary PSK modulation circuit is shown in Fig. 5.2 where the modulating transistor switches a capacitance across the antenna's terminals to introduce a phase shift in the scattered field.

Because typical RFID readers employ homodyne receivers, the backscatter link is coherent to the reader's transmit local oscillator. Due to this coherence, the phase of the backscatter as observed in the demodulated baseband changes with tag to reader distance. As the tag moves radially outward from a reader, the phase of the backscatter field incident on the receiver rotates at a rate of 2π radians per half-wavelength of distance. At the 860-950 MHz frequencies typically used for UHF RFID, this leads to a rotation of 2π every ≈ 16 cm. Since the reader to tag distance r is usually initially unknown and both ASK and PSK modulation schemes are permitted by most RFID

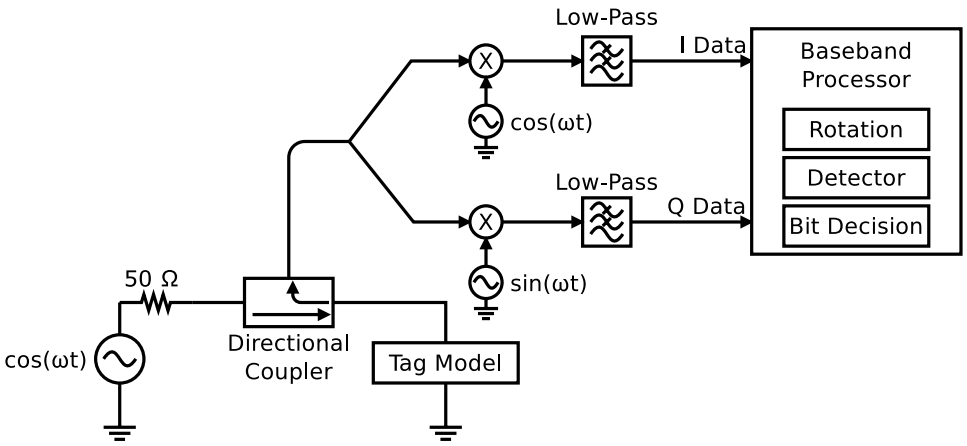

FIGURE 5.3: Cabled test setup (simplified reader) implemented physically as well as in ADS simulation [©2012 IEEE]

standards [14], the reader must be able to demodulate tag signals arriving at any phase. For binary modulation schemes such as ASK or PSK, the reader's baseband signal processing software typically rotates the received signal vector from its arrival angle in the I/Q plane back to the in-phase axis prior to data slicing to demodulate the tag's binary data. Most existing RFID reader hardware is therefore not restricted to binary ASK/PSK backscatter modulation. While upgraded reader baseband signal processing software would be required to demodulate M-ary QAM data with some increase in computational complexity, QAM demodulation is supported by the existing RFID reader architecture.

5.3 QAM tag modulator design and simulation

Based on the observation from (3.38) that a careful choice of modulating load impedance Z_L can yield a scattered E-field component in any quadrant of the complex plane, a series of modeling exercises were conducted to simulate a practical backscatter QAM modulator. Component choices were validated using Agilent Advanced Design System (ADS) with the simplified reader system model shown in Fig. 5.3.

Modulating impedance values can be chosen by first writing each symbol of the

desired I/Q constellation in the form

$$\mathcal{S}_i = x_i + jy_i \tag{5.1}$$

where x_i represents the in-phase component and y_i represents the quadrature component of the i-th symbol. In order to produce impedance values realizable with passive components, all reflection coefficients are confined within a circle about the conjugate match with magnitude $\leqslant 1$. These reflection coefficients are then scaled by a constant $0 < \alpha \leqslant 1$.

$$\Gamma_i^* = \alpha \cdot \frac{\mathcal{S}_i}{\max|\mathcal{S}|} \tag{5.2}$$

Values of α closer to 1 reflect increasing amounts of the incident RF power back to the reader and thus result in higher backscatter signal strength. This is the typical case for a semi-passive (battery-assisted) tag, such as the one described in this work, because maximizing the backscatter signal strength gives the longest read range. Passive tags, however, must harvest their DC operating power from the incident field. Values of $\alpha \ll 1$ are typical for a passive tag to permit a majority of the incident field to be absorbed in the energy harvesting circuit. Because α is a constant that relates power reflection and power transmission coefficients [64,67], the optimal value will depend on the desired balance between backscattered signal power and power delivered to the energy harvesting circuit. For binary ASK and PSK, this tradeoff has previously been analyzed as a function of reflection coefficient [80]. Due to government regulations limiting the reader's transmitted power, well-designed passive RFID systems usually operate in a forward-link limited regime where the read distance is limited by the ability to deliver power to the tag.

By rearranging the conjugate reflection coefficient Γ^* from (3.35), we find a set

of complex impedance values for a given I/Q constellation

$$Z_{L_i}\Big|_{Z_a^*} = \frac{Z_a^* - Z_a\Gamma_i^*}{1+\Gamma_i^*} \tag{5.3}$$

normalized to Z_a^*, the conjugate of the antenna impedance. The resulting modulating impedances will then fall in all 4 quadrants of a modified Smith chart normalized to $Z_0 = Z_a^*$.

Because UHF RFID antennas are typically designed to include significant amounts of inductance in order to nearly conjugate match a capacitive tag IC impedance, all QAM modulating impedance values may be realizable using only R and C components. For example, an antenna designed to match the Impinj Monza4 IC [81] has an impedance $Z_a = 11 + j143$. The required impedance states for a 4-QAM/4-PSK modulator matched to this antenna with $\alpha = 1$ are all capacitive [$-j147.6$, $-j169.6$, $-j116.4$, $-j138.4$] with $C \approx$ [1.18 pF, 1.03 pF, 1.49 pF, 1.26 pF] respectively.

However, for a resonant antenna with approximately real-valued Z_a, modulating impedances found by solving (5.3) will require R, L, and C components. This creates a problem for monolithic implementation because standard CMOS processes yield good quality resistors and capacitors but physically large and low Q inductors. In order to make CMOS integration feasible by eliminating L components, a transformation from RLC impedances to RC-only may be found by enforcing the constraint that

$$\Gamma^*_{i_{\text{C Only}}} = \beta\left(\Gamma_i^* - j\min\left[\Im\left(\Gamma^*\right)\right]\right) \tag{5.4}$$

for all Γ_i^* before re-applying the conversion to impedance values (5.3), where $\Im\left(\Gamma^*\right)$ represents the imaginary portion of the reflection coefficients and

$$\beta = \frac{\max\left[\Im\left(Z_L\right)\right]}{\max\left[\Im\left(Z_L\right)\right] - \min\left[\Im\left(Z_L\right)\right]} \tag{5.5}$$

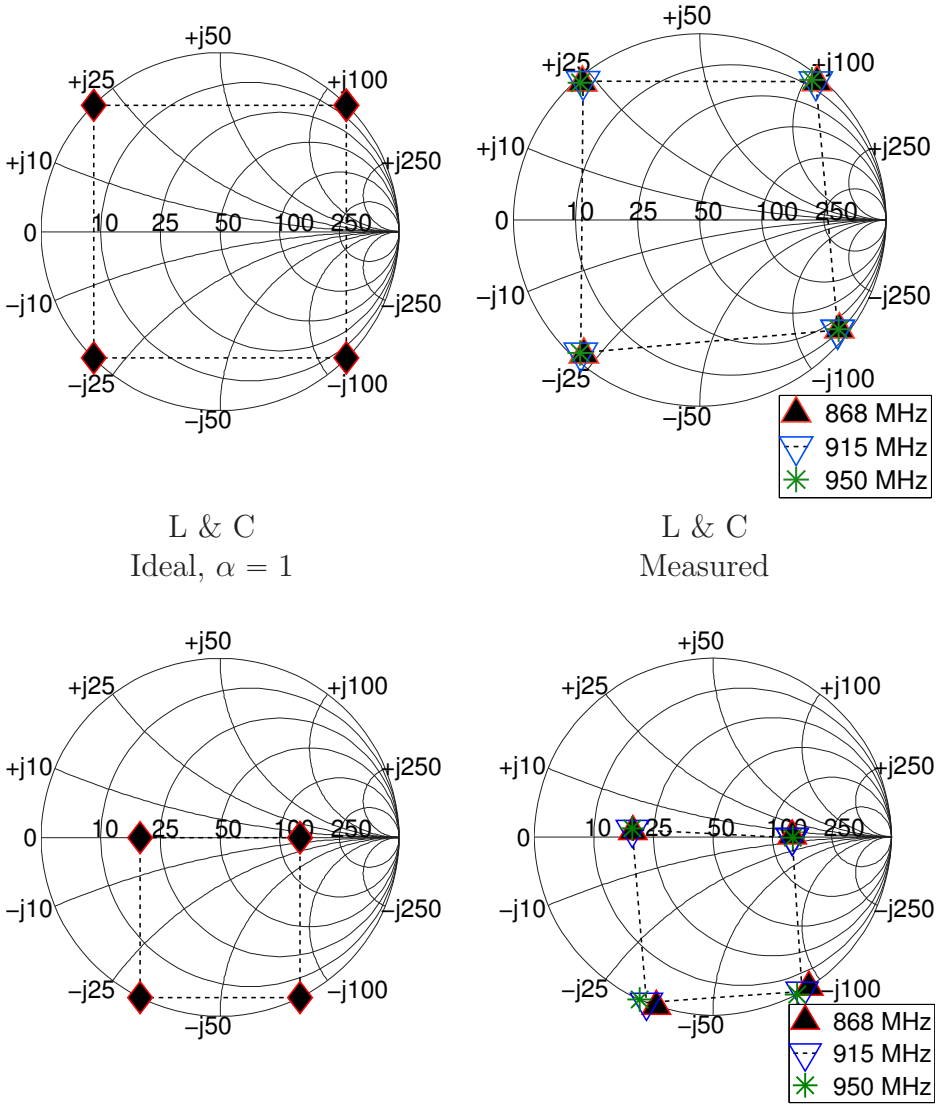

L & C
Ideal, $\alpha = 1$

L & C
Measured

C-Only
Ideal

C-Only
Measured

FIGURE 5.4: Smith charts showing ideal and measured modulating impedances for a $M = 4$ PSK/QAM modulation scheme [©2012 IEEE]

scales the reflection coefficients by the portion of impedances above the real line. This transformation compresses the I/Q vector space of the constellation, resulting in a tradeoff of reduced backscatter amplitude compared to the RLC implementation but yielding the desired QAM constellation with a CMOS process. Smith charts showing the conjugate reflection coefficients of the RLC and RC-only constellations

Table 5.1: Impedance values for 4-PSK / 4-QAM Modulator with L&C components with $Z_a = 50\Omega, \alpha = 1$

Ideal Impedance States: $Z\|_{Z_a} = 50\ \Omega$				Γ Error versus Frequency *(Referenced to 915 MHz)*	
Z	R + jX Ω	L/C Value	Γ	860 MHz	950 MHz
Z_1	$0.0 - 20.71j$	8.4 pF	0.71 +0.71j	3.66%	2.69%
Z_2	$0.0 - 120.71j$	1.44 pF	-0.71 +0.71j	3.8%	2.62%
Z_3	$0.0 + 120.71j$	21.0 nH	-0.71 -0.71j	3.8%	2.62%
Z_4	$0.0 + 20.71j$	3.6 nH	0.71 -0.71j	3.66%	2.69%

Table 5.2: Impedance values for 4-PSK / 4-QAM Modulator with R&C only, with $Z_a = 50\Omega, \alpha = 1$ [©2012 IEEE]

Ideal Impedance States: $Z\|_{Z_a} = 50\ \Omega$				Γ Error versus Frequency *(Referenced to 915 MHz)*	
Z	R + jX Ω	C Value	Γ	868 MHz	950 MHz
Z_1	$0.0 - 30.9j$	5.63 pF	0.45 +0.89j	4.66%	3.39%
Z_2	$0.0 - 80.9j$	2.15 pF	-0.45 +0.89j	4.77%	3.33%
Z_3	$130.9 + 0.0j$	-	-0.45 +0.0j	0.0%	0.0%
Z_4	$19.1 + 0.0j$	-	0.45 +0.0j	0.0%	0.0%

are shown in Fig. 5.4 for a $Z_a = 50 + j0\,\Omega$ antenna where the compression of vector space spanned by adjacent symbols is apparent.

5.3.1 Experimental validation

Based on the block diagram in Fig. 5.5, a discrete component semi-passive tag pictured in Fig. 5.6 was constructed to test a 4-state PSK / 4-QAM backscatter modulator designed with this procedure. Four lumped impedances are connected to an antenna port through an Analog Devices ADG904 SP4T CMOS FET switch that is controlled by a TI MSP430F2011 microcontroller. The microcontroller was programmed to stream 128 bit strings of pseudo-random data to modulate the 4 switch states at 200k symbols/s, corresponding to a data rate of 400kbps. The static DC power consumption of the modulator, excluding the power consumption of the micro-

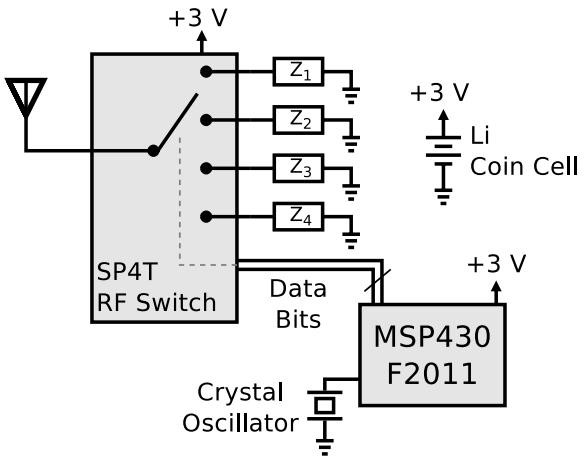

FIGURE 5.5: Block diagram of the 4-PSK / 4-QAM semi-passive tag. In this modulator implementation, the number of discrete impedance states is equal to the number of symbols [©2012 IEEE]

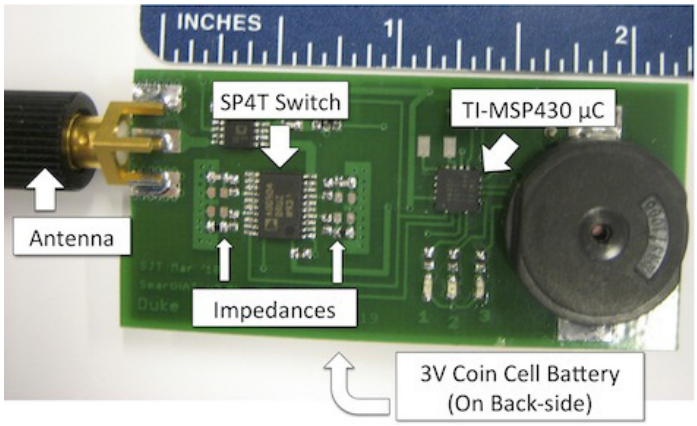

FIGURE 5.6: Photo of tag used for experimental data. A SP4T switch allows for 4-state modulation schemes controlled by two pins of a microcontroller [©2012 IEEE]

controller, is 3.0 V at 38.3 nA, or 115 nW. The dynamic power consumption is shown in Fig. 5.7. In the prototype tag, a MSP430F2011 microcontroller consumes an additional 1-2mA (or 3-6mW) when generating the pseudo-random data. A CR2032 3V lithium coin cell battery serves as a power source for the device.

The values of the lumped impedances were designed using (5.4) to match an antenna with $Z_a = 50 + j0\,\Omega$ and $\alpha = 1$. The calculated values for the L&C and C-Only cases are shown in Tables 5.1 and 5.2. At a design center frequency of 915 MHz,

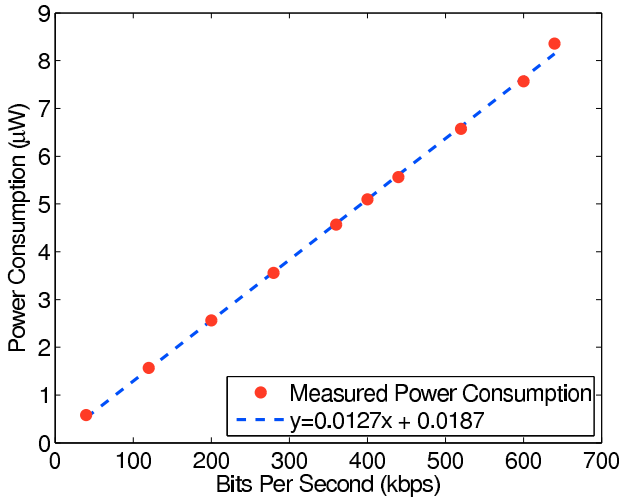

FIGURE 5.7: Measured DC power consumption of the 4-QAM/4-PSK modulator for varying data data rates [©2012 IEEE]

the nearest standard lumped values were 8.0 pF, 2.2 pF, 22 nH, and 3.9 nH for the L&C case and 5.6 pF, 2.2 pF, 130 Ω and 19.1 Ω for the C-Only case. The capacitors have a tolerance of ±0.1 pF and the inductors have a tolerance of ± 0.1nH. As the carrier frequency deviates from the design center frequency, constellation distortion is introduced causing a greater EVM, reflecting increasing BER.

Because the prototype semi-passive tag is matched to 50 Ω, a cabled test bench setup similar to that shown in Fig. 5.3 can be used to characterize the tag. An Agilent MXG N5181A synthesized RF source set to produce +3 dBm at 915 MHz was used as the forward link source. The reflected signal was separated using an MiniCircuits ZFDC-15-10 15 dB directional coupler and fed to a Linear Technology LT5575 I/Q demodulator. The baseband I and Q signals were sampled at 8 bit resolution with a sampling rate of 2 MSPS using an Agilent Infinium DSO8104 oscilloscope. Fig. 5.8(a) shows the received constellation generated by the L&C modulator while Fig. 5.8(b) shows the received constellation generated by the C-Only modulator as captured by the oscilloscope with random I and Q data.

Digitally generated AWGN was summed with the captured time-domain signal

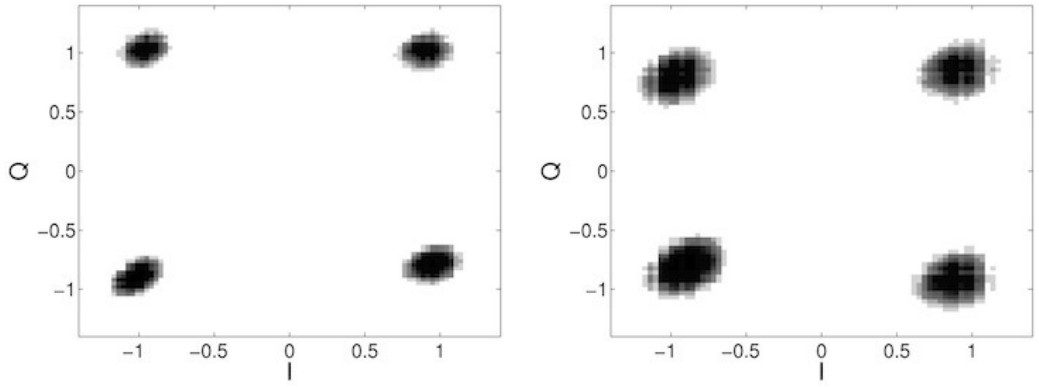

(a) 4-QAM/4-PSK (L & C) (b) 4-QAM/4-PSK (C-Only)

FIGURE 5.8: Measured I/Q baseband constellations (density plot) generated by the semi-passive tag in the cabled test setup [©2012 IEEE]

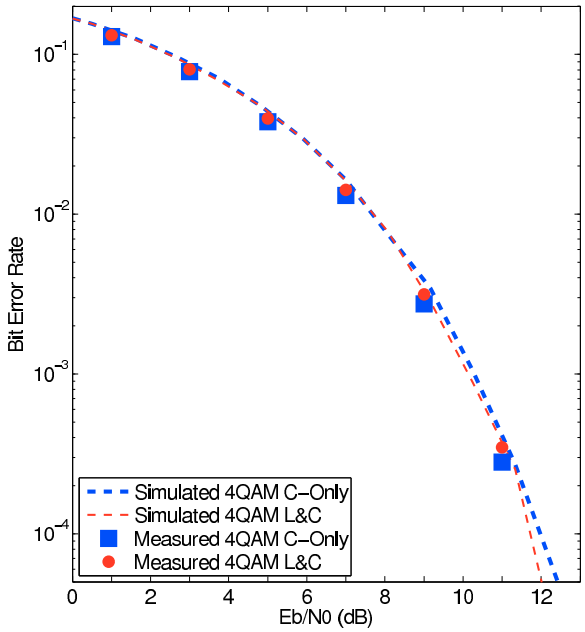

FIGURE 5.9: Simulation vs. cabled setup measurement of bit error rate for 4-QAM/4-PSK modulation [©2012 IEEE]

samples. A minimum distance soft decision demodulator was used to obtain BER curves for the two constellations (L&C, and C-Only) found in Tables 5.1 and 5.2 and the Smith charts of Fig. 5.4. The resulting measured BER curves, shown in Fig. 5.9, showed good agreement with those predicted by MATLAB simulation.

The final step was to connect the switched impedances to a 50 Ω dipole antenna and perform an over-the-air test of the resulting semi-passive backscatter modulator. The transmitter employed for this test consisted of an Agilent MXG N5181A synthesized signal source followed by a Mini-Circuits ZHL-5W-2G amplifier yielding a conducted output power of +30 dBm. The effective isotropic radiated power (EIRP) of this transmitter setup was +38.4 dBm given a Yagi antenna of 9dBi gain and a cable loss of 0.6 dB. A 6 dBi patch receiving antenna was located with close proximity to the transmitting antenna to minimize the radar bistatic angle. The test setup used for gathering the over-the-air data is shown in Fig. 5.10.

As the tag moved radially outward with respect to the reader, the baseband constellation was observed to rotate and scale as expected given the signal model presented in Fig. 4.2. Due to the indoor environment and the interaction with multipath signals, some locations in the lab exhibited a deep fade in the detected backscatter signal. This behavior is typical for any passive or semi-passive backscatter system and is not specific to the QAM modulation method presented in this work.

During initial testing in a typical indoor lab environment, 500,000 bits were transmitted from multiple locations. No more than 1 bit error was observed at any location within 4.5 m. This implies a BER of less than $\approx 10^{-5}$ over the air in a low-interference, relatively controlled laboratory setting. Given the experimental setup, measurement times and thus the number of bits accumulated for error rate measurements are limited by oscilloscope capture memory depth. The tag was then fixed at a separation of 2.92 m from the transmit antenna and the RF power feeding the antenna was swept to produce the data shown in Fig. 5.11. Simulation as well as over-the-air results show the C-Only 4-QAM / 4-PSK constellation performance trailed the L&C performance by a margin of approximately +1.5 dB Eb/N0 to achieve equivalent BER. This is a tradeoff due to the reduction in inter-symbol

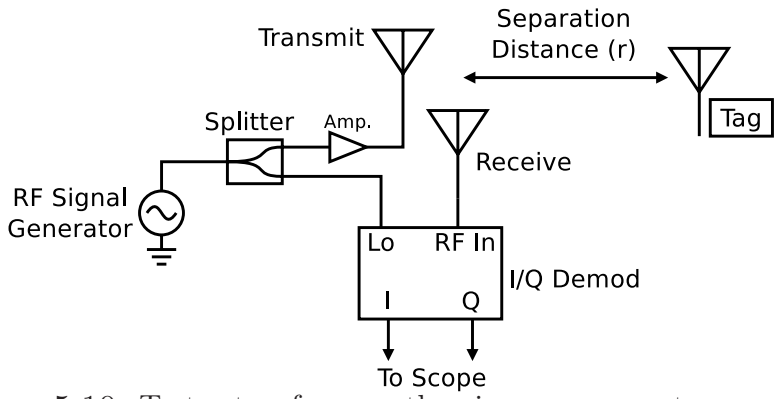

FIGURE 5.10: Test setup for over-the-air measurements [©2012 IEEE]

distance brought about by the compression of the C-Only constellation by the factor β.

5.4 Discussion

The development of passive and semi-passive RFID system models has in most cases followed directly from radar systems techniques. While scalar valued differential radar cross section (DRCS) analysis is useful for analyzing binary ASK or PSK modulation schemes, the DRCS approach is unnecessarily limiting. Because the E field scattered from a tag antenna is complex-valued, passive and semi-passive RFID systems can be designed to produce M-ary QAM signals with minimal increase in cost or complexity at the tag or the reader.

More versatile M-ary modulation schemes also permit an important new design space for RFID systems. Because a tag's on-chip oscillator frequency ultimately limits the symbol rate, not the bit rate, higher values of M yield increased data rate for a given on-chip oscillator frequency. This in turn allows for fine grained tradeoffs between on-chip power consumption, data rate, and link margin.

In terms of bandwidth (spectral) efficiency and performance in the presence of AWGN, 4-QAM/4-PSK and binary PAM have equivalent performance [65, ch. 7]. For a given data rate, the lower symbol rate of 4-QAM/4-PSK permits the QAM

modulator transistors to switch at half the frequency compared to a binary modulator. In general, an M-ary QAM modulator can be clocked slower by a factor of $\log_2 M$. In the digital sections of a tag IC, careful choice of internal memory bus width and associated data path width may also allow the clock rate driving these on-chip circuits to be correspondingly reduced. The power dissipation in all of these sections will thus decrease in accordance with the $\frac{1}{2}CV^2f$ model for CMOS power dissipation. Higher order constellations can improve modulator power efficiency further.

As an example, a 16-QAM constellation is shown in Fig. 5.12 for implementation either with or without inductors. When designed for a $50\,\Omega$ antenna operating at 915 MHz, the $\alpha = 1$ C-Only implementation requires a minimum capacitance of 1.93 pF, a maximum capacitance of 12.74 pF, and a maximum resistance of $130.9\,\Omega$. Future work will explore the tradeoffs in the choice of α and β with such higher-order constellations.

The multi-state RF switch based modulator presented in this chapter is simple and power efficient, though it trades off die area for simplicity because M switched impedances are required to implement M-ary modulation. Future modulator designs can be realized with weighted combinations of R, L, and C components to form simple impedance DACs that hold the promise of similar power consumption with reduced die area.

Finally, as the behavior of backscatter links in multipath environments becomes better understood, it is expected that independent control of the backscatter amplitude and phase will allow for modulation schemes to be designed with multipath immunity as a primary goal.

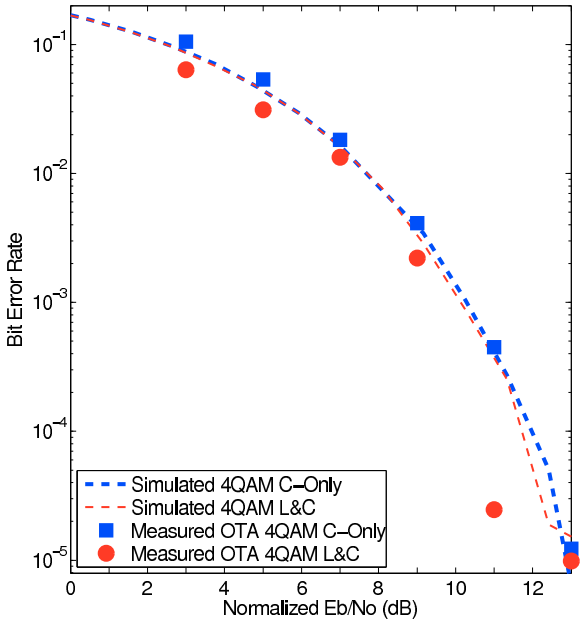

FIGURE 5.11: Measured and simulated over-the-air BER versus Eb/N0 in an indoor environment for 4-QAM/4-PSK implemented with both inductors and capacitors (L&C) as well as capacitors only (C-Only) [©2012 IEEE]

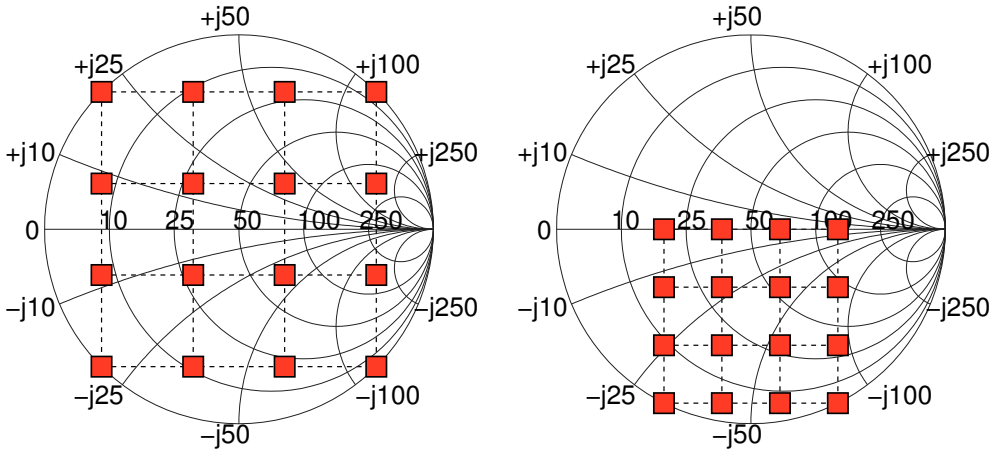

16-QAM L & C 16-QAM C-Only

FIGURE 5.12: Ideal impedances for a $M = 16$ QAM modulator with $Z_a = 50\Omega$ and $\alpha = 1$, with and without inductors [©2012 IEEE]

5.5 Motivation for the 16-QAM backscatter device

As has been shown, UHF RFID tags achieve low-power wireless communication by repartitioning the complexity and power of the radio link. Instead of generating and

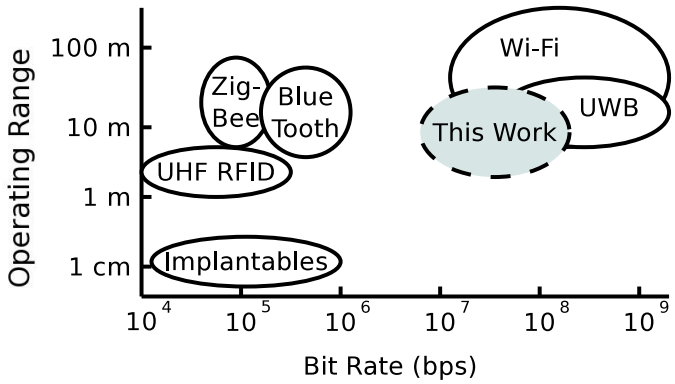

FIGURE 5.13: Comparison of wireless technology bit rates and communication range [©2012 IEEE]

modulating a UHF carrier, UHF RFID tags reduce circuit complexity and power consumption by backscattering a carrier generated by a remote reader. The scattered field is demodulated to reproduce the baseband waveform. In a backscatter system, no transistors are biased for UHF operation. Instead, power is conserved by only switching tag transistors at baseband data rates. For simple ID-only tags employing binary ASK/PSK communication, tag operating power can be less than 2.25 μW [43].

As shown in Fig. 5.13, passive UHF RFID tags based on global UHF RFID standards [14] typically have sub 10 m operating range with data rates up to 640 kbps. While UHF RFID operating range can be increased using semi-passive (battery-assisted) technology, data rates remain low when compared to IEEE 802.11 (WiFi) or UWB [29]. The high data rate and long operating range of these technologies come at an increase in power consumption with reported values as high as $\approx$ 1 W for some WiFi implementations [82]. This is prohibitively high for low-power, remote or embedded sensor applications seeking high-bandwidth wireless communication. In contrast, the backscatter modulator described in this paper is capable of similar uplink data rates with measured power consumption over 50 times less than a typical WiFi chipset.

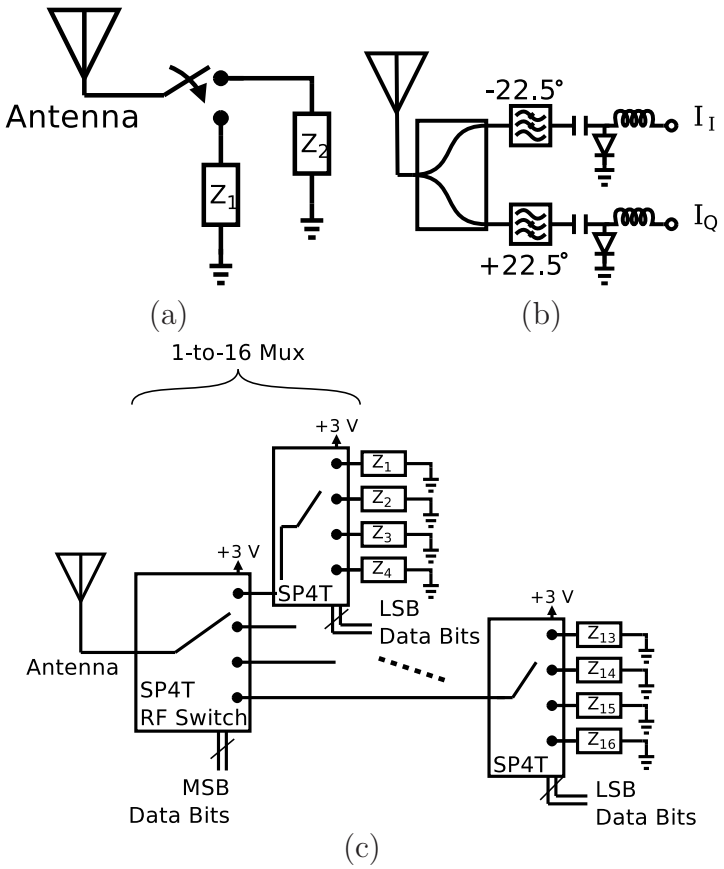

FIGURE 5.14: Block diagram of (a) traditional binary backscatter modulator, (b) PIN diode based vector modulator [79], and (c) high bit rate 16-QAM backscatter modulator presented in this work [©2012 IEEE]

In a typical passive tag employing binary backscatter modulation, the circuit input impedance is switched between a matched, absorptive state designed to maximize RF-to-DC power conversion efficiency and a deliberate impedance mismatch causing an amplitude or phase change in the scattered electric field. Existing RFID standards [14] permit the circuit designer to choose between binary amplitude shift keying (BASK) or binary phase shift keying (BPSK). Historically the modulation is measured in terms of the DRCS, a scalar value representing the distance between input impedance states [59]. A typical binary backscatter modulator is shown in Fig. 5.14(a).

As has been shown, QAM backscatter can be produced with careful control of

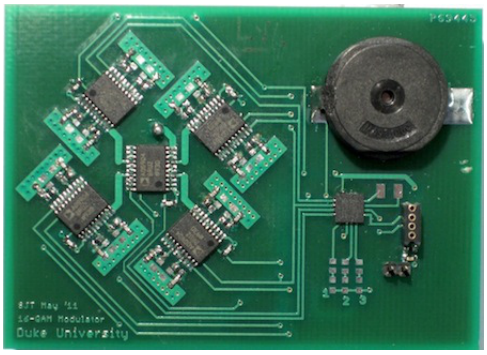

FIGURE 5.15: Photo of the high-bit rate 16-QAM tag. The PCB board measures 6.8 x 4.9 cm [©2012 IEEE]

the tag's input impedance [7, 17, 79]. For example, the circuit shown in Fig. 5.14(b) produces IQ backscatter modulation using bias currents to change the impedance of two PIN diodes connected to a quadrature hybrid [79]. Because this circuit requires a high bias power consumption of 80 mW and two DACs which introduce significant power consumption and data rate limitations, it is not compatible with low-power sensor or wireless applications.

A 16-QAM backscatter modulator, shown schematically in Fig. 5.14(c), is presented[2]. This modulator includes a 16-to-1 mux to modulate the circuit impedance between 16 impedance states. It can be thought of as an "impedance DAC" that converts a 4-bit digital input to a specified modulating impedance. The assembled tag, pictured in Fig. 5.15, is implemented as a semi-passive device using a CR2032 3.0 V coin cell battery for DC power and is capable of transmitting 96 Mbps with the modulator consuming only 1.49 mW (15.5 pJ/bit). Using a +36 dBm EIRP transmitter operating at 915 MHz, the tag has a theoretical maximum operating range of 17.01 m.

[2] This portion of the chapter is a derivative of previously published work, ©2012 IEEE. Reprinted, with permission, from Thomas et al., "A 96 Mbit/sec, 15.5 pJ/bit 16-QAM modulator for UHF backscatter communication," in 2012 IEEE International Conference on RFID, April 2012.

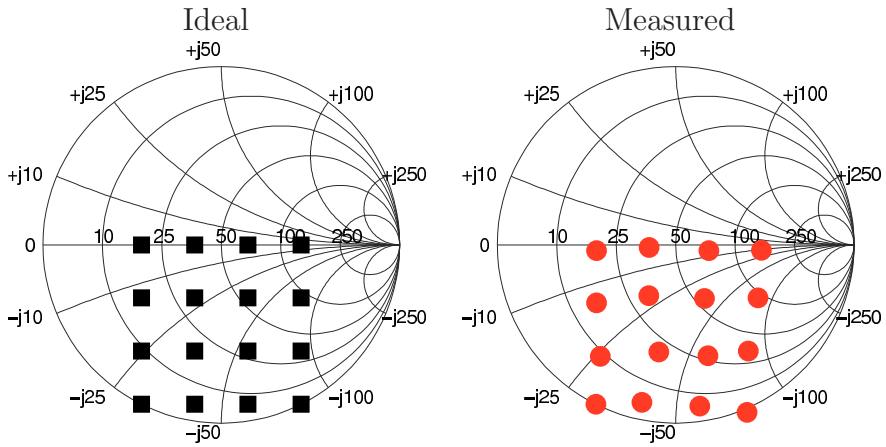

FIGURE 5.16: Comparison between ideal and measured impedance values for a 16-QAM backscatter modulator plotted on a $Z_0 = 50\Omega$ Smith chart [©2012 IEEE]

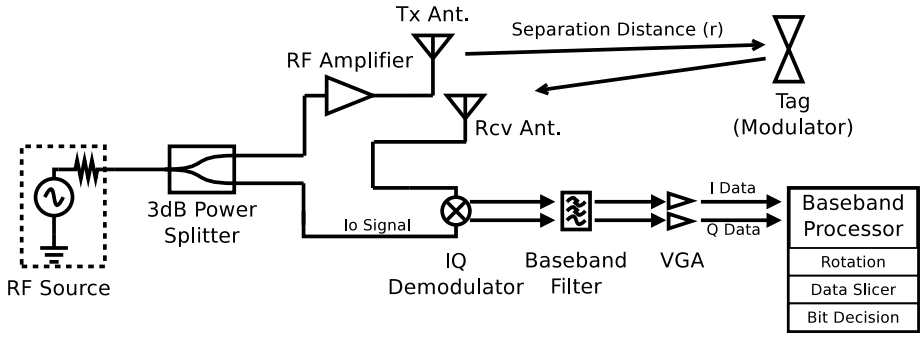

FIGURE 5.17: Bistatic test setup for the high data rate QAM modulator [©2012 IEEE]

5.6 16-QAM tag modulator design

The 16-QAM modulator in this work is designed for a 50 Ω system ($Z_a = 50 + j0\ \Omega$) with $\beta = 0.5$ scaling to eliminate inductors. Conjugate reflection coefficients measured at the design frequency of 915 MHz are compared to simulated values in Table 5.3 and shown on a Smith chart in Fig. 5.16. Using the equation for error vector magnitude (EVM)

$$\text{EVM} = \sqrt{\frac{\frac{1}{N}\sum_{k=1}^{N} |S_{k_{\text{Ideal}}} - S_{k_{\text{Measured}}}|^2}{\max\left[S_{\text{Ideal}}\right]}} \tag{5.6}$$

Table 5.3: Γ^* values for 16-QAM Modulator with RC components, $Z_a = 50\ \Omega$, $\alpha = 1$ [©2012 IEEE]

	Ideal Γ^*	Measured Γ^*	
Z_1	-0.15	-0.19 + j0.03	
Z_2	-0.45	-0.48 + j0.03	
Z_3	-0.15 + j0.3	-0.16 + j0.3	
Z_4	-0.45 + j0.3	-0.46 + j0.29	
Z_5	0.45	0.44 + j0.04	
Z_6	0.15	0.15 + j0.02	
Z_7	0.45 + j0.3	0.44 + j0.33	
Z_8	0.15 + j0.3	0.15 + j0.29	
Z_9	0.45 + j0.6	0.42 + j0.63	
Z_{10}	0.15 + j0.6	0.09 + j0.6	
Z_{11}	0.45 + j0.89	0.44 + j0.9	
Z_{12}	0.15 + j0.89	0.18 + j0.89	
Z_{13}	-0.15 + j0.6	-0.19 + j0.62	
Z_{14}	-0.45 + j0.6	-0.41 + j0.59	
Z_{15}	-0.15 + j0.89	-0.14 + j0.9	
Z_{16}	-0.45 + j0.89	-0.41 + j0.94	
Simulated EVM		868 MHz	2.96%
		915 MHz	0%
		950 MHz	2.09%
Measured EVM		**915 MHz**	**3.62%**

that compares the experimental value of the k^{th} symbol ($S_{k_{\text{Measured}}}$) to the ideal location of the k^{th} symbol ($S_{k_{\text{Ideal}}}$) and normalizes by the maximum ideal symbol magnitude, a symbol EVM of 3.62% was measured at 915 MHz. Simulation results presented in Table 5.3 indicate small variation ($< 3\%$ added EVM) over the 868–950 MHz worldwide UHF band.

5.7 Experimental results

Using the test setup of Fig. 5.17, a series of IQ backscatter constellations are measured. In addition to 16-QAM backscatter, subsets of the 16 impedance states in Fig. 5.16 are selected to yield 4-QAM/4-PSK and 4-Pulse Amplitude Modulation

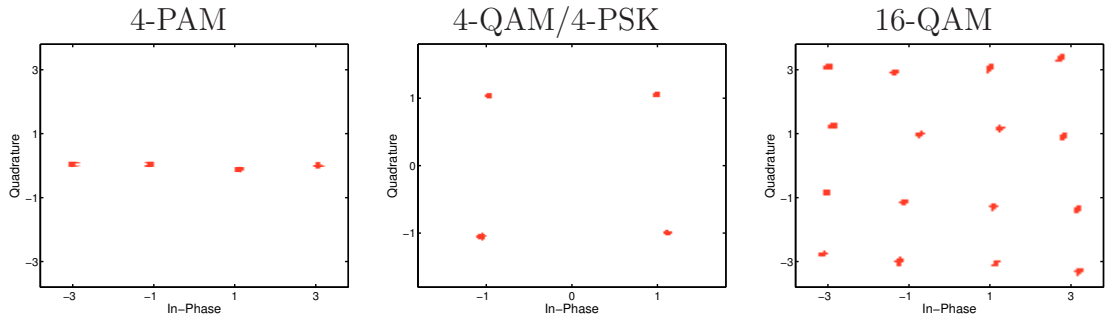

FIGURE 5.18: Measured IQ backscatter constellations operating over a 915 MHz carrier at a separation distance of 2.75 m from a +23 dBm RF source. Data rates for the constellations shown are 1 Mbps (500,000 symbols/sec) for 4-PAM (a) and 4-QAM/4-PSK (b) and 2 Mbps (500,000 symbols/sec) for 16-QAM (c) [©2012 IEEE]

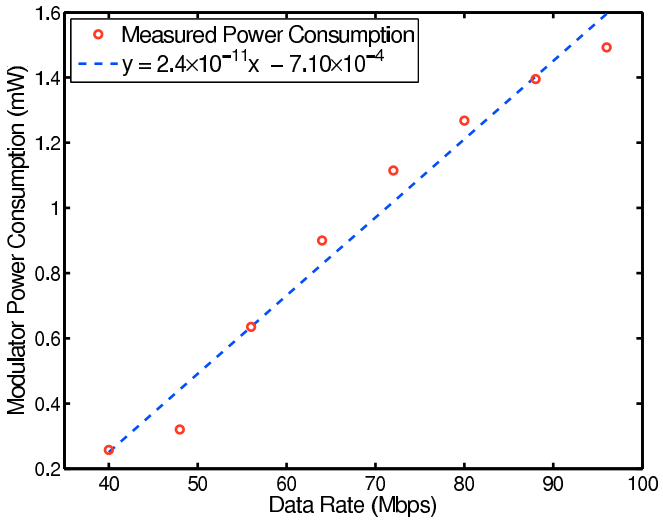

FIGURE 5.19: Measured DC power consumption of the 16-QAM backscatter modulator over a range of data rates [©2012 IEEE]

(PAM). Measurements in Fig. 5.18 are taken over-the-air using a +23 dBm RF source operating at 915 MHz and tag-to-reader separation by 2.75 m. The symbol rate of the modulator was held constant at 500,000 symbols/sec for all three constellations resulting in bit rates of 1 Mbps for 4-PAM and 4-QAM/4-PSK and 2 Mbps for 16-QAM.

The DC power consumption of the modulator was also characterized. This measurement only includes power required for the 1-to-16 Mux modulator implemented

Table 5.4: 16-QAM Backscatter Link Budget [©2012 IEEE]

	λ	P_t	G_t, G_r	$\Delta_{\text{RCS, min.}}$	P_r	$r_{\text{max.}}$
96 Mbps	33 cm	+28 dBm	8 dBi	0.03 m^2	-63.2 dBm	17.01 m
60 Mbps	33 cm	+28 dBm	8 dBi	0.03 m^2	-65.2 dBm	19.20 m
40 Mbps	33 cm	+28 dBm	8 dBi	0.03 m^2	-67.0 dBm	21.25 m

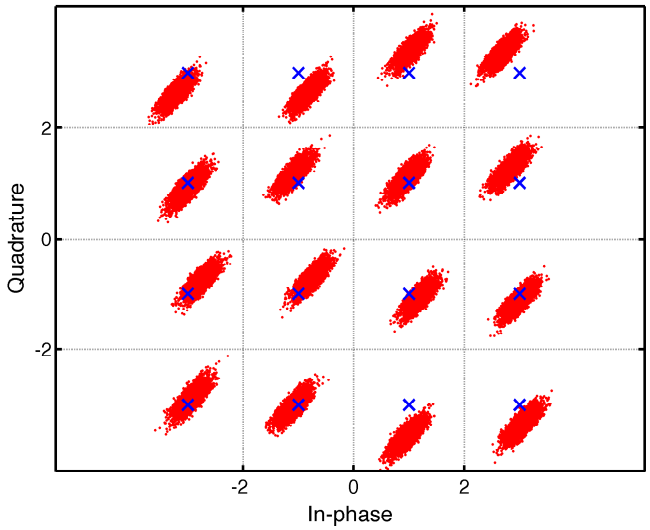

FIGURE 5.20: Measured baseband constellation of a 16-QAM modulator transmitting 96 Mbps at a distance of 1.24 m from a +23 dBm, 915 MHz reader [©2012 IEEE]

using Analog Devices ADG904 CMOS SP4T RF switches and ignores data generation logic feeding the modulator. As the data rate increases, DC consumption increases following $\frac{1}{2}CV^2f$ CMOS switching speed as shown in Fig. 5.19. Continuous operation at 96 Mbps requires 1.49 mW of DC power resulting in an energy per bit of 15.5 pJ.

Due to switching characteristics and state transition time of the SP4T switches, a large settling time ($\approx$ 25 ns) was needed to reduce intersymbol interference and constellation noise. This resulted in a maximum usable symbol frequency of 12 MHz corresponding to a bit rate of 96 Mbps. Maximum bandwidth for the QAM modulator of Fig. 5.14(c) is determined by switching characteristics and state transition time.

A measured 96 Mbps 16-QAM constellation is shown in Fig. 5.20. The red dots showing demodulated data points are compared to the blue marks representing ideal symbol locations. The modulator was measured using a 915 MHz +23 dBm RF source placed 1.24 m away from the tag in a typical indoor environment. This link budget is summarized in Table 5.4. During transmission of 196,736 bits, zero bit errors were observed, for a corresponding bit error rate (BER) of $< 5.08 \times 10^{-6}$ and measured EVM of 9.38%.

Equation (5.7) can be used to estimate range assuming free space propagation, no polarization loss and a semi-passive tag that is not limited by available power. Theoretical maximum operating distances for varying data rates using a standard +36 dBm EIRP transmitter (Table 5.4) are found by assuming spectral efficiency of 1 bps/Hz, a measured reader noise figure of 19 dB and a 12 dB E_b/N_o margin. For operation at 96 Mbps, a theoretical maximum distance of 17.01 m is found using the minimum differential RCS of the constellation [59].

$$r_{\text{max.}} = \left(\frac{P_t G_t G_r \Delta_{\text{RCS}} \lambda^2}{P_r \left(4\pi\right)^3} \right)^{1/4} \tag{5.7}$$

Using the same test setup and conditions as the over-the-air test for Fig. 5.20, EVM for varying data rates is measured. As the data rate increases, the measured EVM in Fig. 5.21 also increases. This result is largely attributed to the switch transition time of the SP4T CMOS switches dominating the bit period as the symbol frequency increases.

5.8 Discussion

In this chapter, a 96 Mbps 16-QAM UHF backscatter modulator was presented, consuming only 15.5 pJ/bit or 1.49 mW of power. The modulator was implemented as a semi-passive tag capable of producing 4-QAM/4-PSK, 4-PAM, and 16-QAM

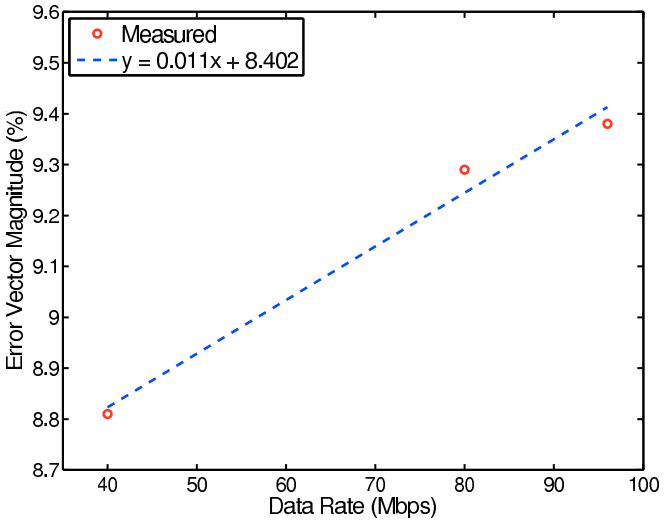

FIGURE 5.21: Measured EVM of a 16-QAM tag placed 1.24 m away from a +23 dBm, 915 MHz reader with a varying data rate [©2012 IEEE]

backscatter. Using a 915 MHz transmitter with +36 dBm EIRP, this backscatter data link has a theoretical maximum operating distance of 17.01 m at 96 Mbps or 21.25 m at 40 Mbps. This device is suitable for ultra low-power wireless applications requiring high-bandwidth communication such as remote camera sensors or wireless audio.

5.9 Chapter conclusion

This chapter has provided the first ever experimental demonstration of vector modulated backscatter. Results were obtained from a device built from discrete components for 4-QAM and 16-QAM signalling. The 16 state modulator is capable of transmitting data at a rate of 96 Mbps for a total communication power efficiency of 15.5 pJ/bit.

This chapter validates vector modulated backscatter as a means for extremely low-power, high-data rate communication and has been demonstrated in a clutter-free indoor environment.

6

Adaptive channel equalization for wideband QAM backscatter

This chapter provides a description of the performance of QAM backscatter throughout a measured indoor backscatter channel. Due to the high data rate, the backscatter QAM signal is a wideband signal with respect to the channel and the received signal includes frequency-selective and multipath fading. The chapter describes a receiver designed for wideband QAM backscatter reception that implements adaptive equalization based on decision feedback equalizer (DFE). The equalizer adapts a set of filter weights to remove the frequency selective and multipath fading caused by the channel. Performance of the DFE receiver is evaluated in both simulated Rayleigh channels and a measured indoor channel.

Contributions in this chapter:

- Description of a receiver for wideband QAM backscatter
- Validation of the adaptive DFE against time varying backscatter channels
- Performance of wideband QAM backscatter throughout a measured indoor channel

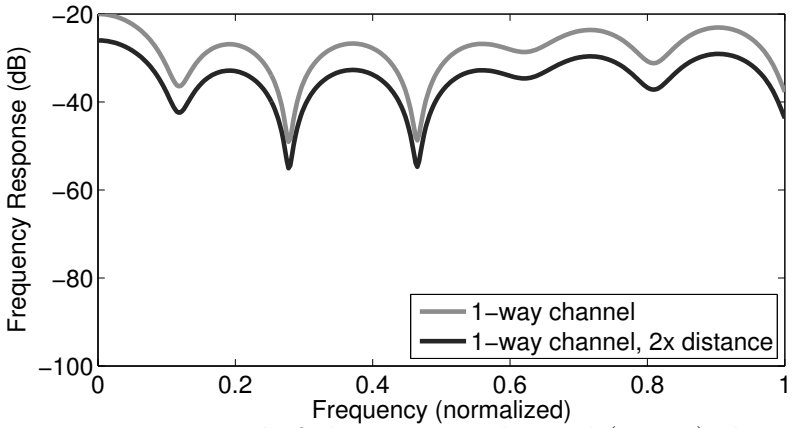

FIGURE 6.1: Example fading in a traditional (1-way) channel

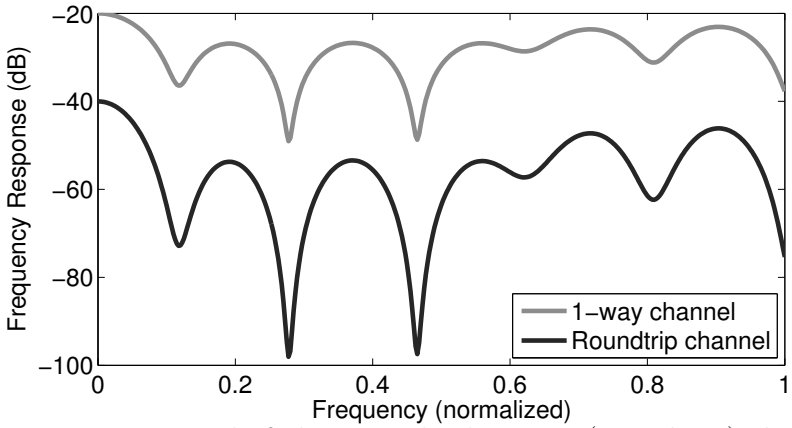

FIGURE 6.2: Example fading in a backscatter (roundtrip) channel

6.1 Fading in backscatter channels

A traditional communication channel is a one-way transmission with path loss is proportional to $1/r^2$. In a backscatter channel, the signal propagates as a round trip transmission and incurs both forward and return path loss. At first glance, attenuation in a backscatter channel may appear equivalent to a doubling of distance in a one-way transmission. However, this is not true as attenuation in a backscatter channel is proportional to $1/r^4$.

A comparison between fading in a traditional link and fading in a backscatter link is shown in Figures 6.1 and 6.2. In Fig. 6.1 an exemplary magnitude response

for a one-way link over a range of frequencies is shown. Doubling the communication distance reduces the magnitude response by by 6 dB over the entire frequency range. In contrast, Fig. 6.2 shows the magnitude response for a round trip (backscatter) channel. In this link, the signal is attenuated by the forward channel as well as the return channel resulting in much greater attenuation compared to the one-way link.

The backscatter channel exhibits deeper and broader nulls in the frequency response of the channel as compared to a traditional link. Similarly, the effects of time-varying fading in a backscatter channel result in faster and more pronounced changes within the channel response. For these reasons, it has remained an open question whether a channel equalizer could improve wideband data reception in a backscatter channel. In this chapter, a series of experiments are presented to analyze wideband backscatter QAM performance in both simulated as well as measured channels. These experiments demonstrate the first application of a channel equalizer in a backscatter communication system demonstrating a 59% improvement in average EVM compared to the unequalized signal.

6.2 Wideband backscatter channel system model

The general wideband backscatter channel system model used in this work is shown in Fig. 6.3. Further description and details of this model are available in the literature [70, 71]. In the model, a constant, CW signal is first sent through a reader transmit gain amplifier block. In the U.S., this output power is limited to +36 dBm EIRP, the transmit power summed with the peak antenna gain. The 'transmit gain' block in the model is tuned to simulate a total +36 dBm EIRP (4 W) signal output power. This narrowband, single tone CW output is then passed through a forward channel gain block. The attenuation and phase rotation of this block vary with tag location due to multipath interference. The attenuated forward link signal is then amplified by the gain of the tag antenna.

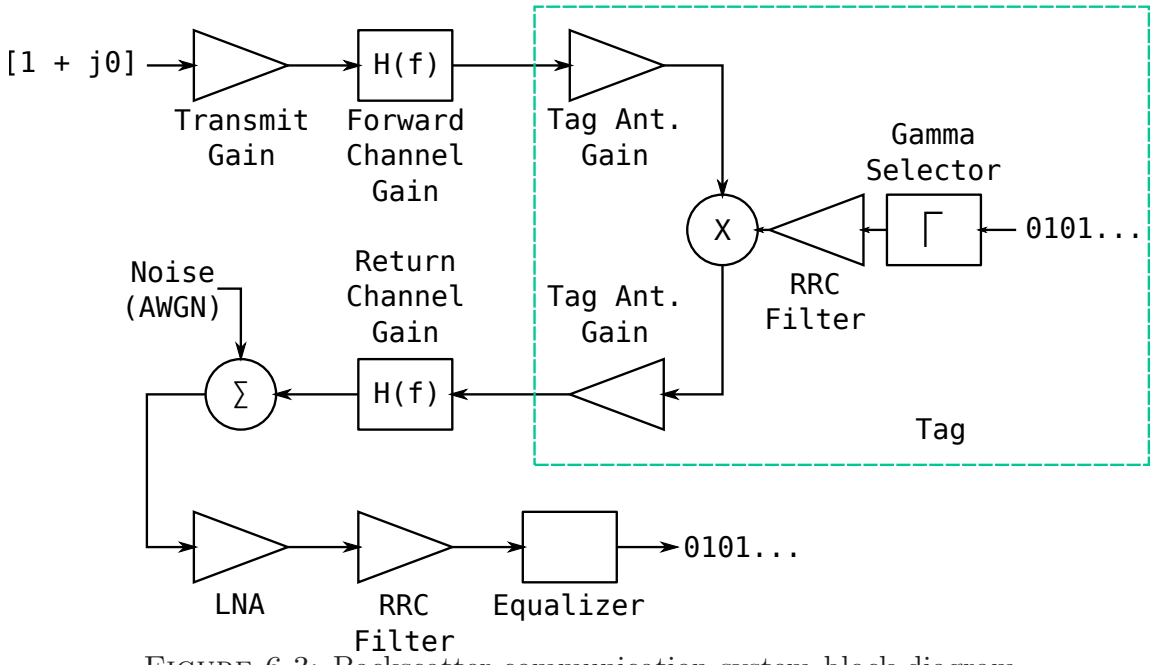

FIGURE 6.3: Backscatter communication system block diagram

For the tag model, binary input data is mapped to a QAM impedance symbol using a Γ^* symbol mapping block. This complex baseband symbol is upsampled to the simulation sampling frequency using a root-raised cosine filter. The upsampling ratio is determined by the simulation sampling frequency and data symbol rate.

The upsampled, complex baseband symbol is mixed with the tag incident signal and amplified by the tag antenna gain a second time before being sent over the return channel. The baseband data bandwidths used in this model extend from 1 MHz up to 20 MHz (4 Mbps and 80 Mbps, respectively, for 16-QAM signalling). As coherence bandwidth for backscatter channels may only be 1–3 MHz, the modulated signal is not narrowband with respect to the channel [70]. The return channel gain operates as a filter (the channel impulse response) that is applied to the modulated data signal. The return channel gain includes frequency-selective multipath fading and ISI introduced by the channel model. In this chapter, this model is applied to operation in simulated channel models (Gaussian and Rayleigh) and a measured

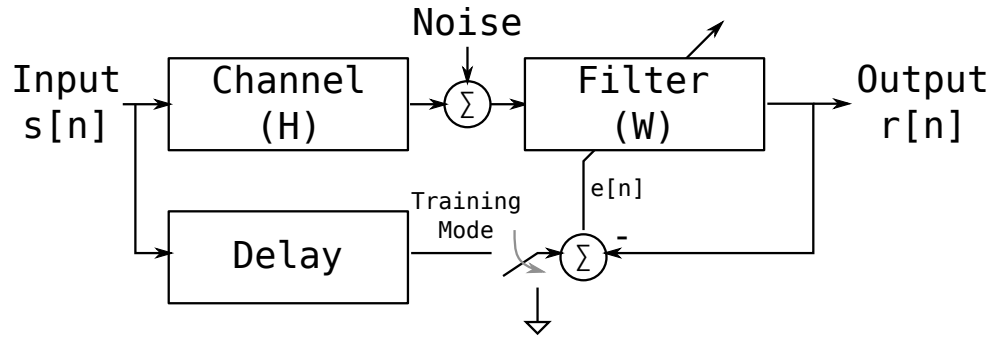

FIGURE 6.4: Linear channel equalizer block diagram

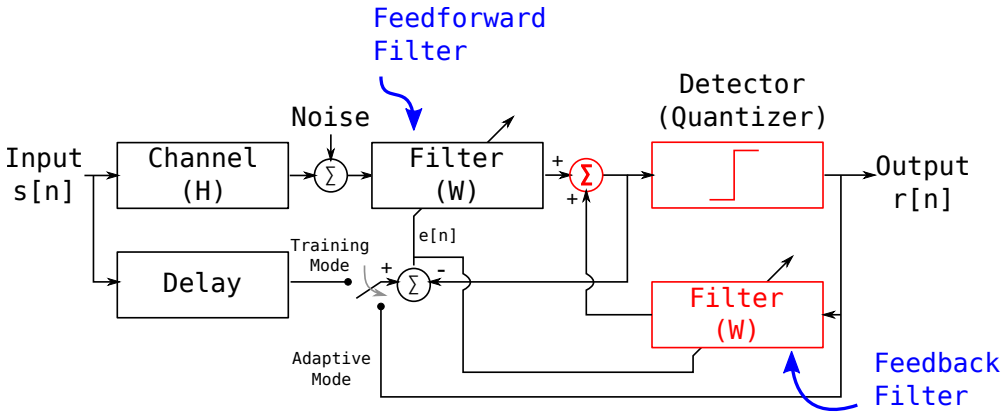

FIGURE 6.5: Decision feedback equalizer (adaptive) block diagram

indoor backscatter channel.

The signal incident at the receiving antenna (not shown) is passed into the QAM receiver which consists of a LNA with 30 dB gain, a matched filter (root raised cosine) for downsampling to the symbol rate, and a channel equalizer. Noise modelled as AWGN is added to the signal before downsampling conversion. Details of the equalizer and its effect on communication performance is discussed next in this chapter.

6.3 Overview of channel equalization

The block diagram for a communications system with a linear channel equalizer is shown in Fig. 6.4. The equalizer consists of a multi-tap digital filter with adjustable

tap weights. The goal of channel equalization is to compensate for the frequency selective fading effects of the channel and remove the resulting ISI.

This is accomplished in the system model by first transmitting known symbol data from a frame or packet preamble through the channel. During this training phase, the known data is used by the equalizer to update and adjust the filter tap weights in order to minimize the error between the known data and the filter output. The weights are updated according to a user-selectable optimization algorithm such least mean squares (LMS) or minimum mean square error (MMSE) algorithms. In the equalizer in this work, the recursive least squares (RLS) algorithm with a forget factor of 0.97 is used.

After the training period of the frame/packet preamble, the weights of a linear equalizer filter are set and stay constant for the balance of the frame. The final result is removal of the channel effects and an improvement in bit detection and data error rates.

An adaptive, nonlinear DFE is shown in Fig. 6.5. The additional blocks in this circuit, compared to the linear equalizer, are highlighted in red. The DFE splits the single filter into a feedforward filter and a feedback filter. A quantizer, which operates on the output from the feedforward filter, passes the quantized data to the feedback filter. The weights for both filters are determined by the summation of the two filter outputs. During training mode the known sequences are used to initially set the filter weights. After training, the quantized data is used to continually adapt and update the filter weights throughout the entire frame. Since the weights are determined by the output of a nonlinear quantizer operation, the DFE is considered a nonlinear operation.

The DFE has two main advantages over the linear feedback equalizer of Fig. 6.4. Since the feedback filter operates on the quantized, noiseless data, a better approximation of the channel effects can be formed and removed from the input data. A

second advantage is that the DFE continues to update the filter weights and coefficients after the training period is over. The adaptive filter is able to compensate for channel impairments that may change within the duration of a frame/packet transmission period.

For more detailed information, an excellent beginning source for adaptive equalization (and equalization in general) is the work of Qureshi [83].

6.4 Simplified simulation model for simulated channels

To characterize the equalizer performance, a simplified simulation model based on the general backscatter channel model is used. The simulation shown in Fig. 6.6 tests the performance of equalization in various channel models. This model is based on the linear function of the transmit gain, (narrowband) forward channel gain, and tag antenna gains in the general wideband model of Fig. 6.3. These functions are combined and applied to the return channel gain as a single complex multiplier. This simplifies the backscatter QAM simulation to that shown in Fig. 6.6 where the "channel" block includes the forward channel gains as well as the wideband return channel impairments and additional AWGN. The AWGN noise model is derived from a typical receiver thermal noise sensitivity (-88 dBm) and held constant for the duration of the simulation. As the tag location and backscatter channel change, the received signal power is also affected. For this reason all E_b/N_0 metrics presented in this chapter are measured at the receiver input port.

To better illustrate this simulation, an annotated version of the block diagram is shown in Fig. 6.7. The transmitted constellation is represented as a set of complex values shown in the upper left of the figure. After pulse shaping has been applied to the transmitted symbols, an eye diagram of the transmitted signal is shown for both the in-phase and quadrature signals. A heat map of the received signal after transmission through the channel shows exemplary scaling phase rotation caused by

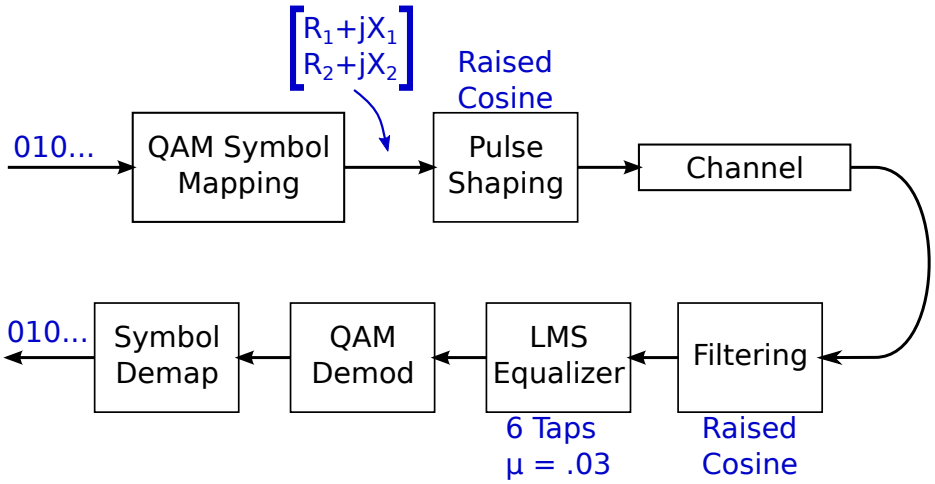

FIGURE 6.6: Simulation model for statistical channel models

the Gaussian channel. This received signal is then downsampled to baseband, filtered using the channel equalizer and then demodulated. The final annotation in the lower left compares the received symbols (blue dots), equalized symbols (red dots), and transmitted symbols (black dots). This simulation is the basis for the experiments of wideband QAM backscatter using channel models. A summary of the model details is shown in Table 6.1.

6.4.1 Frame format

The frame format for data transmission is shown in Fig. 6.8. In a single frame, 100 known training symbols are transmitted. This is followed by the payload which consists of 600 symbols and a tail of 20 symbols. The header and tail portions of the frame are constant for all transmissions throughout the simulation and random data for each frame is inserted in the payload. The simulation assumes perfect synchronization and knowledge of the training data at the receiver.

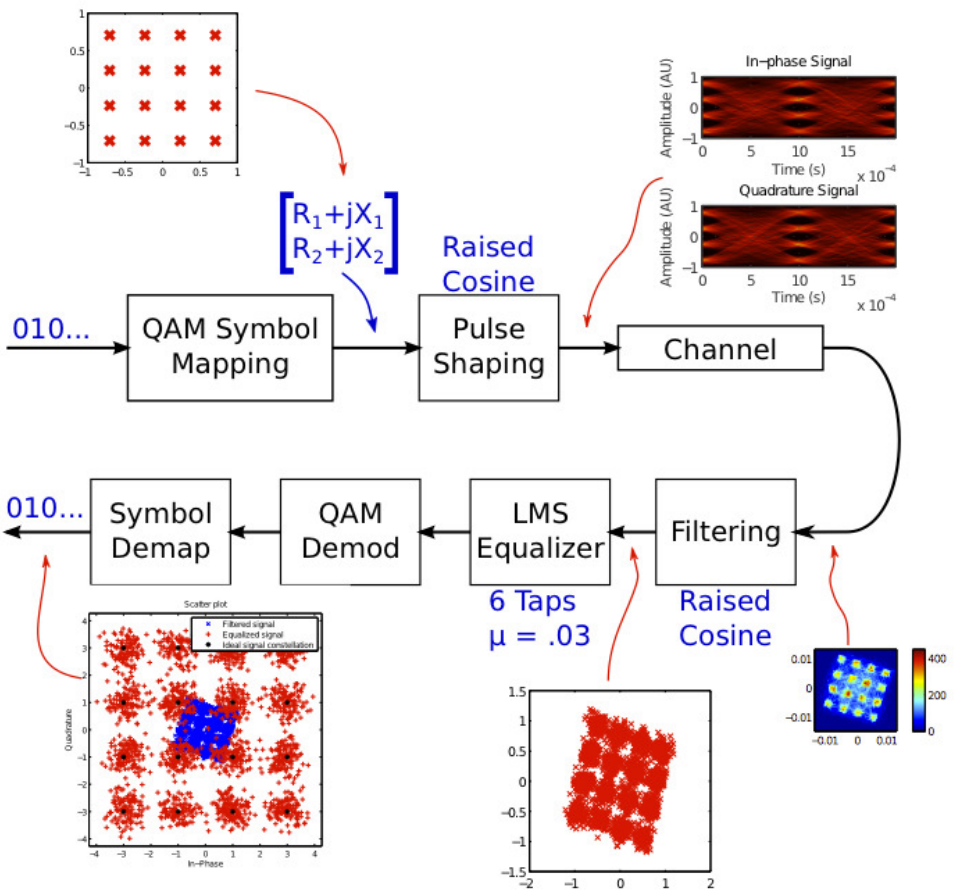

FIGURE 6.7: Annotated simulation model for statistical channels models

Header	Payload	Tail
100 Symbols	600 Symbols	20 Symbols
(Training Data)		

FIGURE 6.8: Frame format used in data transmission

6.5 Linear backscatter equalization in the Friis channel

Use of an equalizer in a Gaussian, or Friis channel [56], is investigated. The channel impairment models single-path propagation with the complex exponential

$$K = \alpha \cdot \exp(j\beta). \tag{6.1}$$

In the complex baseband, this expression attenuates and rotates the phase of the transmitted constellation. The linear equalizer filter therefore needs only to imple-

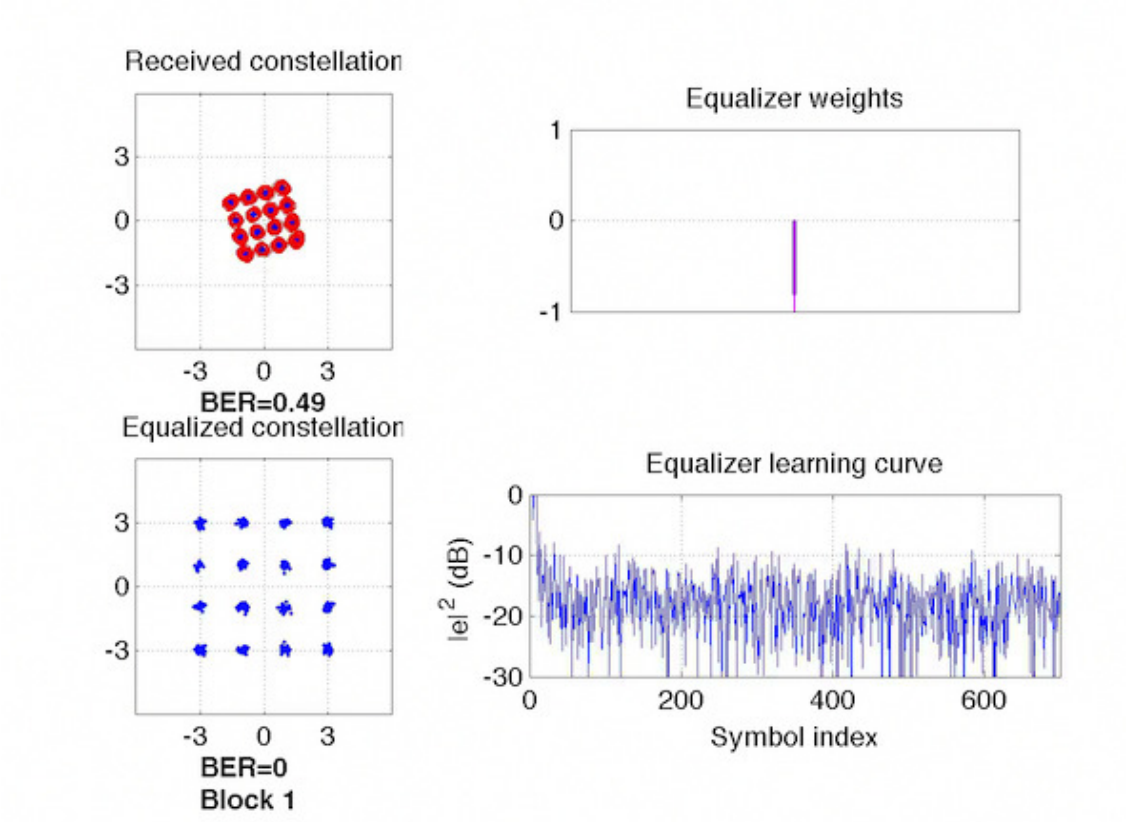

FIGURE 6.9: Single frame of simulation, Gaussian channel with linear equalizer

ment and adjust 1 filter weight (consisting of a real component and an imaginary component) to fully account for and remove the channel impairments.

Exemplary results from this simulation are shown in Fig. 6.9. While this figure represents a single frame (i.e. location) for a tag placed in a non-static channel, the simulation is approximates a moving tag. Shown in the results are the raw, received constellation in the upper left and the equalized constellation output from the receiver in the lower right. Blue indicates the received point, and a red circle around the blue dot indicates a symbol error. Bit error rates for the frame are below the constellation plots. The upper right plot shows the equalizer weights. For the Gaussian channel, only 1 tap with real and imaginary components are required. The blue line indicates the real portion of the tap weight and the magenta line indicates

the imaginary portion of the tap weight. Finally, the lower right plot displays the symbol error magnitudes after equalization over the duration of a symbol. The error magnitude falls quickly during the training phase of the frame and stays below 10 dB during demodulation of the payload.

This result shows that in the simple channel, a single tap equalizer can be implemented in a receiver for demodulation of QAM backscatter. Without equalization, accurate data recovery in such a channel is not possible. In this simulation, the tag is modulating data at a rate of 20 Msym/sec (aggregate link rate of 80 Mbps) on a carrier of 915 MHz with a 16-state C-Only backscatter QAM constellation centered around an incident carrier frequency of 915 MHz and a 50 Ω antenna. The channel is implemented as a single-path Rayleigh channel object in MATLAB with a maximum Doppler shift of 330 Hz.

The equalizer is implemented as a single tap equalizer with 1 real and 1 imaginary component per tap. The algorithm for updating the weights is the RLS algorithm with a forget factor (λ) of 0.97.

6.6 Linear backscatter equalization in the Rayleigh channel

Next, the effects of wideband QAM backscatter in a more realistic yet pessimistic channel model is shown. The Rayleigh channel models a radio channel where no line of site is present [68, 69, 73, 74]. For RFID environments, the Rayleigh channel serves as a pessimistic or worst-case scenario. Often a line of sight path will be present in backscatter communication situations where higher data transfer rates are possible.

The Rayleigh channel for this simulation models multipath effects from 3 separate paths with a maximum Doppler shift of 330 Hz. This introduces multipath ISI and attenuation and scaling of the transmitted constellation. An 8-tap linear equalizer is implemented with a RLS algorithm and forget factor (λ) of 0.97. In this simulation, the symbol rate is 20 Msym/sec (80 Mbps).

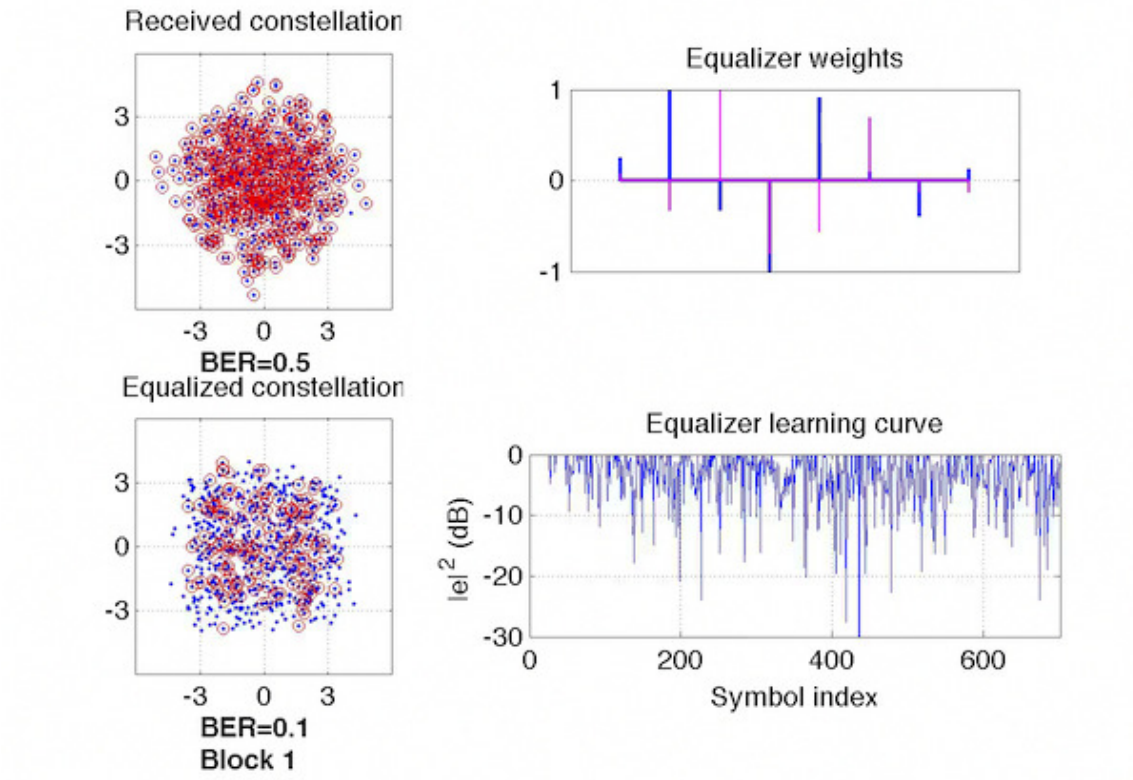

FIGURE 6.10: Single frame of simulation, Rayleigh channel with linear equalizer

As evident from the exemplary frame result shown in Fig. 6.10, the 8-tap equalizer is able to compensate for some of the channel impairments. This is best seen in the difference between the raw BER of 0.5 for the received, un-equalized and the BER of 0.1 for the received, equalized constellation. As the equalizer learning curve displays, the linear equalizer has a difficult time compensating for the channel effects and updating filter weights during the payload transmission. An adaptive solution is therefore required to mitigate the channel effects and keep the error low throughout a frame transmission.

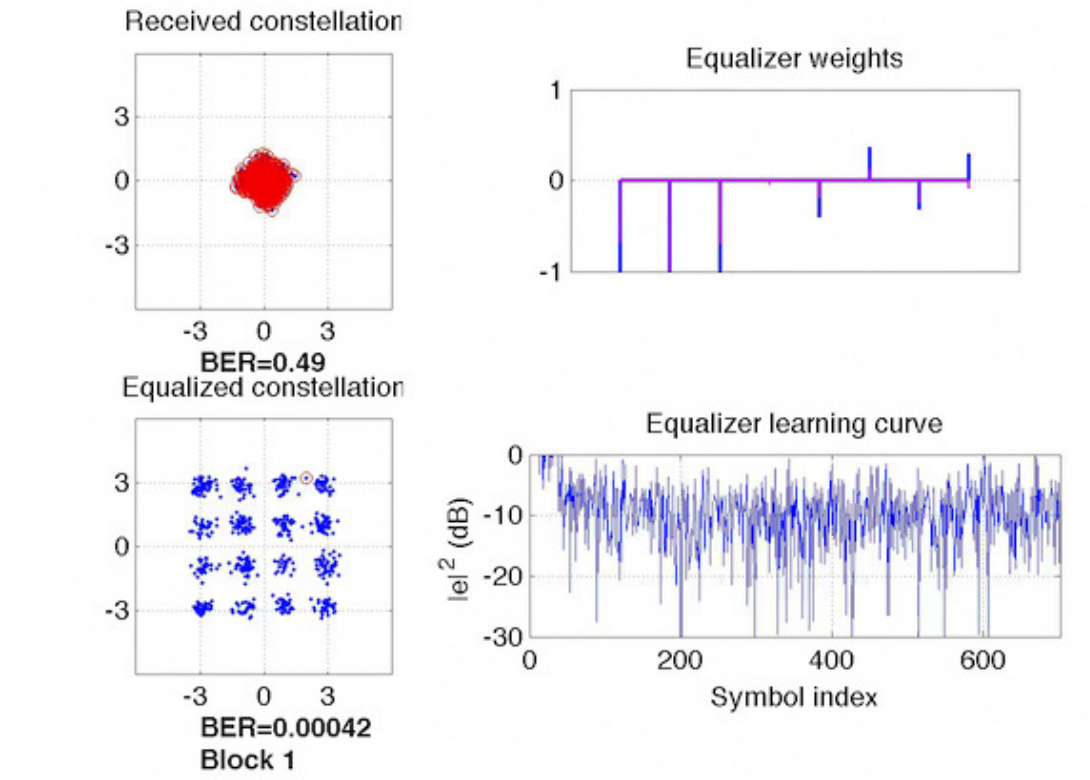

FIGURE 6.11: Single frame of simulation, Rayleigh channel with adaptive equalizer (DFE)

6.7 Adaptive backscatter equalization in the Rayleigh channel

As shown in the previous section, for a channel with multipath propagation, a linear equalizer is able to mitigate some of the channel effects but leaves room for improvement. For this reason, a nonlinear, adaptive DFE block is included in the receiver. This equalizer updates its weights through the frame using feedback from the detector. The equalizer consists of two filters – the feedforward filter and the feedback filter. In this simulation, the feedforward filter has 6 (complex) taps and the feedback filter has 2 (complex) taps for a total of 8 taps. The weight updating algorithm is again the RLS algorithm with a forget factor (λ) of 0.97. One minor difference to note is that DFE implementation operates at twice the clock speed of

Table 6.1: Details of the system model

Name	Symbol	Value
Carrier Frequency	f_c	915 MHz
Transmit Power	P_t	30 dBm
Transmit Ant. Gain	G_t	6 dBi
Transmit EIRP	P_{EIRP}	36 dBm
Receive Ant. Gain	G_r	6 dBi
Tag Ant. Gain	G_{tag}	3 dBi
Receiver Sensitivity	-	-88 dBm
Equalizer Algorithm	-	RLS
RLS Forget Factor	λ	0.97

the linear equalizer and uses 2 samples per symbol.

Using the same Rayleigh multipath channel with 3 paths and a maximum Doppler shift of 330 Hz, the results from the receiver implementing DFE are shown in Fig. 6.11. While the raw, received un-equalized constellation has a BER of 0.49, the received equalized constellation has a BER of 0.00042. The adaptive updating of the filter taps can also be interpreted from the equalizer learning curve. There are times when the symbol error starts to rise, but due to the adaptive decision updating, once again drops back down. This is most evident around symbol index 600 where a rise followed by a fall in the error can be seen.

Even in the pessimistic, non line-of-sight Rayleigh channel model, the adaptive equalizer is able to adapt to the changing multipath channel and greatly decrease the receiver error for the 16-QAM backscatter transmission. Based on these simulations using statistical models of channels, the DFE is selected for use in the receiver intended for demodulation in measured, indoor channels.

6.8 Measured wideband QAM backscatter

A backscatter channel is fully characterized by the forward and return channel gains [70,71,75]. This can be observed in the wideband backscatter model shown in Fig. 6.3.

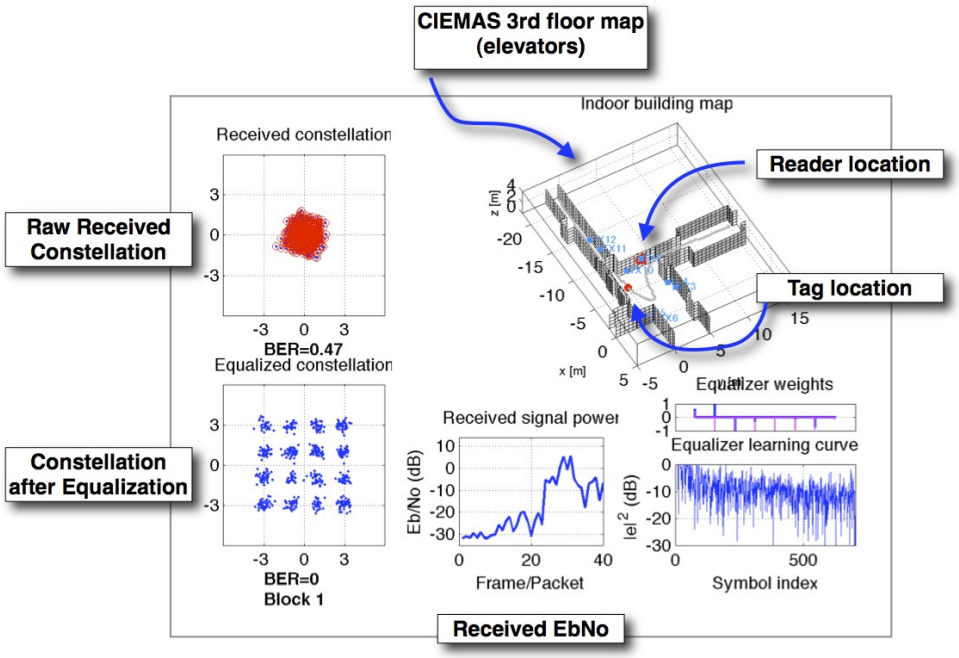

FIGURE 6.12: Annotated description of the measured channel results screen

In order to validate wideband backscatter QAM performance, an indoor backscatter channel was measured over varying frequency and location within an indoor hallway. The author extends thanks to Dr. Daniel Arnitz for sharing the channel measurements used in this work.

6.8.1 Channel measurement setup

The 3rd floor of the Fitzpatrick Center for Interdisciplinary Engineering, Medicine and Applied Sciences (CIEMAS, address: 101 Science Dr, Durham, NC 27705) was chosen as the measurement location. This area consists of a long corridor, an open area with elevators on one side and windows on the opposing side, and a glass "bridge" connecting two wings of the building. The measurement setup for this experiment is documented and described elsewhere [75,84]. This area includes highly reflective multipath surfaces from the two metal elevator doors as well as the large glass windows.

For the measurement, a MIMO transceiver was built using a set of distributed transmit antennas and receive antennas connected via cables and switches to a vector network analyzer (VNA). The transmitting antennas remained in fixed positions while the receiving antenna were moved throughout the environment. The system was controlled via a computer running MATLAB software. To measure the forward and return channel transfer functions for a tag, the receive antennas were affixed to a mobile cart that was moved throughout the indoor environment. At each location, the VNA recorded the frequency response for each set of antenna combinations. This data was used to measure the channel transfer functions and find the complex baseband channel impulse response. The measurement was performed over the frequency band from 0.1 – 2 GHz in 2 MHz steps using 2 dBi antennas (near-omnidirectional). Since omnidirectional antennas were used for the entire experiment, the channel represents worst-case scenarios. Switching to directive antennas "aimed" toward the receiving antenna would result in improved multipath performance compared to this measurement. The final measurement result allows for backscatter communication performance to be evaluated throughout a measured channel that includes location dependent ISI resulting from multipath and location dependent attenuation and phase-rotation.

6.8.2 Results

Motion of the backscatter tag was simulated in MATLAB. A motion path was created where the tag was moved through the corridor, the main area surrounding the elevators and glass, and then across the bridge. At each location, a frame was transmitted from the tag to the receiver following the model of Fig. 6.3. A CW signal was transmitted through the measured forward channel to the tag. The measured tag reflection coefficient modulated the incident carrier signal by mapping the input data stream to the corresponding impedance and reflection coefficient combination.

Table 6.2: EVM for varying data rates in the measured channel (DFE receiver)

Symbol Rate	Link Rate	EVM†	EVM†(dB)
20 MHz	80 Mbps	0.4892	-3.11
5 MHz	20 Mbps	0.2325	-6.33
2 MHz	8 Mbps	0.1928	-7.15

†*Avg. value, initial corridor (first 60 locations) ignored.*

This modulated data was upsampled using a root raised cosine filter and passed through the wideband return channel. The signal at the receiver was then passed through a 30 dB LNA before matched filter downsampling and equalization. Noise (AWGN) was added at the receiver, before downsampling, to model a reader with a thermal-noise limited sensitivity of -88 dBm.

The equalizer implementation was selected based on previous simulations. A nonlinear, adaptive DFE with 8 total taps (6 feedforward, 2 feedback) was chosen. The weight update algorithm was RLS with forget factor (λ) of 0.97.

A screenshot of the measurement results window is shown in Fig. 6.12. In the upper left, the raw, un-equalized constellation is shown. Below this, the equalized constellation is shown. For both constellations, a blue dot is a received symbol and a red circle surrounding the blue dot represents a symbol error (incorrectly demodulated symbol). The map of the measurement area is shown in the upper right. The reader (transmit and receive antenna) is shown in the middle of the map as a red dot. The second red dot indicates the current tag location. The tag location is moved throughout the environment following the gray path. Finally, the received E_b/N_o (referenced to the receiver input port) is shown as well as filter weights and equalizer error or learning curve.

As expected from previous model-based channel simulations, the equalizer greatly reduces BER and improves receiver performance. A BER curve for 8 Mbps data rate from the tag for all 176 measured locations along the path through the environment

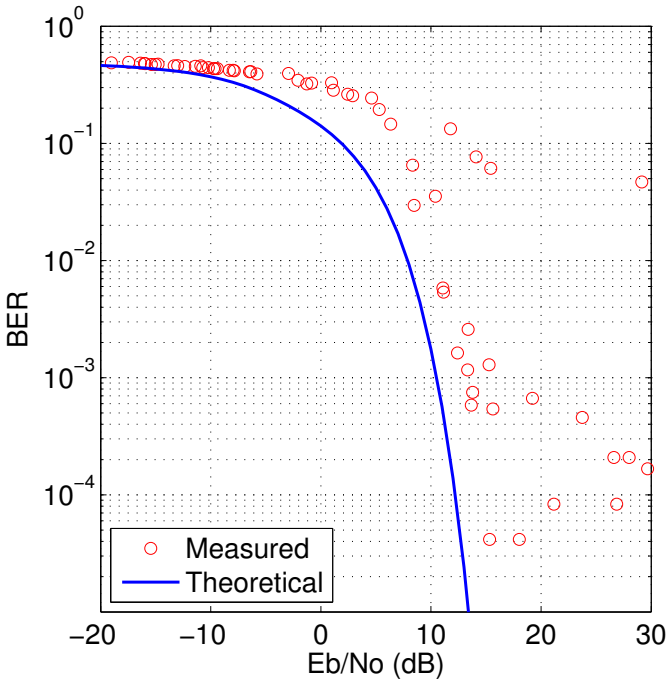

FIGURE 6.13: Measured BER "waterfall" for backscatter 16-QAM in the indoor channel where E_b/N_0 varies with tag position

is compared to theoretical 16-QAM curve, generated from MATLAB's `bertool`, in Fig. 6.13. The measured values are close to the theoretical limit. A second plot in Fig. 6.15 shows the E_b/N_0 power at the receiver for all positions of the tag throughout the simulation. In this plot, locations where the received E_b/N_0 was below 16 dB are marked in red to indicate dropouts in performance caused by poor signal-to-noise ratio at the receiver.

In the measurement setup, the measured channel impulse response has a bandwidth of 200 MHz. Symbol rates from the tag were varied from 1 MHz to 20 MHz and performance was evaluated as seen in Fig. 6.14. The data are shown in Table 6.2 in tabular form. Since lowering the data rate increases average bit energy, it follows that increasing the data rate increases average EVM. For a link rate of 8 Mbps, an average EVM of -7.15 dB is measured. However, for the link rate of 80 Mbps, a EVM of -3.11 is measured. This value of EVM is found after ignoring the initial locations

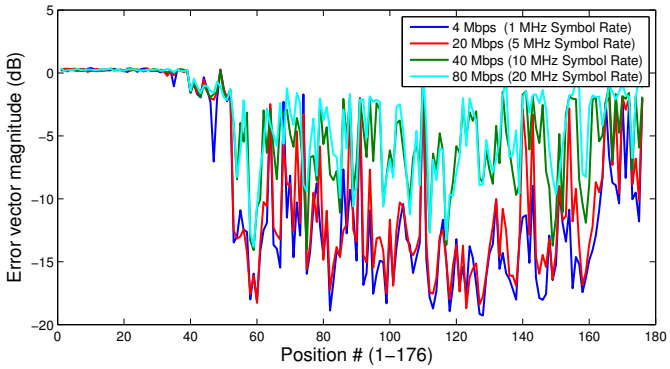

FIGURE 6.14: EVM for varying data rates in the measured indoor channel

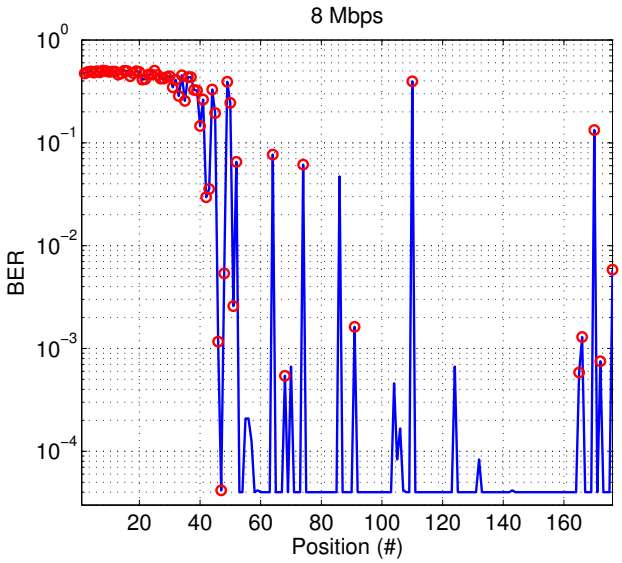

FIGURE 6.15: BER over all positions in simulation

in the corridor where no data is able to be detected due to high attenuation along the forward and return paths.

Though average EVM is a useful comparison metric, a histogram of the received EVM better illustrates the impact of the equalizer on system performance. In Fig. 6.16, a histogram of the received EVM for a data rate of 20 Mbps is shown. Figure 6.16(a) shows EVM performance when using a linear equalizer at the receiver. This histogram shows error values clustered around three locations indicating positions where the equalizer fully compensates for channel effects (EVM$\approx 10^{-1}$), posi-

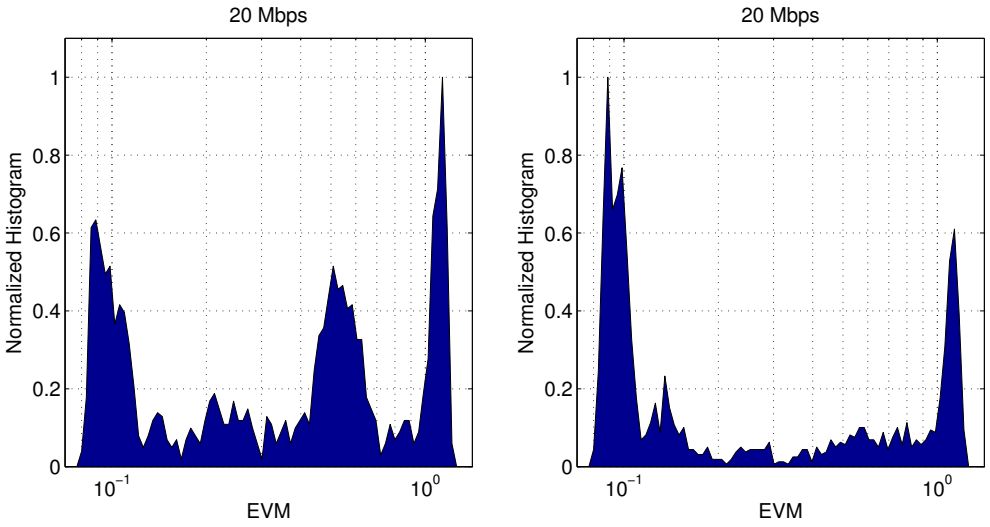

linear equalizer (a) decision feedback equalizer (b)

FIGURE 6.16: Histogram of EVM for 20 Mbps data rate with (a) linear equalizer and (b) DFE

tions where the equalizer has partial effects (EVM$\approx 10^{-0.6}$) and positions where the equalizer does not work (EVM$\approx 10^{0}$). However as Fig. 6.16(b) shows, the adaptive equalizer further improves EVM performance. Using the DFE, errors are clustered around two points where the equalizer is able to fully compensate for the channel impairments (EVM$\approx 10^{-1}$) and where the equalizer cannot function due to poor received signal-to-noise ratio (EVM$\approx 10^{0}$). When no equalization is used at the receiver, the system is unable to detect and recover any data from the tag. With an average EVM of approximately 100% for the unequalized data, the DFE operates with a 59% improvement in average EVM at a 20 Mbps data rate. Compared to the linear equalizer, the DFE operates with a 9% improvement in average EVM for a 20 Mbps data rate.

6.9 Chapter conclusion

This work is the first investigation of adaptive equalization for backscatter QAM systems. The results show that backcsatter QAM is feasible in highly multipath indoor channels. Data rates of 20 Mbps were possible throughout the surveyed area with isotropic (0 dBi) antennas used in measurement. However, this rate could be improved with directive antennas and/or additional reader transmit power.

This chapter has shown the characterization of wideband QAM backscatter in simulated model-based channels as well as measured indoor channels. A nonlinear, adaptive equalizer with decision feedback was implemented in the receiver to mitigate channel impairments such as multipath ISI. A general wideband backscatter channel model was provided as well as a simplified simulation model both including a receiver structure that includes channel equalization. Results were shown for performance in simulated channel models as well as a measured indoor channel. The equalizer was able to successfully remove the channel effects and allow for the transmitted data from the tag to be recovered. For a data rate of 20 Mbps, the adaptive equalizer improves average EVM performance by 9% compared to a linear equalizer and 59% average EVM improvement compared to the unequalized signal.

7

A single-chip backscatter neural/EMG telemetry system

An integrated, single-chip, high-data rate binary phase shift keying (BPSK) backscatter system is described. The device operates with a data rate of 5 Mbps, well beyond the traditional limitation of 640 bps [14]. This enables unique low-power sensing applications such as remote biosignal acquisition and passive wireless audio recording.

Two experiments are described: the first is a highly integrated chip that includes a digital backscatter modulator for communication and is designed to wirelessly record 10 neural and 4 electromyography (EMG) inputs from a dragonfly in flight. Without the high-data rate backscatter modulation, as this chapter will show, achieving the required bandwidth at such a low power cost is not possible. Secondly, this chapter presents the first ever experimental transfer of audio and images using digitally modulated backscatter. These applications present a glimpse into the future of backscatter technology as it will be used to transport increasing amounts of data. The binary backscatter communications system used by this chip serves as a baseline for

next-generation multi-state vector backscatter modulator systems.

This chapter is based on collaborative work by the author [7, 8, 30]. The author's contributions to the publications presented here include physical layer and radio architecture simulation, design and characterization, as well as power-harvesting circuitry simulation and design, design of experimental tests for validation and evaluation, reader analog component design and testing, and overall system performance characterization.

Contributions in this Chapter:

- Description of a backscatter based wirelessly powered system for wireless, in-flight multichannel biosignal recording of freely-moving insects.
- First demonstration of a "rich-media" backscatter tag capable of streaming multichannel digital audio and image transmission (5 Mbps, 4 pJ/bit)

7.1 Wireless neural recording

This section[1] describes a fully-passive wireless neural recording solution for freely-moving insects. The study of neural activity during behavior is a topic of intense interest in neuroscience, but progress is often slowed by the difficulty of measuring the activity of multiple neurons in a moving animal. For example, dragonflies are predatory insects that catch prey on the wing, intercepting their targets during prey capture flights of 0.5–1.0 m in distance [85]. Dragonflies of the species *Libellula lydia*, which initiate foraging flights from a perch, weigh about 400 mg and can maintain their interception behavior with payloads of up to 33% of their body weight, or about 130 mg. This small payload capacity presents severe challenges for designing

[1] Portions of this chapter are a derivative of previously published work, ©2012 IEEE. Reprinted, with permission, from Thomas et al., "A battery-free Multichannel Digital Neural/EMG telemetry system for flying insects," IEEE Transactions on Biomedical Circuits and Systems, October 2012.

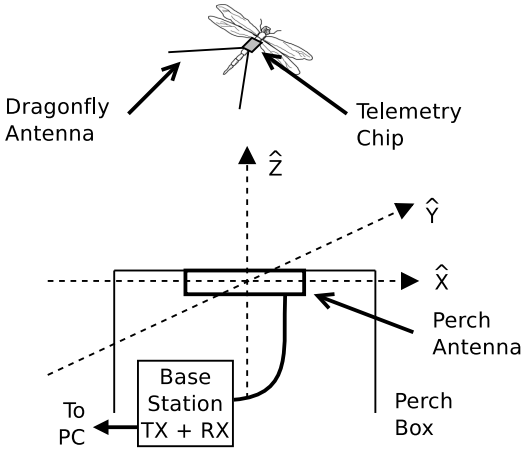

FIGURE 7.1: Experimental setup in the dragonfly flight arena [©2012 IEEE]

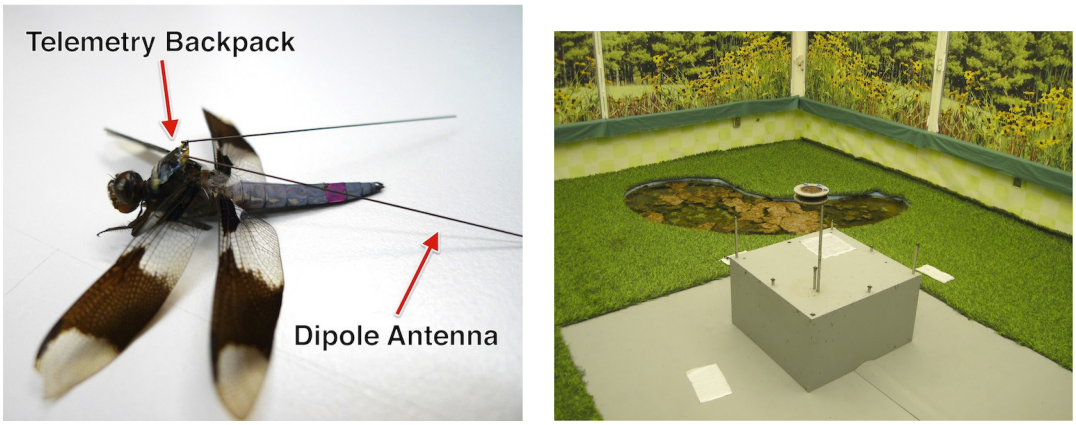

(a) (b)

FIGURE 7.2: Photographs of the wireless telemetry package mounted on a dragonfly (a) and the dragonfly perch and reader enclosure (b) inside the flight arena [©2012 IEEE]

instrumentation that can measure the electrical activity of one or more neurons in the dragonfly nervous system during flight.

The weight and volume associated with bulk energy storage devices such as batteries or supercapacitors are the primary concerns in achieving long run-times in such small animals. The system described here addresses this challenge by eliminating bulk energy storage from the telemetry device altogether.

The experimental setup in the dragonfly flight arena is shown in Fig. 7.1. The

dragonfly being studied carries a dipole antenna attached to a chip-on-flex telemetry package. Prey capture experiments take place in the volume of space above a perch box enclosing the perch antenna as well as the reader transmitter (BSTx) and receiver (BSRx). The coordinate system shown in Fig. 7.1 is used throughout this work to describe the working volume above the perch box. A photograph of the telemetry module attached to a dragonfly and a photograph of the perch and reader enclosure are shown in Fig. 7.2.

A block diagram of the telemetry system is shown in Fig. 7.3. All of the energy required to operate the device is transmitted wirelessly in the form of an ultra-high frequency (UHF) radio signal that originates from a base-station transmitter mounted in the perch box. This signal is coupled by means of far-field (radiative) coupling to a dipole antenna carried by the dragonfly, and converted to DC operating power by means of an on-chip RF power harvesting circuit.

Wireless power transmission is generally found to be inefficient when the untethered device moves over a large operating volume. This includes the 0.5-1 m region above the dragonfly perch where particularly interesting prey capture behavior occurs. In this system, a +36 dBm (4 W) transmitter is used as the power source, but as little as a few milliwatts may be available from a dragonfly-carried dipole in the far field. This is because the transmitted power in the far field is spread over a wide area, resulting in a low power density. In an unobstructed and uncluttered environment with minimal multipath, the energy available at the receiving antenna decreases with the path loss as $1/r^2$. Power consumption in the telemetry IC must therefore be minimized in order to maximize the distance from the transmitter at which the IC can operate reliably from harvested energy alone.

Modulated backscatter is produced at the telemetry IC by modulating a FET to switch a time varying, deliberate impedance mismatch across its antenna terminals. This results in a time varying scattered field from its antenna. The modulating FET

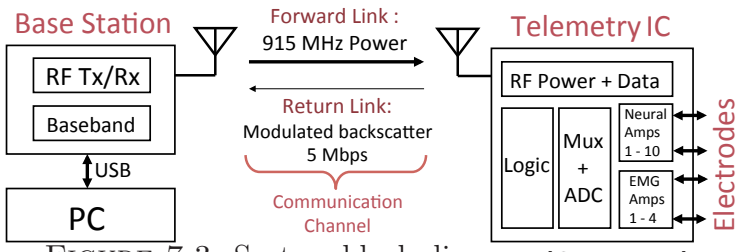

FIGURE 7.3: System block diagram [©2012 IEEE]

is driven by a 5.0 Mbps BPSK data stream carrying the desired telemetry data.

As has been previously shown, modulated backscatter has the benefit of repartitioning much of the circuit complexity and power consumption of the communication link from the telemetry IC to the reader. The backscatter modulator is extremely simple, consisting only of a modulating FET and a MIM capacitor. From a power consumption point of view, the modulated backscatter uplink avoids the use of an on-chip UHF oscillator, or a frequency synthesizer, which are significant contributors to the overall power consumption of previous telemetry ICs. Because of the power efficient communication modality, the wireless data uplink accounts for only 2%, or 24.6 μW, out of the total DC power consumption of 1.23 mW.

7.2 Related work

Table 7.1 compares the most important features of this work against representative wireless telemetry systems from the literature. Most reported wireless multi-channel neural telemetry systems have masses in the 30–60 g range and require a large battery pack for extended operation [86–88]. Miniaturized wireless neural recording systems weighing less than 1 g have been built by reducing the number of neural channels, battery size, and operating range [6, 54, 55, 89–94]. A system mass of even 1 g may still be excessive when studying very small animals, or in chronic experiments where a non-irritating package placement is critical to ensure normal animal behavior. This work represents a continuation of earlier efforts [6] to develop wire-

less instrumentation that allows less kinematically invasive measurements from very small animals.

Power requirements present the greatest obstacle to achieving successful data capture from very small animals such as flying insects. Even state-of-the-art ultra-lightweight battery powered systems are fairly heavy (170 mg) with the bulk of this weight (130 mg) being associated with a 1.5 V silver oxide battery [6]. We have addressed this challenge by eliminating the battery entirely with the on-chip UHF (902–928 MHz) power harvesting subsystem that extracts the chip's operating power from incident RF energy supplied by a transmitter and antenna mounted beneath the dragonfly's perch.

In contrast to commonly used inductive coupling for power transfer, far-field radiative coupling at UHF frequencies can operate with small and lightweight dragonfly-sized dipole antennas at distances of several meters, depending on telemetry system power consumption and available transmitter power. Related work in biotelemetry ICs powered by UHF energy harvesting includes [47, 95]. This work improves on these prior examples in signal fidelity (ADC resolution), bandwidth, channel count, and package mass, as well as presenting a complete system including both the telemetry IC and a suitable reader with a USB connection to a PC for data storage and analysis.

The telemetered bandwidth and number of channels are key aspects of system engineering. Many of the most pressing questions in systems neuroscience relate to understanding the role of specific neurons within a circuit, so signals must be measured in a manner that preserves their identity. Telemetering event times based on a threshold is insufficient because the identity of the neurons is lost. Extracellular electrodes, such as those used in awake behavior experiments, measure the summed activity of multiple neurons. These signals must then be sorted back into the activity of individual cells. There are well developed tools that facilitate such "spike sort-

Table 7.1: Comparison of Selected Low-Power Wireless Biotelemetry Systems [©2012 IEEE]

	Ando [55]	**Takeuchi [94]**	**Mohseni [54]**	**Yeager [47]**	**Harrison [6]**	**This Work**
Year	2002	2004	2005	2010	2011	2012
Power Consumption	3.6 mW	10 mW	2.2 mW	16.56 μW	1.0 mW	1.23 mW
Signals Transmitted	2 EMG	1 neural	3 neural	1 temperature	2 neural 2 EMG	10 neural 4 EMG 2 auxiliary inputs
Signal Bandwidth	200Hz–2kHz	20Hz–10kHz	50Hz–9.1kHz	50Hz	300Hz–5.2kHz (neural) 20Hz–280Hz (EMG)	250Hz–10kHz (neural) 5Hz–700Hz (EMG)
Operating Range	5 m	16 m	0.5 m	3 m†	2 m	1.5 m‡
Battery Life	0.5 h	0.5 h	*(Not Described)*	Battery-free	5 h	Battery-free
Total Mass	250 mg	100 mg (w/out battery)	1100 mg	250 mg	170 mg	38 mg
Approximate Size	7.5 x 6.25mm	15 x 8mm	17 x 12mm	9.1 x 7.3mm	6 x 5mm	6.8 x 4.6mm
Off Chip Components	*N/A*	18	3	16	1	3
Supply Voltage	1.55 V	3.0 V	3.0 V	1.8 V	1.5 V	1.31 V
Telemetry Frequency	82–85 MHz	85 MHz	96 MHz	902–928 MHz	905 MHz	902–928 MHz
Telemetry Modulation	analog FM	analog FM	analog FM	digital backscatter	digital FSK	digital BPSK backscatter
Target animal(s)	hawkmoth	cockroach	marmoset monkey	hawkmoth	locust, elec. fish, dragonfly	dragonfly

† Using commercial off-the-shelf (COTS) EPC Gen 2 UHF RFID reader

‡ Assuming transmitter power of +36dBm and antenna gain of 9dBi

ing" [96], but they use computational methods difficult to embed on-chip [97] and generally require the full analog waveforms seen on the electrode to perform well. It is preferable to record sampled time series data for each electrode for maximum flexibility in spike sorting and analysis.

In the dragonfly, there are ≈ 16 target-selective descending neurons (TSDNs) that appear to control interception based steering [98]. At flight temperatures of 35° C, TSDNs have action potential spikes of ≈ 250 μs in duration. These action potentials must be sampled at 25–40 kHz in order to have sufficient resolution to allow accurate neuron identification. Extracellular action potential spikes seen in the dragonfly can be 4 mV in amplitude, on background noise levels of 10 μV RMS or smaller. Careful attention to amplifier noise, ADC resolution, and gain distribution are critical to achieving high quality signal recording.

7.3 Wireless power and backscatter communication link design

Recent work in passive UHF RFID has demonstrated long-range operation of battery-free tags with power consumption as low as a few microwatts [43]. Passive UHF RFID tags harvest their operating power from the incident RF signal and return their stored data via modulated backscatter. These wireless links can be described in two parts: a *forward link* responsible for power transmission to the remote device and a *return link* that carries stored data from the tag back to the reader. In some systems the forward link additionally transmits commands to the remote device, but the system described in this paper employs unidirectional communication only. These links are described individually in the following sections.

7.3.1 Wireless power (forward link)

In an uncluttered far-field radiative power transfer regime, the well-known Friis free space model describes the RF power available at the telemetry IC's power harvester

as a function of key system parameters

$$P_{\mathrm{Rx}} = \frac{P_{\mathrm{Tx}} G_{\mathrm{Tx}} G_{\mathrm{Rx}} \lambda^2}{4\pi r^2} \propto \frac{1}{r^2} \tag{7.1}$$

where P_{Tx} is the transmitter's conducted RF output power, G_{Tx} is the transmitting antenna gain, G_{Rx} is the receiving antenna gain, and λ is the operating wavelength. A thorough discussion of the limitations of the Friis model in practical environments and the practical constraints on the model parameters is available in the UHF RFID literature [43, 68, 99–101].

The system described is designed to operate in the 902–928 MHz FCC Part 15 Industrial, Scientific, and Medical (ISM) band, which corresponds to a wavelength of approximately 33 cm. The reader transmit antenna (Laird Technologies S9028PCR) is circularly polarized and has a manufacturer's specified gain of 9 dBi. The reduced-size dipole used on the dragonfly is assumed to have a gain of approximately 0 dBi. Given a measured power-up RF sensitivity of +7.76 dBm and an measured harvester efficiency of 20.6% (including mismatch loss), the telemetry system has a forward link limited maximum operating distance of around 1.91 m, assuming free space propagation. The forward link budget is summarized in Table 7.2.

Because the presence of a human experimenter could disrupt the dragonfly and prey behavior, humans are excluded from the flight arena while the transmitter is on and experiments are being performed. Nevertheless, following the FCC's Maximum Permissible Exposure guidelines [102], we applied Eq. 7.2 to calculate a minimum safe distance beyond which the continuous-exposure power density limit of 3.05mW/cm^2 at 915 MHz is not exceeded. The power density S is given by

$$S = \frac{P_{\mathrm{Tx}} G_{\mathrm{Tx}}}{4\pi d^2} \tag{7.2}$$

where P_{Tx} is transmitted power in appropriate units (mW), G_{Tx} is the transmit antenna gain as a linear factor, and d is the antenna-to-human distance in cm. We thus calculate a minimum safe distance of 29 cm when the transmitter is on.

Table 7.2: Wireless Biotelemetry Power Link Budget

Transmitter output power	P_t	36 dBm
Transmitter antenna gain	G_t	9 dBi
Receiver (insect) antenna gain	G_r	0 dBi
Operating wavelength	λ	33 cm
Received power at IC input terminals	P_r	7.76 dBm
IC power harvester + mismatch efficiency	η	20.6 %
DC power consumed by IC	P_{th}	1.23 mW
Power-up threshold distance	$r\|_{P_r\,=\,7.76\,\text{dBm}}$	1.91 m

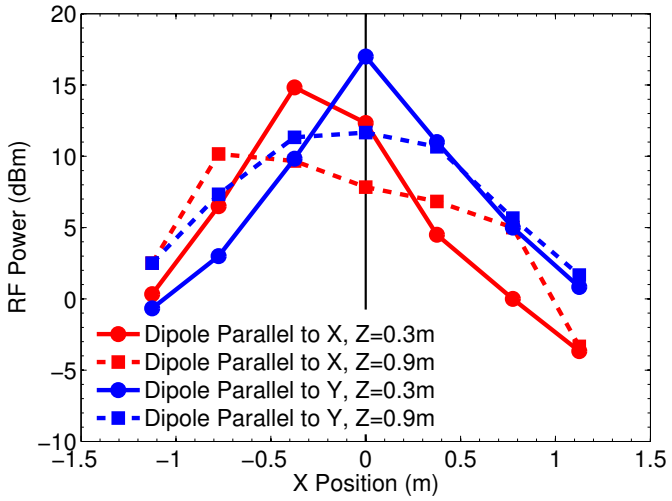

FIGURE 7.4: Measured RF power in an indoor environment vs. test dipole position, range, and polarization. Transmitter power is +36dBm [©2012 IEEE]

Since the dragonfly flight arena contains reflective objects, it is not a true free space environment. To better predict the spatial extent where the chip will receive adequate operating power, a series of measurements were taken in the lab environment with a reference dipole connected to an accurate RF power meter (Agilent N1913A). The transmitter was set to deliver +36 dBm conducted power to the 9 dBi gain circularly polarized antenna. Measurements presented in Fig. 7.4 show the effects of non-ideal circular polarization (elliptical polarization) in the transmitting antenna, as well as some degree of multipath propagation in the lab.

An ideal circularly polarized transmitting antenna in a multipath-free environ-

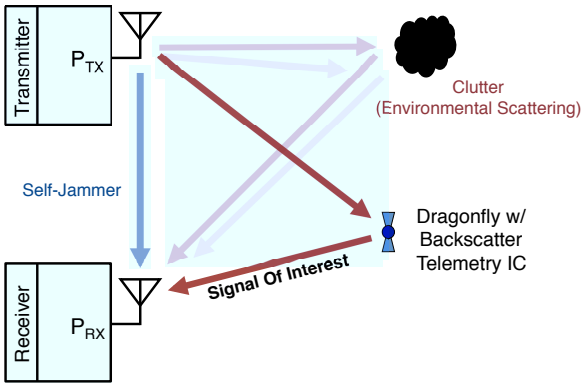

FIGURE 7.5: Signals present at the receiver in a backscatter communication link [©2012 IEEE]

ment would yield a near-constant available power in the critical ≈1 m^3 volume directly above the transmitter antenna where interesting animal behavior is expected. For certain combinations of position and polarization, less than the +7.76 dBm needed to power the IC is observed in these measurements. This has been addressed initially by increasing the transmitted power to compensate for the observed non-ideal propagation. Future work includes a careful study of transmitting antenna radiation pattern and polarization by measurement in the actual operating scenario rather than reliance on the manufacturer's published specifications.

The on-chip power harvester (rectifier) circuit that is used to convert the available RF power into DC power for chip operation is described in detail in Section 7.4.3.

7.4 The digital telemetry IC

The telemetry IC is highly integrated, with a block diagram shown in Fig. 7.6. The die is 2.36 mm x 1.88 mm x 250 μm thick. The die layout is shown in Fig. 7.7. Only three off-chip components are required for operation, comprising a miniature 20 MHz quartz crystal and two 0402 SMD bypass capacitors for the unregulated and regulated power supplies V_{unreg} and V_{reg}. The crystal provides precise clocks for analog to digital converter (ADC) sampling and data clock synchronization. The flight package

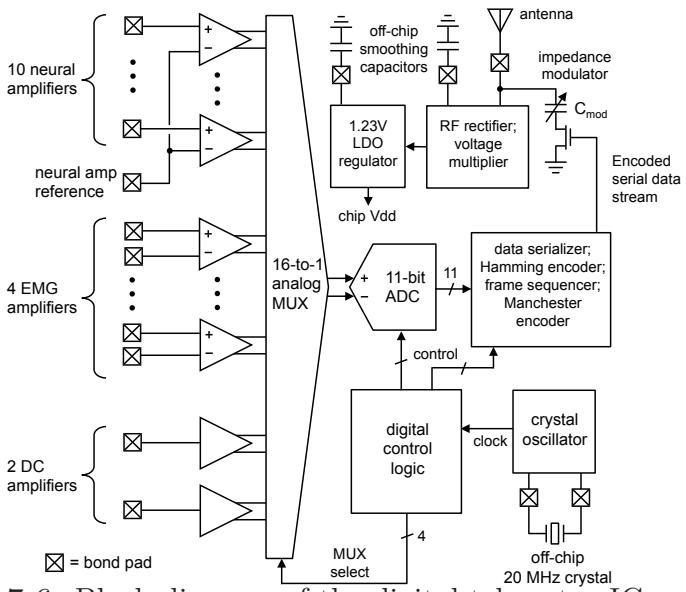

FIGURE 7.6: Block diagram of the digital telemetry IC [©2012 IEEE]

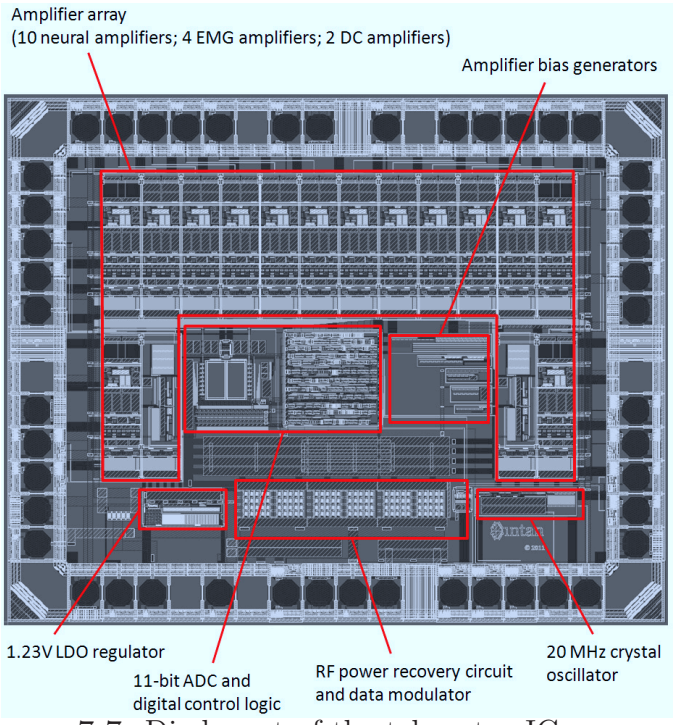

FIGURE 7.7: Die layout of the telemetry IC [©2012 IEEE]

described in Section 7.6 includes an optional antenna impedance matching network in addition to these three components.

7.4.1 Neural and EMG biopotential amplifiers

The neural and EMG amplifiers have fully differential architectures using low-noise, low-power CMOS design techniques previously described in detail [2,103]. The use of differential signaling throughout adds immunity to common-mode noise and power supply noise.

The neural amplifiers each have a bandwidth of 250 Hz to 10 kHz with a gain of 500 V/V and a maximum input range of ±2.4 mV. The measured input-referred noise of each neural amplifier is 5.7 μVrms. The ADC's least significant bit (LSB) is 2.3 μV, referred to the input. The input-referred noise of the amplifier thus occupies 2-3 LSBs. Simulation indicates that each neural amp consumes approximately 16 μW of power from V_{reg}.

The EMG amplifiers each have a simulated bandwidth of 5 Hz to 700 Hz with a gain of 50 V/V and a full-scale input range of ±24 mV. The measured input-referred noise of each EMG amplifier is 43 μVrms. The ADC LSB step size is 23 μV, referred to the input, so the input-referred noise occupies 1-2 LSBs. Simulation indicates that each EMG amp consumes 0.25 μW of DC power from V_{reg}.

The DC amplifiers have a 0 to 4.9 V input range (using an on-chip voltage divider). The ADC LSB step size is 2.4 mV, referred to the input. One of the DC amplifiers is permanently connected to the output of the RF power recovery circuit, and thus monitors the unregulated voltage supply of the chip. This is a useful feature because the telemetry IC can thus indicate when the available RF power is sufficient for proper operation of the chip. The other DC amplifier is available for use with an optional off-chip sensor.

7.4.2 Input multiplexing, data framing, and error correction

A high-speed analog multiplexer connects one selected amplifier at a time to an 11-bit successive approximation ADC with a differential input and bandgap voltage

reference. The ADC's clock is derived from the 20 MHz quartz crystal. It digitizes the 10 neural inputs at 26.1 kSps, along with 4 additional EMG inputs at 1.63 kSps. This is accomplished by digital control logic that re-visits the neural inputs more frequently than the EMG and auxiliary inputs, as indicated in the data frame layout shown in Fig. 7.8.

Each of the 11-bit ADC samples are encoded into a 16-bit word using an extended (11,16) Hamming code, which provides SECDED (Single Error Correction; Double Error Detection) capability, providing robust data transmission in noisy environments.

Each data frame consists of 192 16-bit words, sent at a rate of 1627.6 frames per second, for an aggregate return link data rate of 5.0 Mbps. The 192 word frame layout is organized into 16 rows and 12 columns. The last 10 columns in each row always contain samples from each of the 10 neural input channels. Neural data is therefore sampled and telemetered more frequently than the EMG and auxiliary data.

The data frame is delimited by three 16-bit frame markers. Frame marker 1 (FM1) is a unique word indicating the start of each complete frame, and is thus present 1627.6 times per second. Frame marker 3 (FM3) is another unique word that always occupies the second position in each of the 16 rows in the frame, immediately preceding the 10 neural samples. Frame markers 1 and 2 occupy alternate rows. Rows not beginning with FM1 or FM2 begin with samples of each of the 4 EMG inputs, the 2 Auxiliary inputs, and two special words. Word CID is a 16-bit word containing the state of two digital input pins, so up to four telemetry devices can be uniquely identified with hardware pull-ups. Word CNT is a 16-bit frame counter permitting missing frames to be identified in the data stream, in the event of bit errors that result in the loss of frame sync.

FM1	FM3	N1	N2	N3	N4	N5	N6	N7	N8	N9	N10
E1	FM3	N1	N2	N3	N4	N5	N6	N7	N8	N9	N10
FM1	FM3	N1	N2	N3	N4	N5	N6	N7	N8	N9	N10
E2	FM3	N1	N2	N3	N4	N5	N6	N7	N8	N9	N10
FM2	FM3	N1	N2	N3	N4	N5	N6	N7	N8	N9	N10
E3	FM3	N1	N2	N3	N4	N5	N6	N7	N8	N9	N10
FM2	FM3	N1	N2	N3	N4	N5	N6	N7	N8	N9	N10
E4	FM3	N1	N2	N3	N4	N5	N6	N7	N8	N9	N10
FM2	FM3	N1	N2	N3	N4	N5	N6	N7	N8	N9	N10
A1	FM3	N1	N2	N3	N4	N5	N6	N7	N8	N9	N10
FM2	FM3	N1	N2	N3	N4	N5	N6	N7	N8	N9	N10
A2	FM3	N1	N2	N3	N4	N5	N6	N7	N8	N9	N10
FM2	FM3	N1	N2	N3	N4	N5	N6	N7	N8	N9	N10
CID	FM3	N1	N2	N3	N4	N5	N6	N7	N8	N9	N10
FM2	FM3	N1	N2	N3	N4	N5	N6	N7	N8	N9	N10
CNT	FM3	N1	N2	N3	N4	N5	N6	N7	N8	N9	N10

Word ID	Payload
FM1 - FM3	Frame Markers
N1 – N10	Neural data
E1 – E4	EMG data
A1 – A2	Analog inputs
CID	Chip ID word
CNT	Frame Counter

FIGURE 7.8: Frame layout for the telemetry IC's return link data [©2012 IEEE]

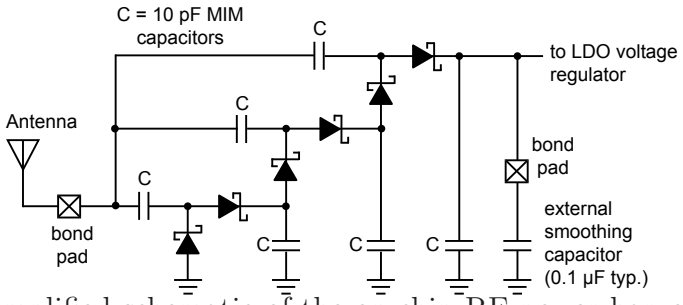

FIGURE 7.9: Simplified schematic of the on-chip RF power harvester [©2012 IEEE]

7.4.3 RF power harvester and voltage regulator

The incident RF signal from the reader transmitter must be converted to DC to wirelessly power the telemetry IC. This is accomplished by an on-chip RF power harvester using a 4-stage Schottky diode based voltage multiplier as shown in Fig. 7.9. The measured input impedance of the packaged chip (chip + bondwires + pads) is $11.50 + j3.80\ \Omega$ at 915 MHz. The output voltage V_{unreg} from the power harvester varies dramatically with the input RF power as shown in Fig. 7.20. V_{unreg} thus varies with distance from the reader transmitter to the telemetry IC. A well regulated DC voltage V_{reg} must therefore be developed to deliver the required 1.23 V to the chip. V_{unreg} feeds an on-chip bandgap-reference 1.23 V low dropout (LDO) voltage regulator detailed in Fig. 7.10. The dropout voltage is 80 mV, so a minimum of 1.31 V from the RF power recovery circuit is required to power the chip.

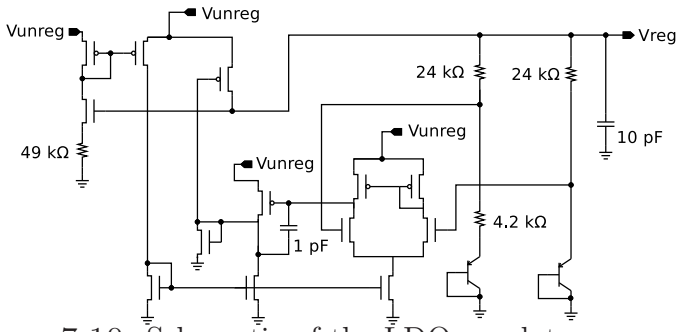

FIGURE 7.10: Schematic of the LDO regulator [©2012 IEEE]

7.4.4 Backscatter modulator

Shown in Fig. 7.11, the telemetry IC implements BPSK backscatter by introducing an additional shunt capacitance in parallel with the harvester's input impedance. This is accomplished with a capacitive PSK modulator that is digitally configurable via pin strapping to values between 62.5 fF and 500 fF. This allows for a modulation depth variable between 0.22% and 1.74% relative to the chip's conjugate match impedance as shown in Table 7.3. By keeping the modulation depth relatively shallow, the majority of the incident RF power is available for harvesting to DC to power the chip. PSK backscatter modulation, as implemented in this chip, has been shown to have a significant power efficiency advantage compared with ASK (load modulation) [99].

The modulator circuit is realized using a weighted capacitor array that is configured using two input pins to select a particular modulating capacitance from the array. A single FET is then used to connect or disconnect the appropriate MIM capacitor to ground. Fig. 7.12 shows the BPSK backscatter spectrum at the receiver input with the telemetry IC connected to a test dipole 1 m away from the perch antenna. The two BPSK sidebands containing the chip's backscattered data are visible, along with a strong self-jammer (-10.8 dBm) caused by unwanted transmitter-receiver coupling as well as reflective objects in the environment.

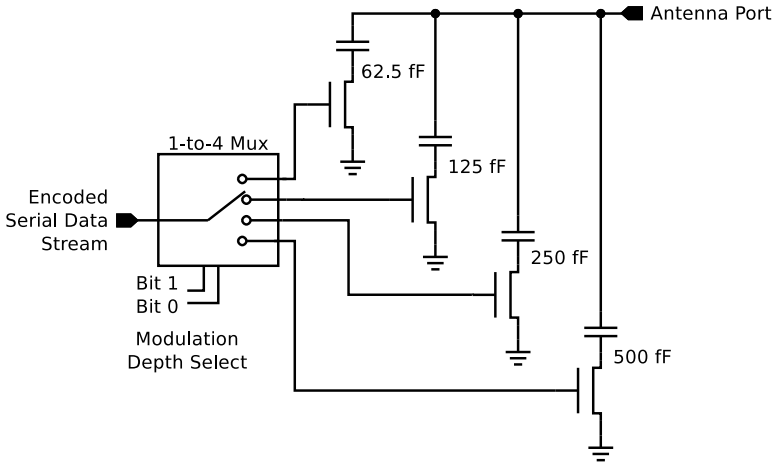

FIGURE 7.11: Schematic of the digitally controlled variable-depth BPSK modulator [©2012 IEEE]

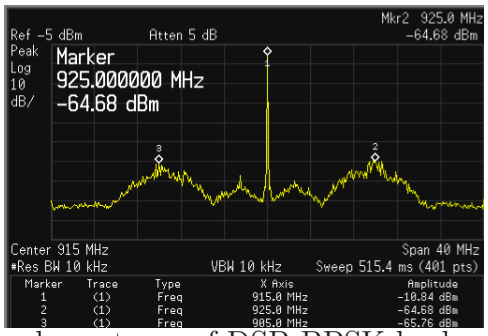

FIGURE 7.12: Measured spectrum of DSB BPSK backscatter data [©2012 IEEE]

Table 7.3: Variable-depth BPSK Backscatter Modulation [©2012 IEEE]

Chip State	$Z_{\text{Chip+Package}}$ at 915 MHz	$\Delta\Gamma$	Modulation Depth (%)
Unmodulated	$11.50 + j3.80$	0	0
62.5 fF	$11.53 + j3.76$	$0.0007 - j0.0021$	0.22%
125 fF	$11.56 + j3.72$	$0.0013 - j0.0041$	0.43%
250 fF	$11.62 + j3.62$	$0.0025 - j0.0083$	0.86%
500 fF	$11.74 + j3.54$	$0.0051 - j0.0167$	1.74%

7.5 Reader

7.5.1 Reader transmitter (BSTx)

Because of the relatively high power consumption of the wireless neural telemetry system (1.23 mW) compared to typical UHF RFID tags ($\approx 10\ \mu$W), a much higher effective isotropic radiated power (EIRP) is required to achieve similar operating distances. The reader transmitter (BSTx) can deliver an RF output power of up to +36 dBm and is typically used with antenna gain of 9 dBi, yielding an EIRP of up to +45 dBm. These power levels exceed the FCC Part 15.247 limit of +36 dBm EIRP, but are permitted in this band under the Part 18 rules for industrial, scientific, and medical (ISM) systems.

A block diagram of the BSTx is shown in Fig. 7.13, and a photo is shown in Fig. 7.14. A Texas Instruments MSP430F2011 microcontroller is used to control the synthesized local oscillator in the transmitter. The microcontroller programs the synthesizer (Mini-Circuits KSN-960A) to generate a 915 MHz carrier, which is amplified by a power amplifier module (NXP BGY-915) specified for continuous duty at +36 dBm output. All conducted harmonic and out-of-band spurious outputs are suppressed in excess of 70 dB. The BSTx microcontroller can also amplitude modulate the power amplifier to send addressing commands from the BSTx to future generations of the neural telemetry system.

Due to the full-duplex on-channel nature of modulated backscatter communication, receiver performance is typically limited by strong-signal handling (linearity) as well as local oscillator phase noise. Measured LO phase noise (Fig. 7.15) is better than -129 dBc/Hz in the critical 1 MHz – 10 MHz carrier offset regime where the BPSK encoded backscatter is present. Transmitter-receiver isolation is maximized with a bistatic Tx-Rx antenna pair. Through careful placement of the Tx and Rx antennas, an isolation of approximately 45 dB is achieved.

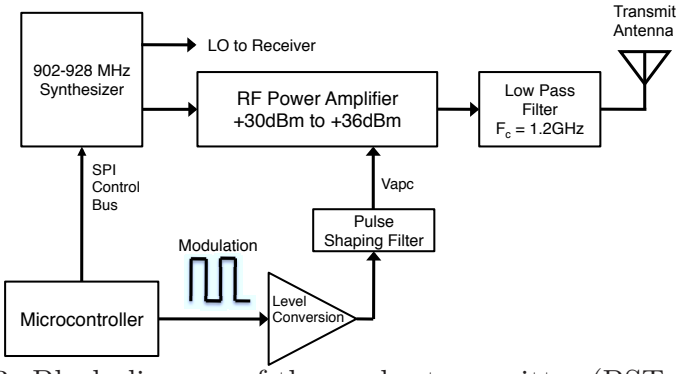

FIGURE 7.13: Block diagram of the reader transmitter (BSTx) [©2012 IEEE]

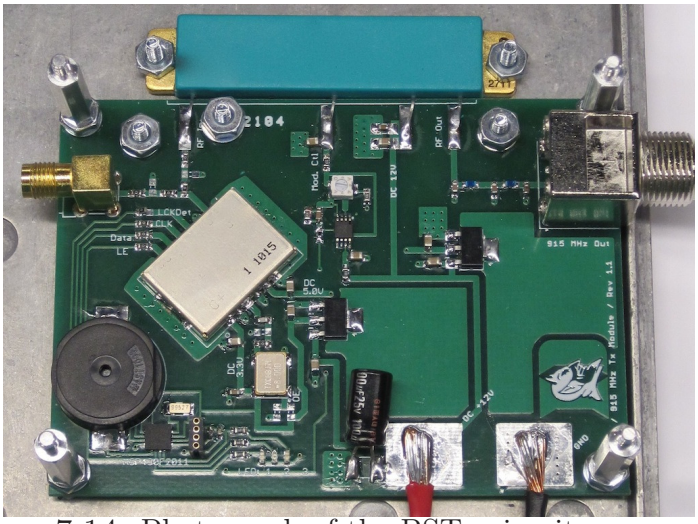

FIGURE 7.14: Photograph of the BSTx circuitry [©2012 IEEE]

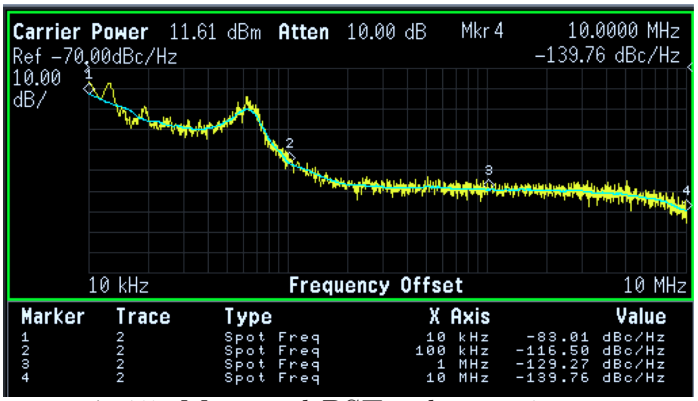

FIGURE 7.15: Measured BSTx phase noise [©2012 IEEE]

7.5.2 Reader receiver (BSRx)

A block diagram of the BSRx is shown in Fig. 7.16, and a photograph of the receiver circuitry is shown in Fig. 7.17. It is a direct conversion design with a digitized baseband section. Backscatter communication is inherently full duplex, as the transmitted carrier is always present during reception. The receiver's analog front end (AFE) is thus optimized for large signal performance at the expense of noise figure. The receiver's AFE has a measured 1 dB compression point of +14 dBm with a noise figure at analog baseband of 13 dB. The relatively high noise figure does not limit receiver performance for link distances of up to 5 m. Within the baseband signal bandwidth the input-referred noise power is approximately -88 dBm, yielding a sensitivity of better than -70 dBm at a BER of 10^{-5} at a data rate of 5 Mbps. In practice, sensitivity is somewhat reduced by partial phase noise correlation in the transmitter-receiver system. At the telemetry IC's power-up threshold of +7.76 dBm at the chip's input terminals, and assuming a backscatter ratio of -15 dB, the expected signal power at the BSRx is -47 dBm yielding a receive-system implementation margin of $\approx$ 23 dB.

Baseband signals are filtered by a matched pair of bandpass filters to reject out-of-band noise, decimated, then rotated to the in-phase axis to bit-slice the BPSK-encoded signal. A digital phase locked loop and symbol correlators extract clock and data prior to transfer to the reader's PC for Hamming decoding with a LUT-based approach. A USB 2.0 port interfaces the received data to a PC for subsequent processing. Several time-synchronous digital inputs are also carried along with the received data to achieve synchronization between the telemetry data stream and a video motion capture system.

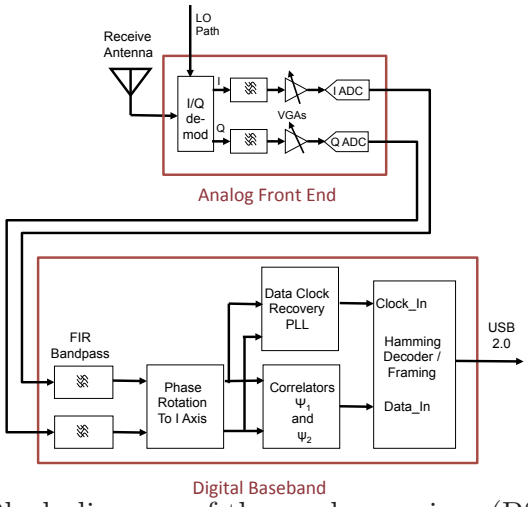

FIGURE 7.16: Block diagram of the reader receiver (BSRx) [©2012 IEEE]

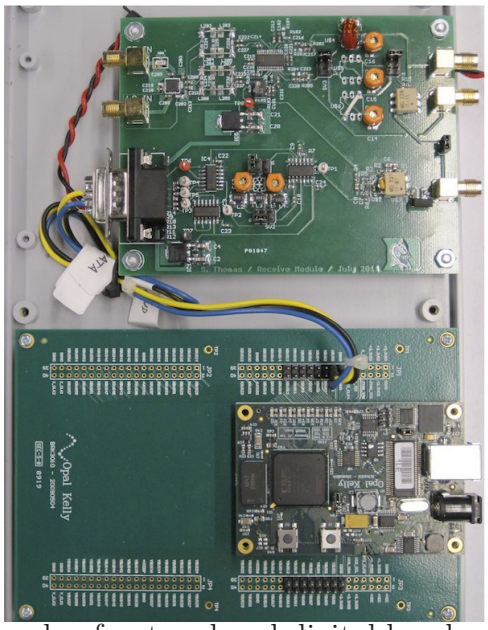

FIGURE 7.17: BSRx analog front end and digital baseband sections [©2012 IEEE]

7.6 Packaging

To minimize the size and weight of the telemetry device, chip-on-flex packaging is employed. As shown in Fig. 7.18, the 2.36 mm x 1.88 mm x 250 μm die is wire bonded directly to a 4.6 mm x 6.8 mm flex substrate. The tiny 0402 surface mount components are bonded to the substrate with conductive epoxy. A miniature 20 MHz

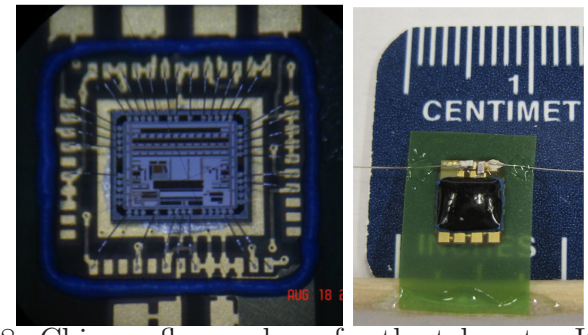

FIGURE 7.18: Chip-on-flex package for the telemetry IC [©2012 IEEE]

quartz crystal and the two required bypass capacitors are placed on the back side of the flex package, behind the die. Pads on the front side accommodate an L- or pi- configuration impedance matching network to match the chip and bondwire impedance to the antenna's impedance, or to 50 Ω for testing. The total package mass, including matching components, is 38 mg.

7.7 Measurement results

The performance of the telemetry IC and reader was verified in both a 50 Ω connectorized (wired) setup, as well as an over-the-air (OTA) wireless experimental setup. In the wired setup, the RF output from an Agilent N9310A signal generator is connected through a 20dB bi-directional coupler (Mini-Circuits ZABDC20) to the antenna port of a telemetry module matched to 50 Ω impedance. The reflected signal from the telemetry IC via the directional coupler's reverse-coupled port is fed to the reader receiver (BSRx). The returned data is captured by a PC connected to the BSRx via USB 2.0.

Wireless operation was characterized using the perch box antennas (Laird model 9028PCR RHCP patches) for the BSTx and BSRx, and the reduced-size dipole antenna on the telemetry IC. The 915 MHz transmit signal was adjusted to compensate for cable losses and produce +36 dBm at the transmit antenna.

Table 7.4: Telemetry IC power breakdown (meas. vs. sim.)

Neural amplifiers	10 x 16 μA	160 μA
EMG amplifiers	4 x 0.25 μA	1 μA
DC amplifiers	2 x 45 μA	90 μA
Analog mux		139 μA
Amplifier / mux bias generators		80 μA
11-bit ADC and digital control logic		320 μA
LDO voltage regulator		60 μA
Crystal oscillator		70 μA
Backscatter modulator		15 μA
Simulated Total IC supply current		935 μA
Measured Total IC supply current		940 μA
Minimum unregulated supply voltage		1.31 V
Simulated Total IC power consumption		1.22 mW
Measured Total IC power consumption		1.23 mW

7.7.1 DC power breakdown

The DC power consumption of the chip was measured in the wired setup by temporarily powering the chip's V_{unreg} node from a bench supply. The measured total DC power consumption is 1.23 mW, which is very close to the simulated value of 1.22 mW. Based on simulation results, we were able to break down the total power by subsystem as shown in Table 7.4 and Fig. 7.19. The majority of system power (84%) is dedicated to bio-signal acquisition (biopotential amps, ADC, and control logic) while the backscatter modulator used for the data uplink accounts for only 2% of total system power.

7.7.2 Over-the-air wireless power (forward link)

The operation of the RF power harvester and LDO regulator were characterized first in the RF powered, wired setup. The chip was matched to 50Ω with the modulating capacitance set to 500fF. As shown in Fig. 7.20, the chip enters regulation at +7.76dBm (6mW) RF input power, with V_{unreg}=1.31V and V_{reg}=1.23V. At the

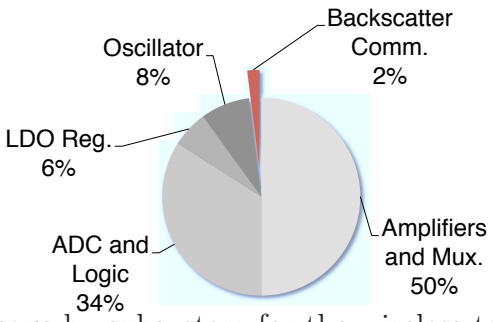

FIGURE 7.19: Power usage by subsystem for the wireless telemetry IC. [©2012 IEEE]

power-up threshold, given the measured DC supply current consumed at V_{unreg} of 940μA, the chip's DC power consumption is 1.23mW and the RF-DC conversion efficiency is $\eta \approx 20.6\%$ including external matching network and substrate losses. Because the chip is in full operation (acquiring and modulating data) this measured power consumption and efficiency also takes into account the effect of the backscatter modulation on the available power to the chip as described in Sec. 7.4.4.

A characterization of over-the-air forward link performance is shown in Fig. 7.21 and Fig. 7.22. To confirm the link budget shown in Table 7.2, the chip's dipole antenna was oriented parallel to the X and Y axes, and V_{unreg} and V_{reg} were measured as a function of Z axis distance (height) as shown in Fig. 7.21. The chip was always in regulation at a distance of up to 1.4 m in either polarization. The Y polarization achieved a longer operating distance of about 1.7 m which is in very close agreement with the 1.9 m maximum distance predicted in Table 7.2. The difference between the X and Y polarizations is likely due to imperfect circular polarization of the transmitting antenna. A slight elliptical polarization is suggested by the manufacturer's specified axial ratio of 1 dB [104].

The packaged chip was attached to the reduced-size dipole antenna and positioned at varying distances $Z = \{0.9, 1.2, 1.4\}$m and rotation angles (0-360 degrees in the $X - Y$ plane) with respect to the transmitting antenna. Figure 7.22 shows the unregulated (V_{unreg}) and regulated (V_{reg}) voltages measured with the chip in full

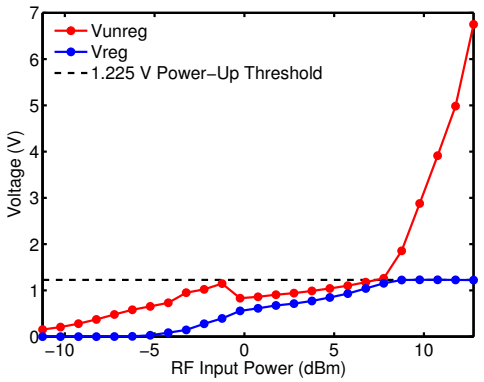

FIGURE 7.20: Measured unregulated (V_{unreg}) and regulated (V_{reg}) supply voltages as a function of RF input power. The chip achieves regulation at an input power of +7.76dBm. [©2012 IEEE]

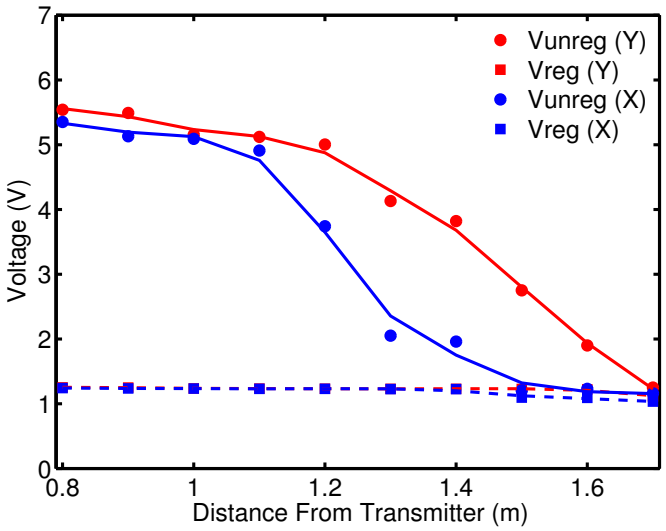

FIGURE 7.21: Measured unregulated (V_{unreg}) and regulated (V_{reg}) supply voltages as a function of distance from the transmitter. [©2012 IEEE]

operation. The chip was found to maintain regulation throughout this measurement, which spans the range of Z distances (heights) of interest in the dragonfly prey capture experiment.

7.7.3 Telemetry uplink (return link)

To verify the operation of the BPSK backscatter telemetry uplink, an Agilent N9320A spectrum analyzer was connected to the receive antenna port, with the telemetry IC

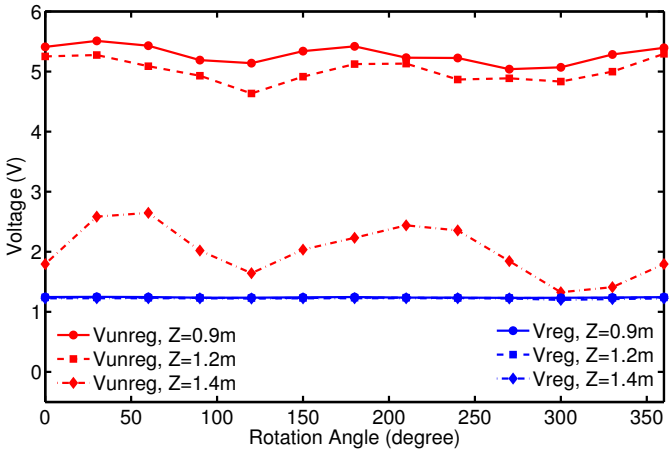

FIGURE 7.22: Measured unregulated (V_{unreg}) and regulated (V_{reg}) supply voltages as the tag is rotated in the X-Y plane at varying Z distance (height) above a +36 dBm, 915 MHz source. [©2012 IEEE]

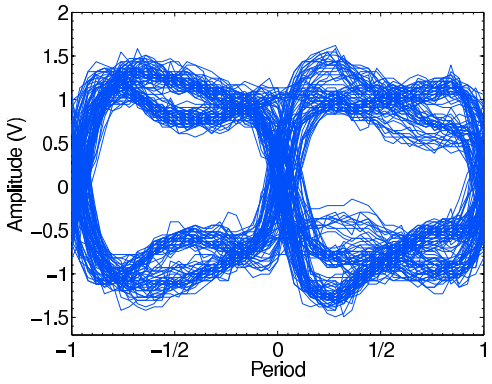

FIGURE 7.23: Measured eye diagram at 5.0 Mbps with the IC 1 m from the receive antenna [©2012 IEEE]

placed at a range of 1 m. The spectrum of the received BPSK backscatter spectrum is shown in Fig. 7.12. The BSRx was then connected to the receive antenna and Agilent DSO8104A oscilloscope was connected to the analog baseband outputs of the receiver's I/Q demodulator. An eye diagram was captured as shown in Fig. 7.23. The measured BER at 5 Mbps was less than 5.0×10^{-5} before error correction in the BSRx.

7.7.4 Biopotential amplifier, MUX, and ADC characterization

The amplifiers, mux, and ADCs were tested together as an integrated acquisition channel, first using the wired measurement setup. All channels were found to perform nominally. Figure 7.24 shows the measured response of a typical channel, including neural or EMG amplifier, the mux, and the ADC, with sinusoidal inputs. These responses were captured from the wired test setup using an Agilent function/arbitrary waveform generator and a high impedance attenuator. The neural channel response was characterized with a 400 Hz, 50 μVpk sinusoidal test signal, and the EMG channel response was characterized with a 50 Hz, 5 mVpk sinusoidal test signal.

A spectrogram of neural channels 1 and 2, captured simultaneously using the wired setup, is presented in Fig. 7.25(a). In this measurement, 400Hz and 10kHz, 160μVpp test signals were applied to channel 1 while channel 2 was grounded. The crosstalk between channels is summarized in Fig. 7.25(b). The worst case crosstalk observed on Channel 2 was at least 53dB below the signal level applied to Channel 1. The observed $2f_0$ and $3f_0$ harmonics are 46dB and 50dB down respectively.

7.7.5 Over-the-air characterization using pre-recorded neural activity

An end-to-end, fully wireless characterization has been performed. Pre-recorded extracellular neural activity from a dragonfly target-selective descending interneuron (TSDN) [85,98] was used as a test signal. The TSDN activity was sampled at 80kHz using a commercial acquisition rack. This data was then loaded into an Agilent arbitrary waveform generator and played back via a high impedance attenuator into the telemetry IC to serve as repeatable test stimulus during over-the-air testing.

The telemetry IC was set up to run wirelessly, with RF power and data uplink, at 1 m range. A comparison between the signal acquired by the commercial acquisition system and the system presented here is shown in Fig. 7.26. Figure 7.26(a) shows

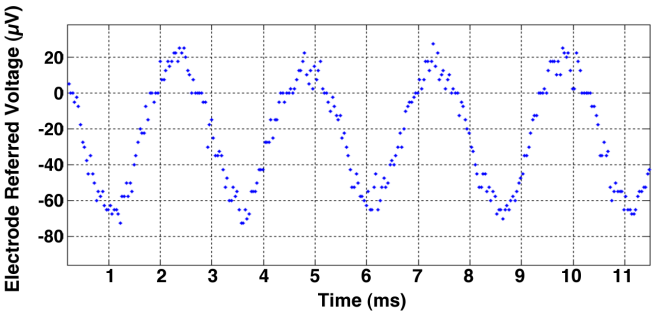

(a) Neural channel, 400 Hz, 50 μVpk input

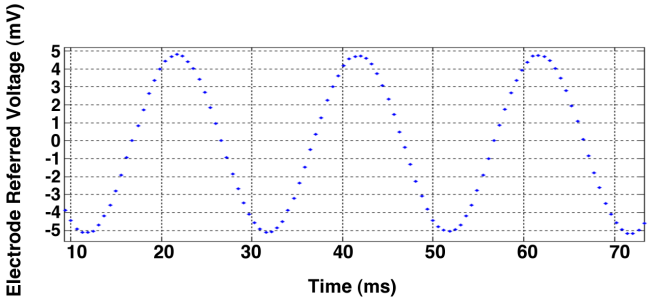

(b) EMG channel, 50 Hz, 5 mVpk input

FIGURE 7.24: Measured, digitized response of the neural and EMG channels with sinusoidal test signals [©2012 IEEE]

a long duration capture. The blue trace (top) is the commercially acquired TSDN signal and the red trace (bottom) is the signal as telemetered completely wirelessly with an RF power and data uplink. Figure 7.26(b) shows a zoomed plot of a representative single spike from the long duration capture. As shown, in both cases the telemetry system faithfully reproduces the source signal.

7.8 Discussion

This chapter presents a digital neural/EMG telemetry system with a measured flight package mass of only 38 mg. It is among the smallest and lightest multi-channel digital neural/EMG telemetry systems yet reported. It has been developed to provide continuous telemetry from a dragonfly in flight.

The system comprises a battery-free, single-chip telemetry IC employing RF power harvesting, along with a companion reader transceiver including an RF trans-

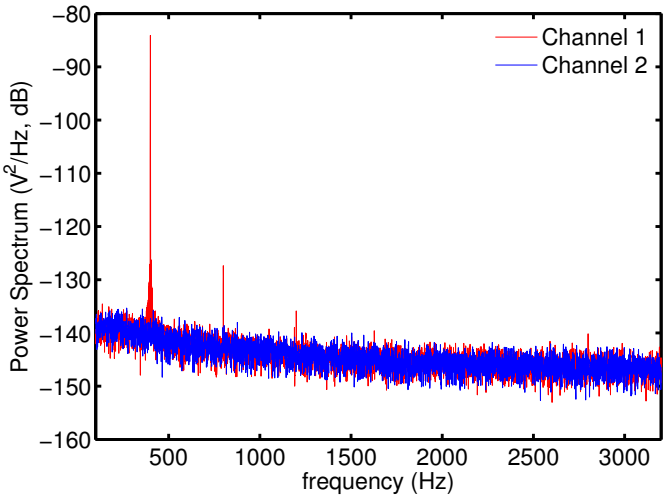

(a)

Source frequency (Ch. 1)	Source Voltage (Ch. 1)	Crosstalk (dB) (Ch. 2)	Crosstalk (%) (Ch. 2)
400 Hz	160 μV	-53.17	0.22
10 kHz	160 μV	-56.58	0.15

(b)

FIGURE 7.25: Example measured spectrum showing channel 1 with a 400 Hz sinusoidal test signal applied simultaneously with channel 2 with grounded input (b) Summary of crosstalk between channels. [©2012 IEEE]

mitter and a digital receiver. The chip digitally telemeters 10 neural and 4 EMG signals. Neural signals are sampled at a rate of 26.1 kSps, and EMG signals are sampled with 11 bit resolution at a rate of 1.63 kSps for a signal bandwidth of 250Hz–10kHz and 5Hz–700Hz, respectively. In addition to an RF power harvester to supply its operating voltage, the chip includes a 5 Mbps data uplink via modulated backscatter in the UHF (902–928 MHz) band. Only three external components are required. Measurements indicate that the chip and reader are fully functional as designed. Table 7.5 summarizes the achieved system performance.

Ongoing work related to this system includes the optimization of the transmitter and receiver antennas in the dragonfly perch to maximize the reliability of power delivery in the region of interest. The maximum operating range is currently limited by

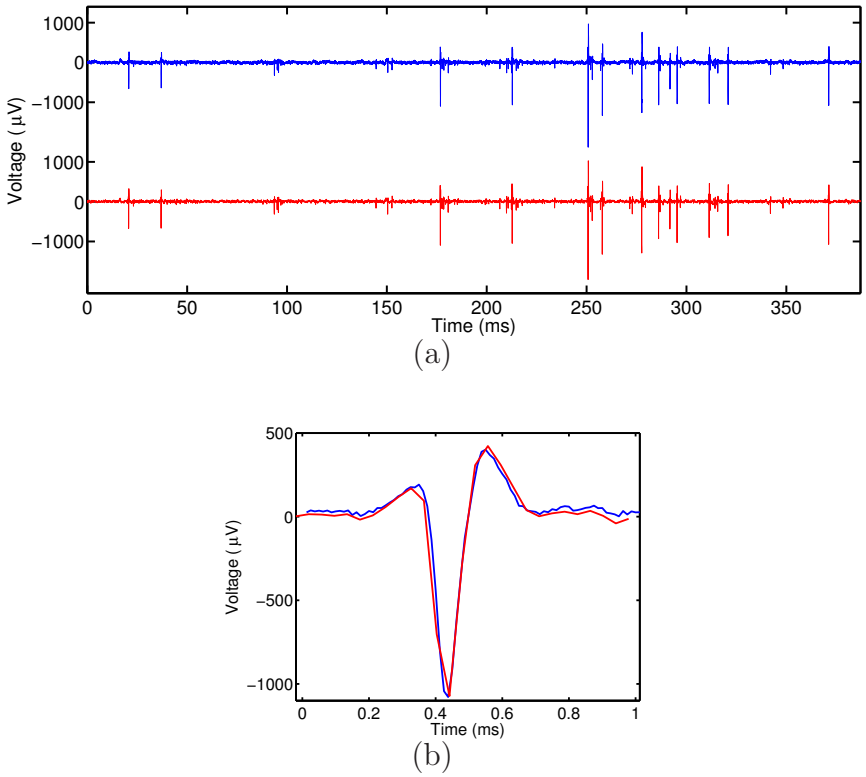

FIGURE 7.26: Wireless acquisition of pre-recorded dragonfly TSDN activity showing (a) long duration capture and (b) expanded view of single spike. The blue trace (top) is the signal recorded by a commercial acquisition rack. The red trace (bottom) is the signal as telemetered from the wirelessly-powered, wirelessly-uplinked system. [©2012 IEEE]

the non-ideal elliptical polarization of the commercial transmit antenna. Additional antenna and system design in the form of a diversity transmitter and receiver is being developed to overcome polarization mismatch to the dragonfly mounted dipole antenna in certain flight poses. The dragonfly mounted antenna itself represents a significant design challenge as it is severely size and weight constrained and must not interfere mechanically with the movement of the wings.

Additional work is also ongoing in the development of microelectrodes optimized for recording from the dragonfly's nerve cord. Of particular interest are electrodes optimized for simultaneously probing as many as possible of the 16 target-selective

Table 7.5: Summary of System Performance

Total Mass	38 mg
Operating Frequency	902 – 928 MHz
Telemetry Modulation	digital BPSK backscatter 5 Mbps
RF Power Consumption	+7.76 dBm (6 mW)
DC Power Consumption	1.31V @ 940 μA = 1.23 mW
RF-DC Power Conversion Efficiency	20.6 %
Operating Range	$\approx$ 1.5m (1.91m, est.) given +36 dBm transmitter and 9dBic antenna
Acquisition Channels	10 neural 4 EMG 2 auxiliary DC inputs
Acquisition Bandwidth	250Hz – 10 kHz (neural) 5Hz – 700Hz (EMG)
Maximum input range	$\pm$ 2.4 mV (neural) $\pm$ 24 mV (EMG)
Input-referred noise	5.7μVrms (neural) 43μVrms (EMG)
Crosstalk between channels	$<$ -53 dB

descending neurons that appear to control interception and steering during prey capture.

7.9 Wireless audio over the backscatter link

The high data rates of the tag telemetry IC previously discussed usher in a new class of backscatter tags. Leveraging the previous biosignal recording IC design, this section[2] presents the first rich-media class of UHF RFID tags.

[2] This portion of the chapter is a derivative of previously published work, ©2012 IEEE. Reprinted, with permission, from Thomas et al., "Rich-Media Tags: Battery-Free Wireless Multichannel Digital Audio and Image Transmission with UHF RFID Techniques," in 2013 IEEE International Conference on RFID, May 2013.

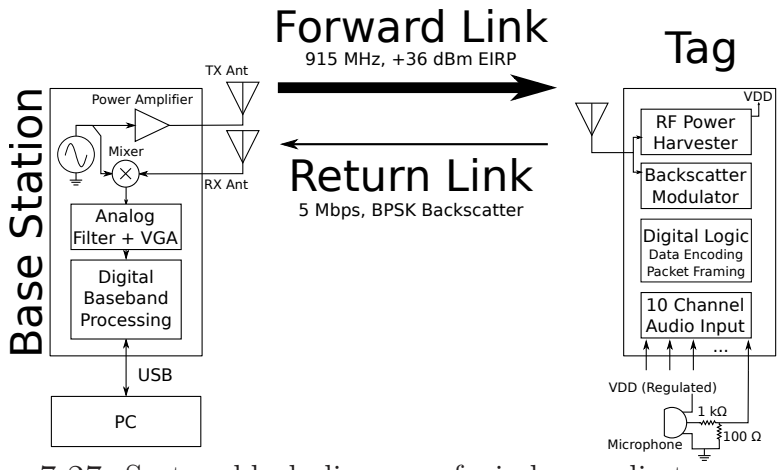

FIGURE 7.27: System block diagram of wireless audio tag [©2013 IEEE]

7.10 System description

A block diagram of the system is shown in Fig. 7.27. The digital audio streaming system consists of two parts: the reader transceiver and the audio recording tag pictured in Fig. 7.28. The reader is responsible for RF carrier generation and transmission to the tag as well as data reception, demodulation and decoding. At the reader, a frequency synthesizer generates a frequency agile UHF (868–950 MHz) carrier that is passed through a power amplifier to yield a total output of +36 dBm EIRP, including transmit antenna gain. The reader is usually operated in a bistatic mode, with the signal captured by the receiving antenna of the reader being mixed with a replica of the transmitted carrier and passed through a set of analog bandpass filters and variable gain amplifier (VGA) blocks to shape the signal before being sent to an FPGA-based digital baseband processing unit. Analog baseband signals are sampled at 100 MS/s using a 16-bit analog to digital converter (ADC) and digitally filtered before being rotated and sliced for bit decisions, clock recovery and data decoding. The decoded data is sent to a PC over a USB connection for display and data capture.

The fully integrated audio includes a 4-stage Schottky-diode based RF power

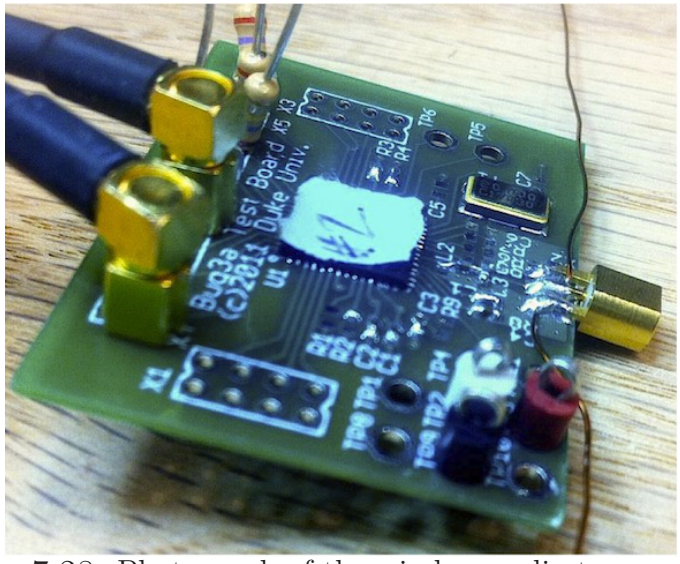

FIGURE 7.28: Photograph of the wireless audio tag [©2013 IEEE]

harvester enabling fully-passive, battery-free operation, a 1.23 V low dropout (LDO) voltage regulator, a digitally-configurable, variable impedance backscatter binary phase shift keying (BPSK) modulator, digital logic for data encoding and packet framing, and 16 total amplifier channels including 10 audio bandwidth input channels each connected to an 11-bit ADC by a high-speed MUX. The IC itself requires a minimum of 3 off-chip components for operation – a miniature 20 MHz quartz crystal oscillator and two 0402 SMT bypass capacitors for the unregulated and regulated power supplies V_{DD} and $V_{DD-\mathrm{Reg}}$. The printed circuit board also includes an impedance matching network to transform the chip impedance to match the 50 Ω antenna impedance. The populated tag board, excluding an external antenna, measures 38 mm x 28 mm, with generous component spacing, so further reduction in size is straightforward.

The chip, developed at Intan Technologies, incorporates 10 fully differential low-noise, low-power CMOS front end amplifiers used for analog signal capture. The amplifiers have a simulated and measured bandwidth of 200 Hz – 13 kHz as shown in Fig. 7.29. For comparison, the bandwidth of the public switched telephone net-

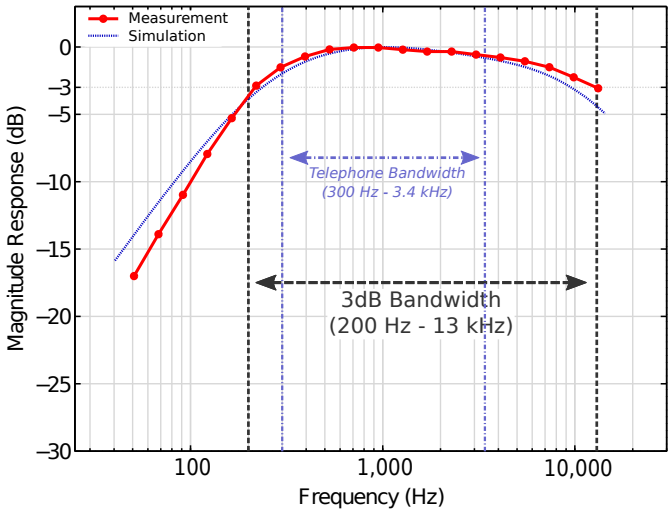

FIGURE 7.29: Measured magnitude response of audio recording tag [©2013 IEEE]

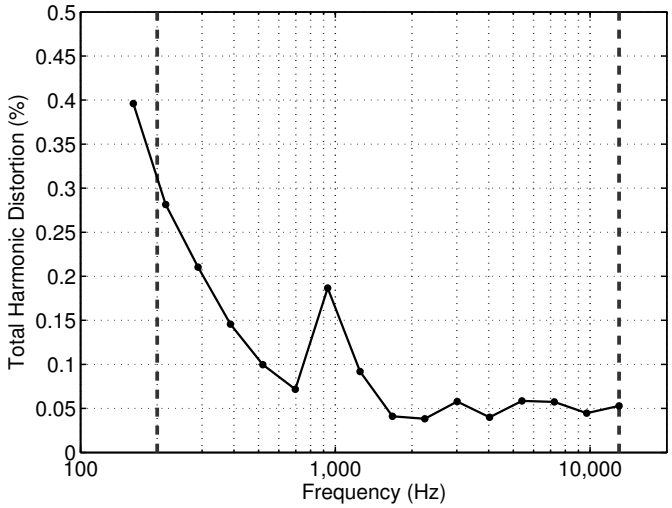

FIGURE 7.30: Measured total harmonic distortion (THD + N) [©2013 IEEE]

work (PSTN) is approximately 300–3400 Hz indicating that the tag has more than sufficient bandwidth available to faithfully reproduce human speech. Each of the 10 audio channels are sampled at 26.1 kHz with 11-bit resolution.

To understand their distortion performance in audio applications, the amplifier channels were characterized by measuring total harmonic distortion plus noise (THD + N) and channel crosstalk. The THD + N measurement was performed by injecting a single tone into the audio chip and recording the received signal. This test was per-

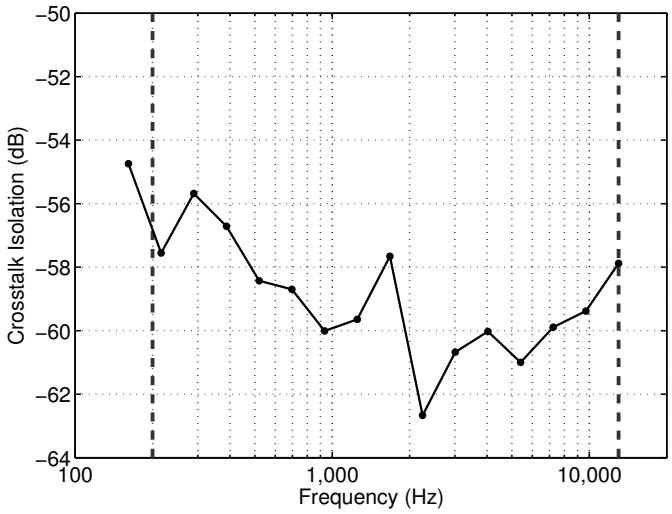

FIGURE 7.31: Measured crosstalk between input amplifier channels [©2013 IEEE]

formed in a cabled setup using a 50 Ω shielded cable and attenuators to approximate the over-the-air channel while maintaining minimum RF noise in the environment. The received data was filtered in post-processing with a digital notch filter (Q = 10) to remove the input tone, leaving only the resulting harmonics and noise for a single amplifier channel. THD was then calculated as the ratio of harmonic plus noise power to original signal power (including the fundamental tone)

$$\text{THD} + N = \frac{\sum \left(S_i^{\text{filt.}}\right)^2}{\sum \left(S_i\right)^2} \tag{7.3}$$

where $S_i^{\text{filt.}}$ is the filtered signal and S_i is the original signal including all harmonics. THD + N is then reported as a percentage. This measurement was taken over the entire signal bandwidth (dc – 13 kHz). Measured THD + N data, as shown in Fig. 7.30, is less than 0.3% over the entire 3 dB channel bandwidth.

Crosstalk between amplifier channels was also measured. Similar to the THD + N measurement, a single tone was injected into the input port of an amplifier channel (channel A) and the ratio of power levels between channel A and a terminated channel (channel B) was measured. The results shown in Fig. 7.31 show that isolation between channels remains better than -55 dB over the entire bandwidth (i.e. less

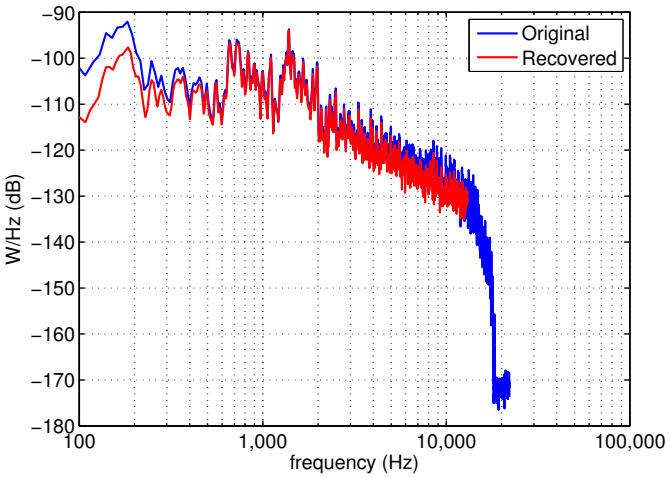

FIGURE 7.32: Measured spectrum comparing original source audio signal and recovered audio signal (cabled setup) [©2013 IEEE]

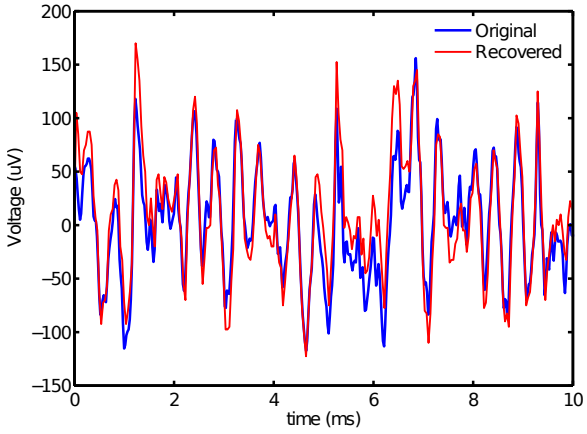

FIGURE 7.33: Measured time-domain waveforms comparing original source audio signal and recovered audio signal (cabled setup) [©2013 IEEE]

than 0.00001% leakage between channels).

7.11 Digital audio characterization

Using a cabled channel setup, a stereo audio file containing music sampled at compact disk (CD) quality (f_s = 44100 Hz, 16-bits) was played back, using a battery powered external device (Apple iPhone) as a signal source. The use of a battery powered audio source allows the testing to be independent of lab ground to avoid ground

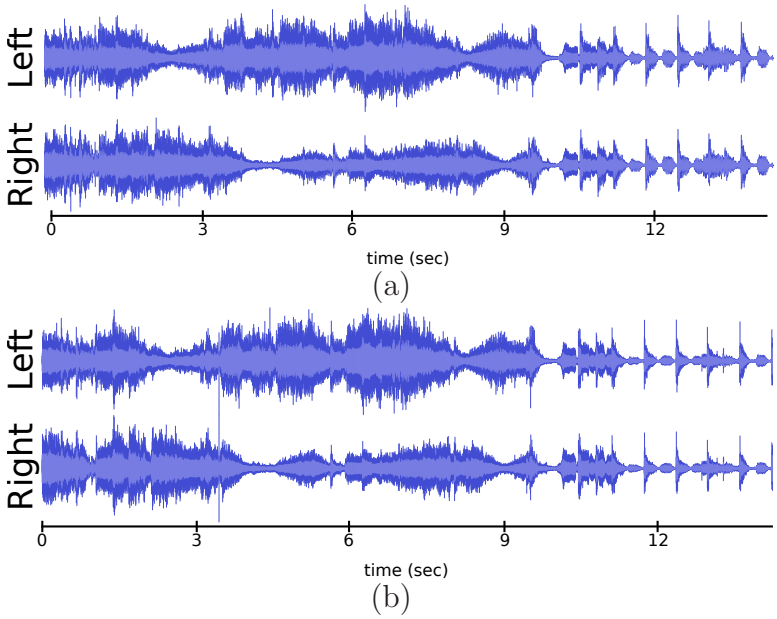

FIGURE 7.34: Measured over-the-air recording comparing original, transmitted waveform (a) and received, recovered waveform (b) [©2013 IEEE]

loops and/or unwanted 60 Hz hum pickup. After passing through the entire tag + RF channel + reader system, the received digital audio signal was then compared to the original recording. Based on an informal sampling of nearby listeners at the time of the experiment, listeners had difficulty differentiating between the original source and the received audio, even given the difference in sample depth and sample rate (16-bits vs. 11-bits, and 44.1 kHz vs. 26.1 kHz).

We then proceeded to perform a more formal engineering evaluation of signal fidelity. In Fig. 7.32 the frequency spectrum of the original, CD-quality recording is compared to the recovered audio transmitted through the audio tag. Though some information is lost below ≈300 Hz and above 13 kHz (the Nyquist frequency of the on-chip ADC sampling rate), the overall shape of the spectrum is maintained. Similarity is also observed in the time-domain comparison, shown in Fig. 7.33. The recovered signal does not track the very highest-frequency features of the original signal, but follows the overall shape of the signal, still allowing for perceptually clear

Table 7.6: Wireless Audio Power Link Budget

Transmitter output power	P_t	+28 dBm
Transmitter antenna gain	G_t	8 dBi
Receiver (tag) antenna gain	G_r	8 dBi
Operating wavelength	λ	33 cm
Received power at tag input terminals	P_r	7.76 dBm
IC power harvester + mismatch efficiency	η	20.6 %
DC power consumed by tag	P_{th}	1.23 mW
Power-up threshold distance	$r\vert_{P_r\,=\,7.76\,\text{dBm}}$	1.703 m

audio reproduction.

After confirmation of functionality of the audio tag using the cabled setup, an over the air experiment was performed. In this experiment, the reader was configured to output +36 dBm EIRP, using a bistatic configuration with 8 dBi linear patch transmit and receive antennas. The audio tag was attached to a similar 8 dBi linear patch antenna and placed 1.4 m away from the reader. A battery powered external device (Apple iPhone) was again used as the audio test source. The left and right stereo channels of the iPhone audio output were connected to two input channels of the tag and a CD-quality, stereo file was played back through the tag and recorded at the reader.

The original, stereo input signal played back into the audio tag is shown in Fig. 7.34 (a) and again compared in the time domain to the received signal, recorded at the reader, shown in Fig. 7.34(b). Features of the music recording align correctly in time and amplitude and the stereo effects are also both visibly and audibly preserved. This over-the-air test demonstrates that it is possible to transfer high-quality, digitized audio recordings using backscatter technology at distances greater than 1 m. Though only two channels were connected to an audio source in this test, all 16 channels (10 available audio channels, 4 lower-bandwidth channels, and 2 general purpose dc channels) were simultaneously telemetered. Multiple channel pairs

were tested with equivalent results; the lack of a 10-port audio test source prevented us from simultaneously testing all 10 channels but we are confident from pairwise testing that all channels are functioning equivalently.

A link budget is provided in Table 7.6 for the audio tag. This table assumes a transmit power of +28 dBm, a transmit antenna with 8 dBi gain, operation at 915 MHz in freespace, and a tag antenna gain of 8 dBi. Based on a measured tag RF power-up threshold of 7.76 dBm, a maximum forward link limited operating distance of 1.703 m is predicted.

Using the calculation of receiver sensitivity presented in [8], for the measured receiver noise figure of 13 dB, input referred noise is -88 dBm. Assuming a 10 dB SNR yielding a bit error rate of approximately 10^{-5} for BPSK and an assumed backscatter ratio of 15 dB, a theoretical maximum operating distance of $\approx$14 m is predicted for the tag operating in semi-passive mode.

7.11.1 Image transfer via modulated backscatter

The over-the-air setup described above was then used to transmit full-color images using slow-scan television modulation (SSTV) through the audio tag. While the 5 Mbps uplink data rate provided by the tag could certainly be used to carry compressed digital video, we opted to leverage the existing audio-bandwidth pipeline for our initial experiments with image transfer via modulated backscatter.

SSTV is commonly employed by amateur radio enthusiasts for image transmission through narrowband radio channels as well as by NASA / NOAA polar orbiting weather satellites utilizing the Automatic Picture Transmission (APT) standard [105, 106]. In general, SSTV operates by converting an image to an analog audio-bandwidth signal by conveying pixel luminance and color information via amplitude modulation (AM), frequency modulation (FM) or a combination of both. There exist many differing protocols for such types of transmission which have different frame

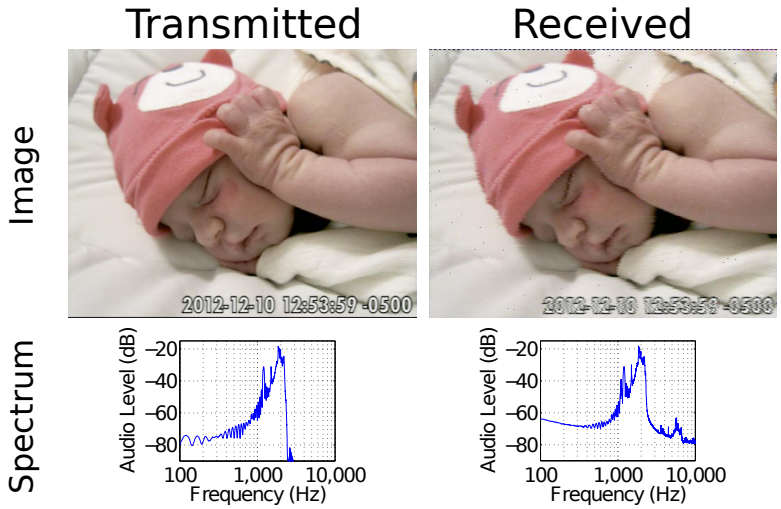

FIGURE 7.35: Comparison of transmitted and received image using an SSTV modulation technique [©2013 IEEE]

rates and image quality parameters [107].

In this experiment, the *PD290* protocol was used to modulate a 640 x 493 pixel input image into an audio file. This protocol allows for transmission of full-color images, but requires long transmission times of 290 seconds per frame (≈5 min / frame). The software "Multi-Scan 2" for Macintosh OSX was used for encoding images into audio as well as decoding audio into images.

The input test image showing an *extremely* cute baby girl, shown in Fig. 7.35 with audio spectrum, was chosen to represent a hypothetical application of a passive child-monitoring system. This encoded audio file was played back into the audio tag using the Apple iPhone as a signal source and wirelessly telemetered 1.4 m to the reader. The received audio was captured and then decoded using the Multi-Scan 2 software. The recovered image and spectrum are shown in Fig. 7.35 on the right compared to the transmitted image on the left. Though some high-frequency noise is present in the received image, the subject is clearly visible and image fidelity is very good.

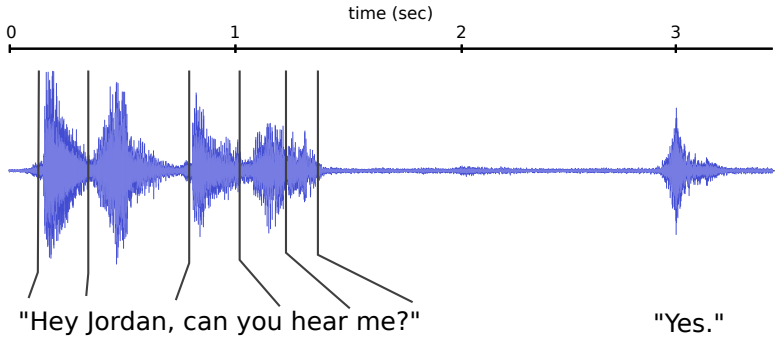

FIGURE 7.36: Fully passive recording of a conversation between participants spaced approximately 3 m [©2013 IEEE]

7.11.2 Battery-Free Digital Wireless Microphone

We then set out to update Theremin's analog Great Seal Bug with modern digital techniques. A very low power microphone (Knowles EM-23046-P16) was integrated with the audio tag circuit. This microphone is specified for operation down to 1.3V VDD, with a current drain of 50μA maximum. Its frequency response is specified to include the region between 100 Hz and 5 kHz which is predominant in human speech.

The regulated 1.3V V_{reg} voltage output from the tag chip's RF voltage harvesting circuit was connected to the microphone. The analog voltage output from the microphone was passed through a voltage divider to reduce signal levels to those appropriate for the amplifier input. The circuit is shown in the block diagram of Fig. 7.27.

The audio tag with its passive microphone was used in combination with a dipole tag antenna with estimated gain of approximately 4 dBi (wire dipole with quarter-wave reflector) and placed 0.72 m away from the reader configured to transmit +36 dBm. Based on a link budget similar to Table 7.6 but scaled for appropriate tag antenna gain, a theoretical maximum operating distance of 1.07 m is expected.

Fig. 7.36 presents a time-domain plot of a conversation recorded using the fully

passive digital microphone.[3] The conversation presented is between two individuals located approximately 0.5 and 3 m respectively away from the microphone. In informal testing, the device recorded clearly audible conversation between participants located over 5 m from the microphone when speaking at normal conversation levels.

7.12 Discussion

These results, showing the first wireless transfer of multichannel high-fidelity digital audio and full-color image over the backscatter link will serve as a first step toward media-rich battery-free devices that take advantage of the high speed, low power nature of modulated backscatter communication links. Future work will focus on interfacing additional sensors on-tag, such as a CMOS camera sensor, in addition to the microphone. The achieved backscatter data link rate of 5 Mbps is more than sufficient for multichannel digital audio and compressed motion video. We expect that ongoing research in power-efficient audio and video codec hardware and software already being developed for smartphone applications will enable increasing media-rich functions even on highly power constrained devices with μW to mW power budgets. This work demonstrates the potential of a new class of media-rich, battery-free devices with unlimited lifetime and great operational flexibility.

7.13 Chapter conclusion

In this chapter experimental results from a low-power, single-chip, high-data rate backscatter system has been presented. Chip functionality has been explored in two applications: wireless biopotential signal recording and rich-media tags transmitting audio and images. The IC requires only +7.76 dBm incident RF power and is

[3] The data shown in Fig. 7.36 was filtered in post-processing to remove room noise before plotting, using the "Noise Removal" tool from the open-source software Audacity. This tool removed high frequency room noise to show the conversation more clearly in the figure, though even with no filtering applied, recorded conversation is easily distinguishable in the raw recordings.

wirelessly communicates at a data rate of 5 Mbps over distances greater than 1 m. The device is able to record and transmit simultaneously up to 16 (10 neural, 4 EMG, 2 general-purpose DC) channels of sampled data. The 10 neural channels are sampled at 26.1 kHz with 11-bit resolution. The remaining 4 EMG and 2 dc amplifier channels are each sampled at 1.63 kHz with 11-bit resolution.

The chip has also been used to demonstrate digital audio and image transmission over the backscatter link. In a series of experiments leveraging the biopotential amplifiers, we have demonstrated multi-channel digital audio streaming, color image transmission, and passive audio recording from a wireless "bug."

8

Towards a single-chip QAM modulator

This chapter provides a description and initial characterization of a single-chip QAM backscatter modulator. This is the first single-chip integrated design intended for use in QAM backscatter. Results presented here will aid in shaping future design of such systems. The chip is designed to be a customizable integrated backscatter communication and sensing device. The 16-state QAM modulator is examined in detail by measuring reflection coefficients over varying frequencies and incident RF power levels. A discussion of the effects of parasitic elements is provided. This includes predicted measurement values with parasitic effects compensated and a plan with new design values to compensate for the effects.

Contributions in this chapter:

- Description of first single-chip backscatter QAM modulator.
- Performance evaluation of single-chip backscatter QAM modulator.
- Plan for future integration.

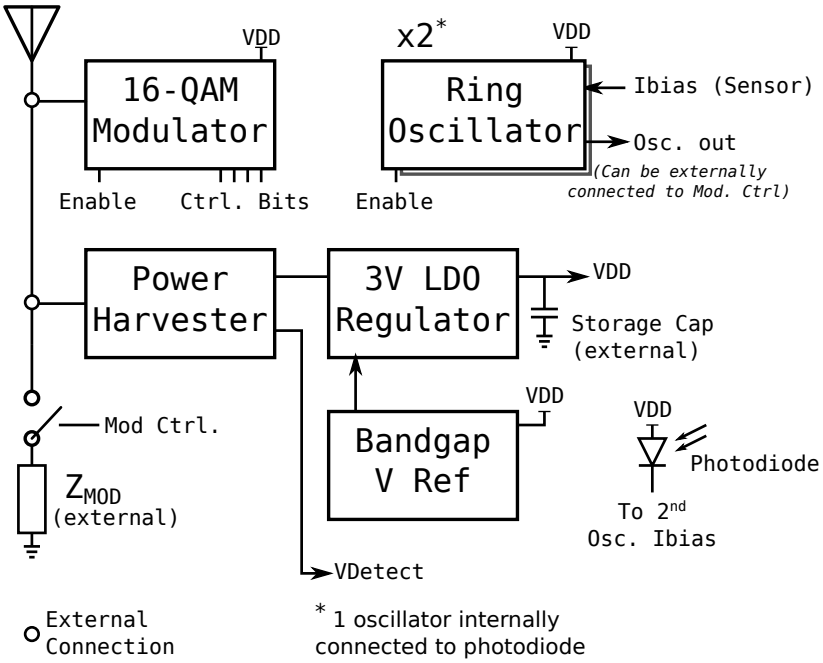

FIGURE 8.1: Block diagram of the custom single-chip RF tag

8.1 Overview of the integrated backscatter sensing chip

A vector modulator was implemented in a single-chip design using a CMOS process. The vector modulator was a single block as part of a larger design. The author thanks Dr. Arnak Aleksanyan (now with Linear Technologies) for his help in chip design and layout. The author designed the 16-QAM backscatter modulator schematic and SPICE models and Dr. Aleksanyan performed chip layout.

The chip was designed using Cadence software and fabricated using the commercial AMI C5N 0.5 μm, 3-metal, 2-poly process available through MOSIS. A highly modular design allows individual system components to function independently. A system block diagram for the chip is shown in Fig. 8.1. Schematic screenshots are shown in Fig. 8.2 with layout and a fabricated die micrograph in Fig. 8.3. The chip can be used to build a fully-passive backscatter sensing circuit that interfaces with a wide variety of analog sensors.

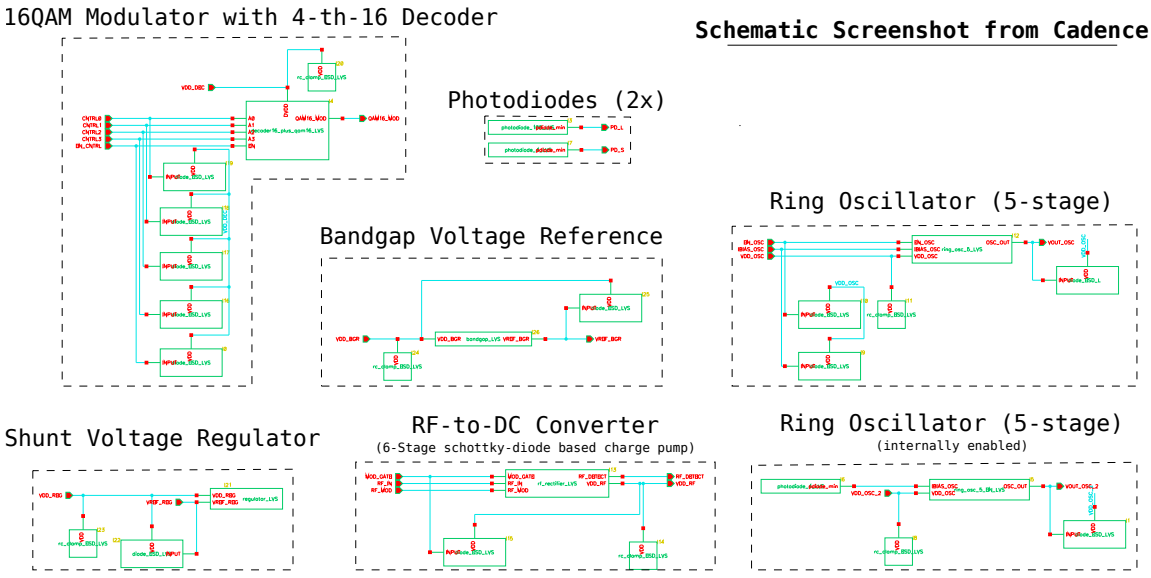

FIGURE 8.2: Schematic of integrated backscatter sensing circuit (from Cadence software)

8.1.1 System components

The chip implements a 16-QAM backscatter modulator, binary backscatter modulator, RF-to-DC converter, shunt voltage regulator with companion bandgap voltage reference, two current-controlled ring oscillators, and two photodiodes. The photodiodes are intended to operate in conjunction with the ring oscillators to form a backscatter light-sensing device. System components have been individually tested and verified for operation. The 16-QAM backscatter modulator will be described below.

Binary backscatter modulator

A binary backscatter modulator is realized using a single FET between the antenna ports (antenna input port and the chip ground). The FET switches in a deliberate mismatch configured with an external impedance. This can be used to generate binary ASK or PSK backscatter with modulation depth determined via impedance selection.

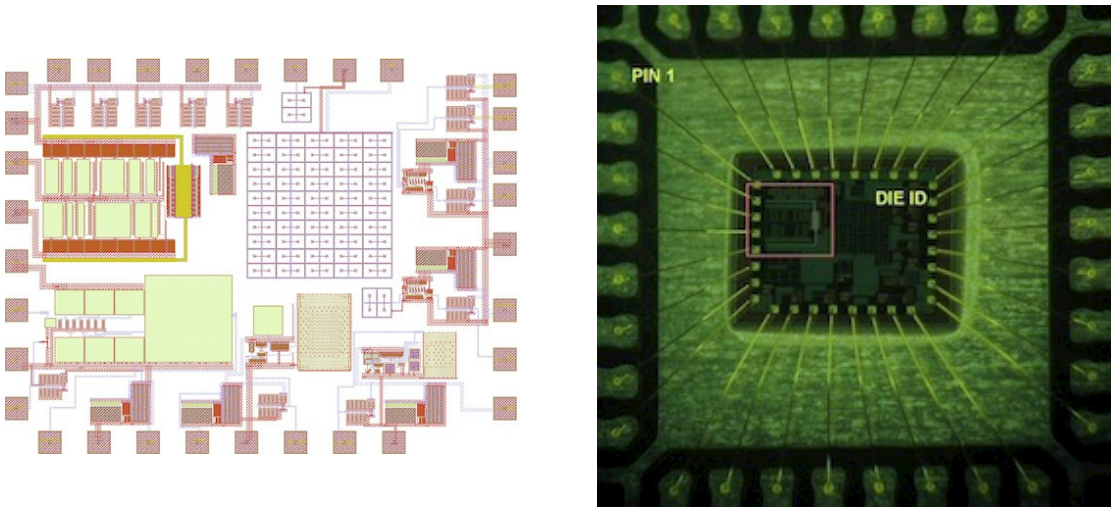

(a) Layout (b) Die Micrograph

FIGURE 8.3: (a) Layout of integrated backscatter sensing circuit (from Orcad software) and (b) fabricated die micrograph with 16-QAM section highlighted

RF-to-DC converter

The chip includes a half-wave Dickson charge pump used to convert incident RF energy into system DC power [80, 108–111]. The circuit is a six stage charge pump built with low-threshold Schottky diodes.

The power harvesting circuit accepts an input RF signal and outputs both an unregulated, harvested voltage and a second signal that follows the communication envelope of the incident signal. This envelope is the demodulated, downlink baseband data.

Shunt voltage regulator

The harvested voltage output from the power harvesting circuit (RF-to-DC converter) widely varies relative to incident RF power. For this reason a voltage regulator is needed to maintain a constant voltage for the system components. In the integrated backscatter sensing circuit, this is done using a shunt voltage regulator.

When the input voltage is above 3 V, the regulator pulls excess current to ground

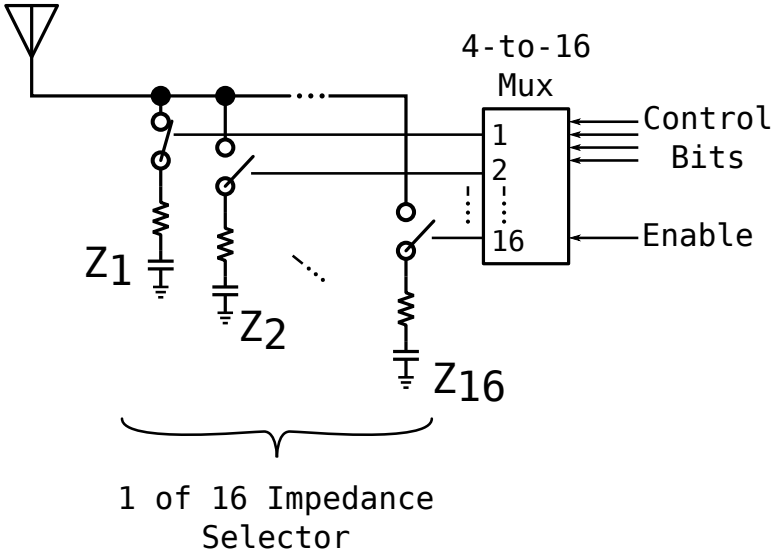

FIGURE 8.4: Block diagram of the 16-QAM backscatter modulator

through a FET. This results in a stable 3 V output from the regulator.

Bandgap voltage reference

The voltage regulator is intended to be operated in conjunction with the silicon bandgap voltage reference. This circuit outputs a temperature-independent fixed voltage output of ≈1.25V.

Ring oscillators

Two current-controlled, 5-stage current-starved ring oscillators are included on the chip. In initial testings, the ring oscillators have a frequency output range that varies from several kHz (≈10kHz) to tens of MHz (≈40MHz). One oscillator is controlled by an external current that allows for interfacing with a wide variety of analog sensors. The second oscillator is internally enabled and connected to a photodiode. When fabricated with a glass package, the integrated backscatter sensing circuit may function as a remote light detection circuit.

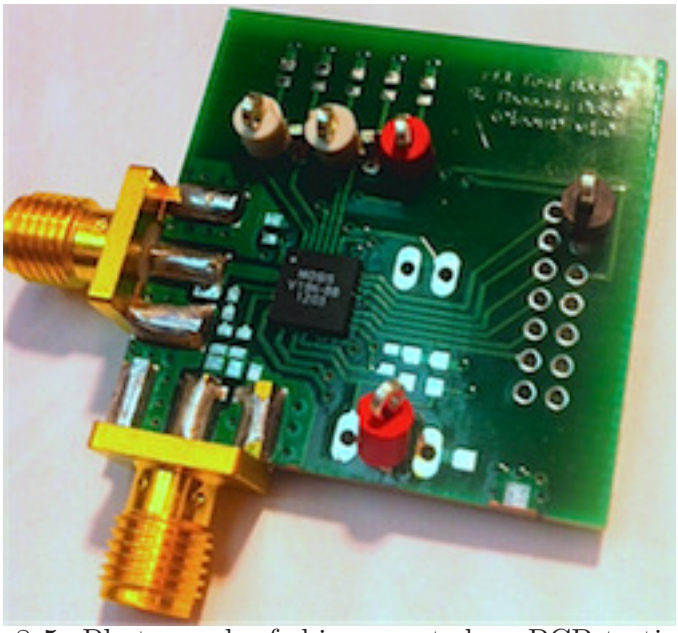

FIGURE 8.5: Photograph of chip mounted on PCB testing board

8.2 Description of the integrated 16-QAM modulator

A schematic for the modulator is shown in Fig. 8.4. The 16 state QAM modulator is implemented as a set of 16 individual impedances formed by series R and C combinations that are individually switched into connection with the antenna. Transistor size was selected based on previously published results [112]. The connection is controlled by a 4-to-16 multiplexer (MUX) with 4 input bits as well as a fifth line used for enabling the multiplexer. With this design, a set of input bits is mapped to an individual impedance that gets connected to the antenna.

The implemented individual impedance values are shown in Table 8.1. The set of values is designed around a 50 Ω antenna with incident carrier frequency of 915 MHz. The expected constellation shown on a Smith chart can be seen on the left side of Fig. 5.16. A benefit of the custom analog CMOS design is the selection of resistor and capacitor values is not limited to the selection available in standard packages (i.e. standard 5% resistor values). This allows for finer resolution when designing

the backscatter QAM constellation.

The circuit layout of the modulator was designed to minimize RF transmission line and parasitic effects. The individual switch and impedance combinations are placed evenly around a common RF trace that connects to the external antenna. With this design, the electric length between elements physically closest to the antenna pad and elements the farthest away is minimized. However, during design and simulation of the chip, model-based parasitic extraction capable estimating parasitic effects of the layout was not performed. For this reason, the selection of impedance states was made assuming minimal parasitic effect.

8.3 Experimental measurement setup

A photograph of the integrated backscatter sensing chip mounted on the printed circuit board (PCB) test fixture is shown in Fig. 8.5. The fabricated and packaged chip is seen in the middle of the circuit board. The leftmost SMA connector is used for attaching external measurement tools or an antenna to the 16-QAM backscatter modulator. Test pins include the 4 digital lines that control the 4-to-16 multiplexer of the modulator, multiplexer enable, and externally applied power and ground for semi-passive operation.

Operation of the 16-QAM modulator was validated by measuring the reflection coefficients of each constellation point using a VNA connected through a 50 Ω cable. This measurement, shown in Fig. 8.6, uses the coaxial cable and VNA input impedance to model circuit interaction with an external antenna. As shown in previous chapters, reflection coefficients may be used to estimate performance of the backscatter QAM signaling constellation.

Using the network analyzer, modulator impedance was measured over varying input frequency and RF power levels. Initial measurements suffered from poor VNA calibration and calibration plane reference. Measurements were taken with the net-

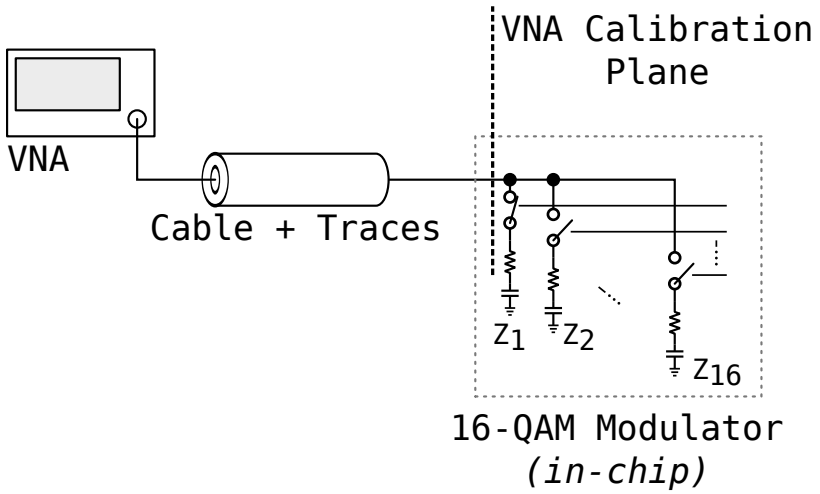

FIGURE 8.6: Measurement setup for chip reflection coefficients

work analyzer calibrated to the input pad of the modulator. Due to undesired parasitic elements stemming from the pad connection, internal wirebond inductance and chip parasitic capacitance, it was necessary to calibrate internally to the 16-QAM modulator.

8.3.1 Network analyzer calibration

Calibration was extended by determining the 2-port S parameter set that removes the common parasitic elements. Using the network analyzer, the measured reflection coefficient is

$$\Gamma_{\text{Meas.}} = e_{00} + (e_{10}e_{01})\frac{\Gamma_{\text{Actual}}}{1 - e_{11}\Gamma_{\text{Actual}}} \tag{8.1}$$

where e_{00} is the directivity error, $(e_{10}e_{01})$ is the reflection tracking error, e_{11} is the source match error and Γ_{Actual} is the actual value of the reflection coefficient as pictured in Fig. 8.7. In this diagram, a_0 and b_0 represent waves flowing into and out of the first port of the S-parameter network and a_1 and b_1 represent the waves flowing into and out of the second port.

The equation above reduces to a set of three unknowns that can be solved for using three known impedances. While generally this correction is made using the

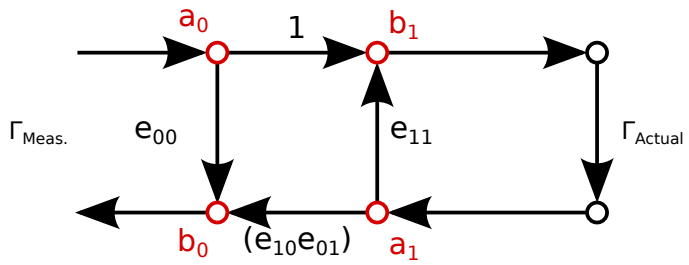

FIGURE 8.7: Two-port VNA error correction network

open, short, and match impedance set, this practice mainly serves to simplify the correction matrix and is not a fundamental requirement.

After assigning

$$a = (e_{10}e_{01}) - e_{00}e_{11} \tag{8.2}$$

$$b = e_{00} \tag{8.3}$$

$$c = -e_{11}, \tag{8.4}$$

the corrected or actual measurement becomes

$$\Gamma_{\text{Actual}} = \frac{\Gamma_{\text{Meas.}} - b}{a - c \cdot \Gamma_{\text{Meas.}}} \tag{8.5}$$

and the values of a, b, and c may be found by solving the correction matrix

$$\begin{bmatrix} \Gamma^1_{\text{Actual}} & 1 & -\Gamma^1_{\text{Actual}}\Gamma_{\text{Meas.}} \\ \Gamma^2_{\text{Actual}} & 1 & -\Gamma^2_{\text{Actual}}\Gamma_{\text{Meas.}} \\ \Gamma^3_{\text{Actual}} & 1 & -\Gamma^3_{\text{Actual}}\Gamma_{\text{Meas.}} \end{bmatrix} \times \begin{bmatrix} a \\ b \\ c \end{bmatrix} = \begin{bmatrix} \Gamma^1_{\text{Meas.}} \\ \Gamma^2_{\text{Meas.}} \\ \Gamma^3_{\text{Meas.}} \end{bmatrix}. \tag{8.6}$$

After DC confirmation of modulator impedance values, the correction matrix was overconstrained using the full 16-state set of impedances and solved. This provides a correction matrix that is applied to other chips extending the network analyzer calibration plane into the chip.

8.4 Measurement results

A summary of results are shown in Table 8.1. In this table, the DC lumped element component values are shown for each of the sixteen modulator states. Also included

Table 8.1: Measurement Results from integrated backscatter sensing chip

	Implemented		Measured		Ideal		% Error
	R (Ω)	C (pF)	Γ* (915 MHz)		Γ* (915 MHz)		$\frac{\lvert\Gamma^*_{\text{Meas.}}-\Gamma^*_{\text{Ideal}}\rvert}{\lvert\Gamma^*_{\text{Ideal}}-\hat{\Gamma^*_{\text{Ideal}}}\rvert}$
Z_1	18.63	4.89	-0.100	- j0.58	-0.148	- j0.60	24.10 %
Z_2	28.59	3.15	0.074	- j0.49	0.148	- j0.60	61.33 %
Z_3	54.49	4.74	0.142	- j0.30	0.148	- j0.30	3.24 %
Z_4	31.58	8.22	-0.110	- j0.17	-0.149	- j0.30	63.41 %
Z_5	4.18	4.12	-0.098	- j0.78	-0.149	- j0.89	27.44 %
Z_6	5.68	2.97	0.175	- j0.64	0.149	- j0.90	54.28 %
Z_7	67.44	0.00	0.093	- j0.15	0.149	- j-0.00	34.15 %
Z_8	37.06	0.00	-0.195	+ j0.01	-0.149	+ j0.00	10.22 %
Z_9	9.16	7.15	-0.450	- j0.57	-0.446	- j0.59	5.00 %
Z_{10}	33.57	1.93	0.296	- j0.65	0.448	- j0.60	33.91 %
Z_{11}	90.35	2.31	0.416	- j0.37	0.447	- j0.30	16.09 %
Z_{12}	16.14	12.73	-0.355	- j0.18	-0.450	- j0.30	31.51 %
Z_{13}	0.00	5.62	-0.369	- j0.67	-0.447	- j0.89	38.17 %
Z_{14}	0.00	2.15	0.468	- j0.75	0.448	- j0.89	23.42 %
Z_{15}	130.70	0.00	0.342	+ j0.06	0.447	+ j0.00	18.75 %
Z_{16}	19.13	0.00	-0.490	- j0.02	-0.447	- j-0.00	7.40 %

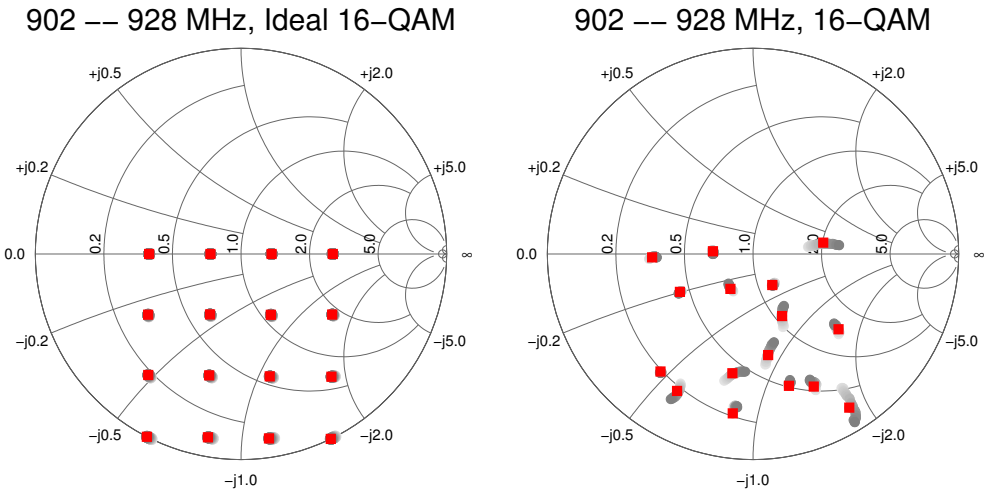

Ideal (a) Measured (b)

FIGURE 8.8: Ideal (a) and measured (b) 16-QAM constellation over 902–928 MHz band

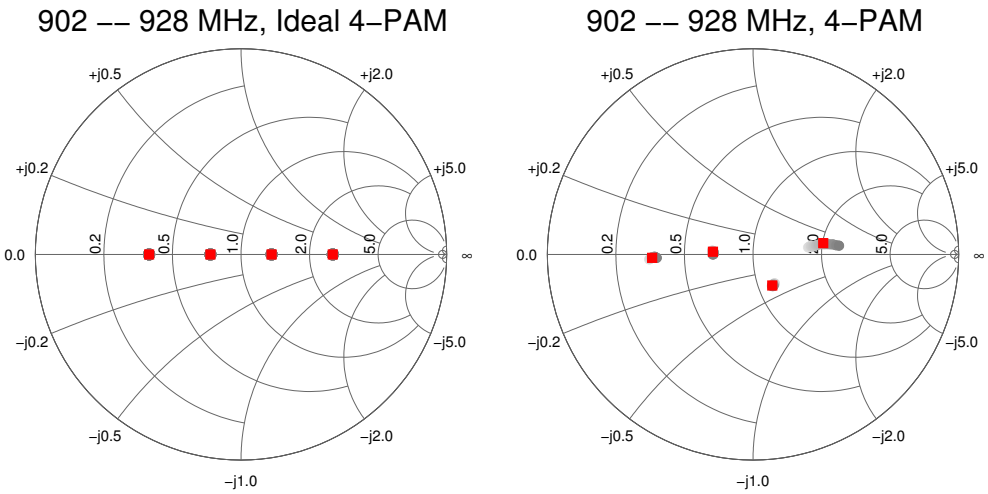

Ideal (a) Measured (b)

FIGURE 8.9: Ideal (a) and measured (b) 4-PAM constellation over 902–928 MHz band

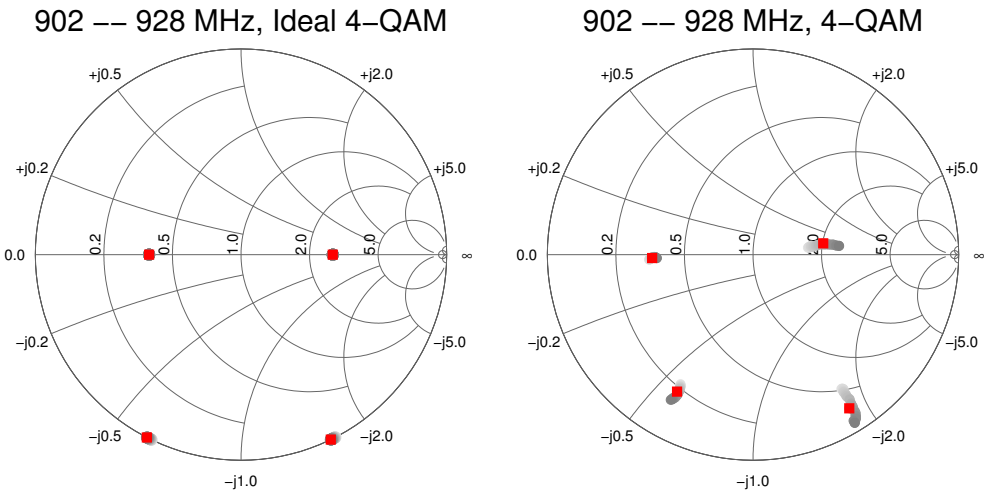

Ideal (a) Measured (b)

FIGURE 8.10: Ideal (a) and measured (b) 4-QAM constellation over 902–928 MHz band

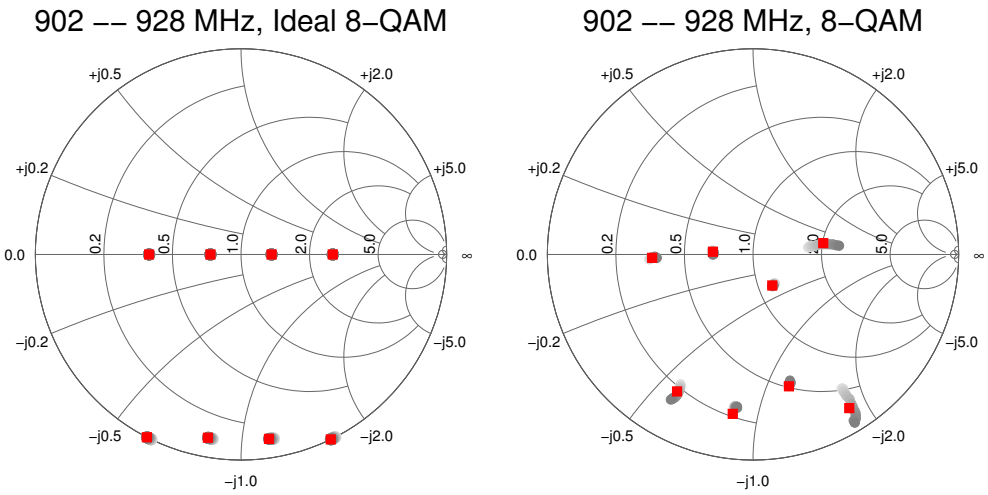

Ideal (a) Measured (b)

FIGURE 8.11: Ideal (a) and measured (b) 8-QAM constellation over 902–928 MHz band

are the measured Γ^* values at 915 MHz compared to the expected or ideal Γ^* values for the rectangular 16-QAM constellation. The final column shows EVM values for each of the sixteen states as compared to the ideal symbol location (ideal Γ^* constellation with DC component removed). The modulator exhibits high EVM values resulting from unaccounted for parasitic effects that will be further outlined in the next section.

The measurement values for the full 16-QAM backscatter constellation are shown in Fig. 8.8 compared to the ideal locations. In this measurement, the frequency is swept across the entire 900 MHz ISM band regulated by the FCC in the United States. As expected from the EVM values shown in Table 8.1, the 16-QAM constellation does not compare favorably to the ideal constellation.

Subsets of the constellation were extracted. Measurements for a 4-PAM, 4-QAM, and 8-QAM signaling schemes are presented below in Figures 8.9, 8.10, and 8.11 which allow for transfer of 2 bits/symbol, 2 bits/symbol, and 3 bits/symbol respectively.

Table 8.2: Measured constellation average EVM and symbol distance

Constellation	Avg. EVM (f = 915 MHz)
16-QAM	28.28 %
8-QAM	26.73 %
4-QAM	21.94 %
4-PAM	17.63 %

The EVM for each constellation was measured and summarized in Table 8.2. The 4-PAM constellation presents the lowest average EVM value for its symbol set. These impedance values consist only of resistive components and no lumped element capacitors. Since the impedance of an (ideal) resistor is not frequency dependent, the 4-PAM constellation is less susceptible to carrier frequency variation. The 4-QAM constellation, however, is composed of resistors and capacitors resulting in a carrier frequency dependent constellation. The average EVM of this constellation is higher as compared to the 4-PAM constellation, but the overall average symbol distance is greater. This results in a increased average backscatter power for the 4-QAM constellation.

These results prove that implementation of a multi-state vector backscatter modulator in standard CMOS processes is possible.

8.5 Accounting for undesired parasitic elements

As shown in Fig. 8.8, the sixteen measured values do not align with the expected, ideal 16-QAM constellation. In designing the backscatter modulator implemented in this chip, RF parasitic extraction using tools compatible with the CMOS layout software was not performed. This did not allow for complete simulation, estimation, or extraction of transmission line effects and parasitic elements that are present in the fabricated design at the UHF frequencies the constellation was designed around. Though the modulator was placed in such a way to reduce unwanted parasitic effects,

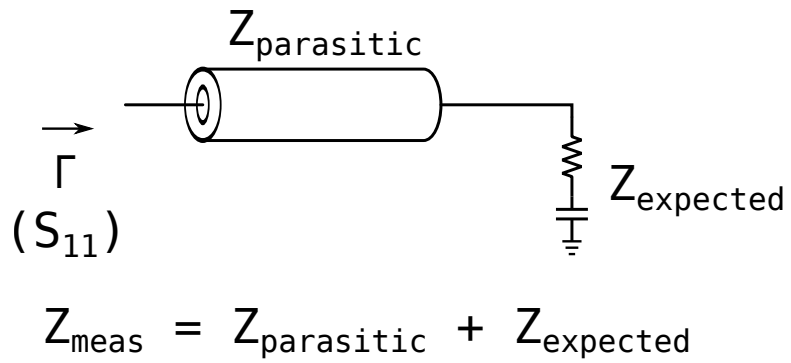

FIGURE 8.12: Transmission line parasitics to be corrected

it was not possible at design time to account for everything.

The result is the deviation from ideal impedance values present in the measured chip for the individual impedance states. While calibration and matching can account for the common transmission line effects, it cannot account for the individual variation. This effect is modeled in Fig. 8.12. The measured impedance value is the summation of parasitic elements including parasitic transmission line effects and parasitic capacitance as well as the implemented, expected impedance.

When designing a discrete component backscatter modulator, it is possible to compensate for the undesired parasitic effects by changing the impedance components. The measured impedance value is

$$Z_{\text{Meas.}} = Z_{\text{parasitic}} + Z_{\text{expected}} \tag{8.7}$$

or the summation of the parasitic effects as well as the implemented or expected impedance. Solving for the parasitic effect and subtracting from the initial implemented value yields a new impedance, Z_{new}. Placing this new impedance in the circuit results in the initially expected value being measured. The equation for this is written as

$$Z_{\text{Meas.-New}} = Z_{\text{parasitic}} + \underbrace{Z_{\text{new}}}_{Z_{\text{expected}} - Z_{\text{parasitic}}} \tag{8.8}$$

This method was used in the previous chapter when designing the discrete-component

Table 8.3: Parasitic cancelled impedance values

	New Values		Measured†		Ideal		% Error
	R (Ω)	C (pF)	Γ* (915 MHz)		Γ* (915 MHz)		$\frac{\lvert\Gamma^*_{\text{Meas.}}-\Gamma^*_{\text{Ideal}}\rvert}{\lvert\Gamma^*_{\text{Ideal}}-\hat{\Gamma^*_{\text{Ideal}}}\rvert}$
Z_1	13.37	0.00	-0.232	- j0.59	-0.148	- j0.60	39.77 %
Z_2	16.54	18.68	0.134	- j0.67	0.148	- j0.60	34.90 %
Z_3	50.81	47.20	0.141	- j0.35	0.148	- j0.30	23.72 %
Z_4	25.26	26.15	-0.133	- j0.32	-0.149	- j0.30	13.40 %
Z_5	0.00	0.00	-0.185	- j0.93	-0.149	- j0.89	10.86 %
Z_6	0.00	0.00	0.142	- j0.94	0.149	- j0.90	9.01 %
Z_7	77.83	0.00	0.150	+ j0.00	0.149	+ j0.00	0.67 %
Z_8	40.55	0.00	-0.147	+ j0.01	-0.149	+ j0.00	2.65 %
Z_9	8.86	608.00	-0.451	- j0.58	-0.446	- j0.59	2.93 %
Z_{10}	36.49	10.12	0.461	- j0.62	0.448	- j0.60	5.35 %
Z_{11}	104.78	43.41	0.461	- j0.32	0.447	- j0.30	5.56 %
Z_{12}	10.28	65.93	-0.445	- j0.28	-0.450	- j0.30	3.23 %
Z_{13}	0.00	102.02	-0.428	- j0.84	-0.447	- j0.89	9.63 %
Z_{14}	0.00	0.00	0.405	- j0.81	0.448	- j0.89	14.46 %
Z_{15}	140.22	13.81	0.376	+ j0.00	0.447	+ j0.00	11.10 %
Z_{16}	20.12	0.00	-0.469	+ j0.00	-0.447	+ j0.00	3.51 %
						Avg. Error:	**11.92 %**

† Constellation adjusted at 928 MHz, and new impedance values measured at 915 MHz in post-processing

backscatter QAM modulator.

However, for a single-chip implementation this iterative design process is not possible as the impedance values are set at design time when the chip is sent to fabrication. Without accurate parasitic extraction tools, it is not possible at design time to predict the impedance values presented to the antenna. For this reason, an investigation of what is possible if the parasitic elements are known is provided.

8.6 Results with compensation for parasitic effects

Parasitic effects were determined at 928 MHz based on the known implemented impedance values in the modulator. New impedance values were then formed to cancel these effects as shown in equation (8.8). The range of possible impedances was limited to passive resistors and capacitor networks. The new impedances were

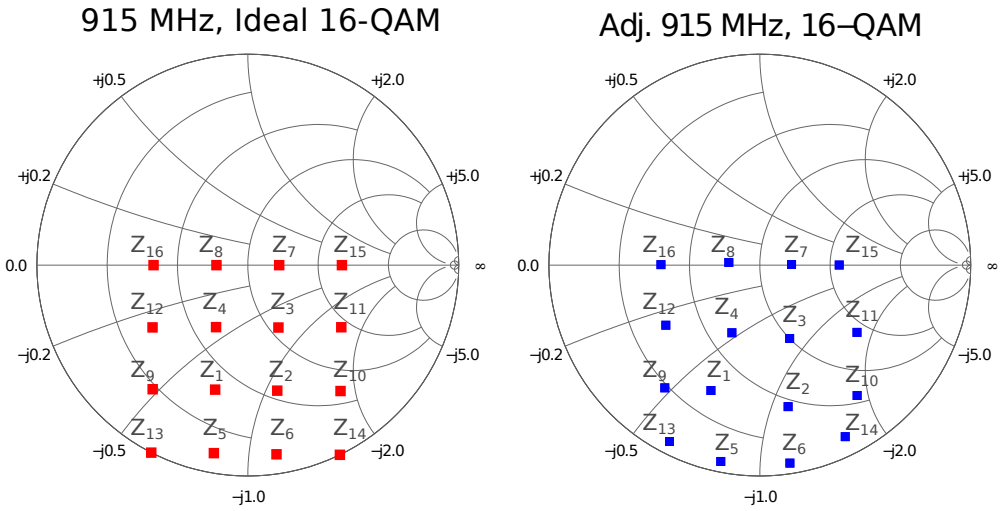

Ideal (a)

Adjusted Z (b)

FIGURE 8.13: Ideal 16-QAM constellation compared to adjusted constellation.

then measured at a carrier frequency of 915 MHz. In MATLAB, the resistance and frequency-dependent reactance for the additional impedance values (Z_{new}) were found for the carrier frequency of 915 MHz. This new impedance was summed with the original measured values to model the expected performance of a second iteration of the single-chip modulator assuming knowledge of the modulator parasitics. The results from this operation are summarized in Table 8.3.

After adjustment, the average error (EVM) reduces to 11.92% for the sixteen states. Previously, the average EVM was 28.28% for the 16-QAM constellation. One interesting result is that the new impedance values for states 5, 6, and 14 are the same (Z = short). This is an artifact of the passive RC network constraint and indicates that the individual parasitic effects for these states are too strong for complete cancellation. The average symbol error for these positions (i.e. parasitic effects only) is 11.4%.

Figure 8.13 shows the parasitic constellation on a Smith chart compared to the ideal constellation. Numerical results for this result are listed in Table 8.3. In

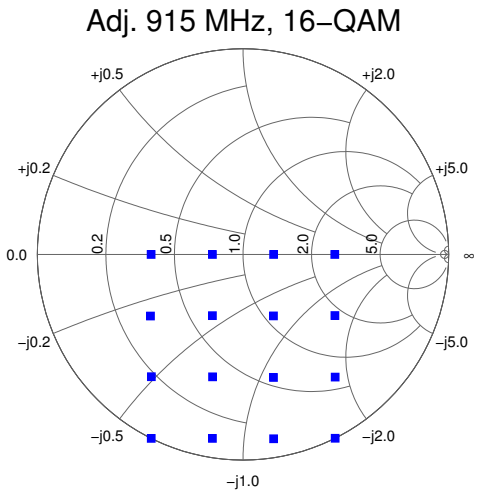

FIGURE 8.14: Adjusted 16-QAM constellation, compensated at 915 MHz.

this measurement, it is assumed that parasitics are equal across different chips and impedances can be changed without introducing new transmission line parasitic effects. The parasitics were cancelled at frequency 928 MHz and then measured at 915 MHz to model a realistic expectation by allowing for some transmission line effects to remain present in the data.

For comparison, Fig. 8.14 shows the 16-QAM constellation at 915 MHz when parasitics have been cancelled at the same frequency. This constellation supports the claim that QAM backscatter is compatible with a single-chip design using only R and C components. However, to achieve this result, the parasitic effects must be known and characterized, whether by simulation models or an iterative design process.

8.7 Chapter conclusion

In this chapter, the first single-chip implementation of a QAM backscatter modulator has been presented. The modulator uses passive R and C lumped element components to form the required set of complex load impedances. Performance of the chip was evaluated using a VNA to model a 50 Ω antenna connected to the modulator

input.

With the existing chip, 4-PAM, 4-QAM, and 8-QAM backscatter signaling constellations are possible using subsets of the 16 modulator states. This chapter also provides a plan for future single-chip work. Assuming accurate parasitic models are available, a method to form a set of modified impedances that effectively cancel the parasitics is shown. Using MATLAB, this method was applied the 16-QAM modulator in post-processing and expected constellations were presented.

9

Conclusion and future work

This thesis has presented an energy efficient communication technique based on an extension to backscatter technology. The extension includes high data rates (up to 96 Mbps) and QAM. Performance of QAM backscatter with data rates up to 80 Mbps was shown in a highly-multipath measured indoor channel. For benign channels, an experimental demonstration of 96 Mbps (15.5 pJ/bit) was presented using a discrete component modulator. We have demonstrated a single-chip device that incorporates binary backscatter modulation with a data rate of 5 Mbps. This chip has been used for multichannel wireless biosignal recording as well as the first demonstration of streaming multichannel audio and images over a backscatter link. An integrated single-chip QAM bakcsatter modulator was then designed. This chip, the first integrated backscatter QAM modulator, was characterized and proven capable of multi-state vector modulation.

In Chapter 1, the problem was formed. Motivation for power reduction in the communication subsystem of wireless sensing devices was shown. As shown in Chapter 2, existing backscatter technology as employed by UHF RFID devices offers a low-power radio solution but has been limited to data rates below 640 kbps.

In Chapter 3, the physical layer is re-examined starting with the basic equations for the fields scattered from an antenna. It was shown that the scattered fields consist of a constant structural scattering term and a load-dependent scattering term. Switching between load impedances connected to the antenna causes changes in the magnitude and phase of the scattered field. The analysis in this chapter focused on the complex nature of the changes being preserved in contrast to analysis techniques using the antenna RCS. Using this observation, a method to generate multi-state QAM backscatter was introduced. This included a method for constraining the signalling constellation to fit with passive networks and a method for generating constellations compatible with single-chip CMOS integration.

A communication system based on the use of scattered fields for data transfer was defined in Chapter 4. This system consists of a reader and one or more tags. The reader generates and transmits the carrier signal to the tag and also performs data demodulation on the incoming fields. The tag responds to the incident field from the reader by modulating between multiple states. A baseband vector signal model for analyzing the received fields at the reader was presented. Using this model, the effect of Doppler shift was analyzed and shown to be negligible at the UHF frequencies used in this thesis.

These observation were used to design and build a discrete component QAM backscatter modulator. The results from two devices were presented in Chapter 5. Initial characterization was performed on a modulator designed for 4-QAM/4-PSK signalling. This included an experimental data transfer of 400 kbps. Based on these results, a tag supporting 16-QAM backscatter modulation was designed and built. Using the 16-QAM modulator, an experimental data transfer of 96 Mbps was shown. This data was taken in an indoor environment relatively free of clutter. The measured communication efficiency of the 16-QAM modulator is 15.5 pJ/bit. While data rates are comparable to IEEE 802.11 (WiFi), the radio power consumption is

reduced by a factor of over 100x from 10 nJ/bit [21].

Achievable performance in more realistic scenarios was evaluated in Chapter 6. Backscatter QAM modulation was analyzed in a highly-multipath measured indoor environment. For successful data reception, a receiver implementing adaptive channel equalization was designed. The receiver was evaluated in simulated channel models as well as an experimentally measured channel.

This chapter showed that an adaptive equalizer can dramatically improve transfer from a QAM backscatter device in non-ideal channels. For a data rate of 20 Mbps, the adaptive equalizer improves average EVM performance by 9% compared to a linear equalizer and 59% average EVM improvement compared to the unequalized signal. While the receiver generally adapted to the channel and was able to detect the data, in areas with significant multipath, increased ISI negatively impacted equalizer performance. In such multipath environments, data transfer can be improved by lowering the backscatter data rate. This suggests a need for protocols with adaptive data rates to be implemented in future designs.

A single-chip modulated backscatter telemetry device was designed for low-power sensing. This chip includes a high-data rate backscatter modulator capable of streaming data at 5 Mbps (4 pJ). The chip includes 10 amplifiers designed for neural signals, 4 amplifiers designed for EMG signals, and 2 dc amplifiers. These channels are sampled on-chip and transmitted as digital data. In Chapter 7, this chip was shown to successfully transmit neural recordings. This was further exploited to stream multi-channel (stereo) audio and images from the tag to the reader. This work represents the first generation of rich-media tags capable of streaming data over the low-power backscatter link.

A 16-QAM backscatter modulator was miniaturized and fabricated using a CMOS process. This device, the first ever single-chip 16-QAM backscatter modulator, was characterized in Chapter 8 and proven capable of generating multi-state vector mod-

ulation. However, the full 16-QAM constellation is not clearly defined due to chip parasitic effects. If parasitics were able to be accounted for, whether by simulation tools or a second fabricated run, the expected constellation was shown. This analysis will aid future circuit designers.

To summarize, the original contributions of this thesis are:

- A technique for low-power generation of vector modulated backscatter (i.e. QAM backscatter).
- Simulation of M-ary QAM and first experimental confirmation of 4-PAM, 4-QAM/4-PSK, 16-QAM modulated backscatter.
- Highest reported to date backscatter data rate (96 Mbps, 15.5 pJ/bit).
- Backscatter based wirelessly powered system for wireless, in-flight multichannel biosignal recording of freely-moving insects.
- First demonstration of a "rich-media" backscatter tag capable of streaming multichannel digital audio and image transmission (5 Mbps, 4 pJ/bit)
- First IC implementation of QAM backscatter modulator.
- Demonstrated use of channel equalizer to compensate for tag motion and channel multipath effects in wideband QAM backscatter communication.

Multi-state vector backscatter modulation is a field with great potential. Interest has increased in QAM backscatter since the author's initial publication in 2010 [15–17, 113, 114]. Multi-state backscatter modulation, based on the principles outlined in this document, will aid future developments within the low-power sensor, communications, and RFID community.

9.1 Future work

9.1.1 Battery-free backscatter QAM

The impact of QAM backscatter modulation on the power harvesting circuits of passive devices is uncertain. Typically, passive UHF RFID tags implement a diode based charge pump for RF-to-DC power conversion. This nonlinear circuit presents a frequency and power dependent load to the antenna. During modulation, the impedance of the power harvesting circuit represents one of the binary symbols. The second symbol is formed by introducing a deliberate impedance mismatch in parallel with the power harvester. The harvesting efficiency of the circuit is reduced for the duration of the mismatch state. The effect of the nonlinear diode impedance acting in parallel or included as one symbol of a backscatter QAM constellation is an open problem.

In the author's initial paper proposing QAM backscatter, physically disconnecting the power harvesting circuit during backscatter modulation was suggested for passive operation [17]. This would require a large capacitor for charge storage and low duty cycle transmissions to allow ample time for sufficient charge accumulation.

Alternatively, passive operation may be achieved by exploiting polarization diversity. A circularly polarized reader allows the tag to implement a dedicated linearly polarized antenna for power harvesting and a second orthogonally polarized antenna dedicated to backscatter modulation. This method has been similarly applied to other passive devices but introduces a 3 dB ($\approx$50%) polarization penalty and makes miniaturization difficult [115].

Connecting the QAM backscatter modulator in parallel with the power harvester would allow a portion of the incident signal to be absorbed during modulation. A 4-QAM backscatter model using this method was recently presented [113]. However, the impedance of the power harvesting circuit may change within the duration of

a packet transmission causing distortion of the received QAM constellation. The wideband adaptive receiver presented in this work may pave the way for successful operation of backscatter QAM in conjunction with a harvester.

9.1.2 Tag multiple access

Existing backscatter devices utilize a slotted algorithm to implement time-division multiple access (TDMA). This remains a valid option for future QAM backscatter devices. However, an exploration of code division multiple access (CDMA) and, frequency division or frequency diversity using orthogonal frequency division multiplexing (OFDM) remains to be demonstrated. Signalling using orthogonal frequency division multiplexing (OFDM) over backscatter requires an increased computational expense in the form of an inverse Fourier transform operation as well as fine resolution of the IQ signalling space.

The main problem standing in the way of building the OFDM modulator is circuit implementation of the impedance selector. Work in this thesis has focused on M-ary QAM constellations of size $M = 16$ and below implemented with M sets of impedance values. However, this is not the only architecture for backscatter QAM. It may not be feasible to implement a sufficient number of individual lumped element combinations required for the desired resolution on a PCB or single-chip. For this reason a weighted impedance selector or digital to analog impedance converter will need to be designed. Due to the nonlinear transformation and warping of IQ space that results from impedance to reflection coefficient conversion, design of the weighted elements will not be straightforward. Successful design of this circuit will allow for frequency diversity from a low-power device that does not run a UHF oscillator or traditional transceiver.

Multiple access for tags will enable higher read rates and tag population density. Currently, tags wait through a randomized slotted read cycle to deliver their ID code.

Using TDMA, only one tag may talk at a time. Frequency division multiple access will allow for multiple tags to simultaneously communicate back to the reader. This will increase the total bandwidth of a tagged environment. As RFID research moves further into the wireless sensing domain, multiple access for streaming tag data will be an important issue.

9.1.3 Adaptive constellation protocols

This work has shown that even with an adaptive equalizer at the receiver, an adaptive constellation protocol is needed. As the received signal power is minimized in various locations of the time varying backscatter channel, the reader needs to inform the tag to lower its data rate or lower its constellation order. Either of these actions will result in an increased signal to noise ratio at the reader. As shown in this thesis, a tag that implements 16-QAM modulation can also generate 4-QAM or 4-PAM or even binary modulation. Adaptive protocols will allow for data transfer in locations where a successful 16-QAM signalling would not otherwise be possible.

9.1.4 Channel sounding and sensing

The use of vector modulation may aid in future channel sounding and sensing. The QAM constellation transmitted from a tag can be used to observe and measure the attenuation and phase rotation of the return channel as the tag is moved or the channel changes. Future sensors may take advantage of this effect and simultaneously transfer data and sense channel effects. Alternatively, QAM backscattering devices may be placed throughout an environment and used to measure a channel. This would offer an inexpensive means to measure a channel as compared to the method presented in chapter 6.

9.1.5 Applications

With experimentally demonstrated data rates of 96 Mbps, a large amount of bandwidth is available for low-power tags. There are several application areas where such high bandwidth for a low-power device will be useful.

- Remote biosignal acquisition

  Behavioral scientists and neurobiologists investigating animals are limited in the amount of neural or other signals that may be obtained from their subjects. Backscatter communication is an excellent solution for this problem. Greatly increasing the achievable data rates allows for more signals to be transmitted and recorded. Even semi-passive (battery-assisted) devices or replacement of the free space propagation channel with coaxial cables carrying both power and communication, will yield improved bandwidth and chip power savings.

  Future work will continue to explore recording of neural, EMG, EEG, as well as other biosignals. The techniques presented in this thesis have focused on far-field RCS and backscattering. However, the principles are also applicable to near-field RFID scenarios. Near-field vector backscatter modulation will allow for implanted devices to record and stream large amounts of *in vivo* data. By attaching low-power cameras, this could include *in vivo* video useful for diagnosis.

- Secure object identification

  The cryptographic community has shown great interest in devices such as the Intel WiSP that would enable secure transactions with passive devices [49,116]. However, the small payload available has limited the amount of data that can be transferred and therefore size and security of the keys.

With extremely high data rates, long cryptographic keys are possible for low-power backscatter devices. This can be used for authenticated data transfer and identification.

- Remote video recording

  Streaming audio and images over a backscatter link has been demonstrated in this work. An obvious next step is interfacing a low-power camera for full-motion video. With multiple camera streams from a single or multiple tags, it will be possible for a passive device(s) to record a scene from multiple angles and stream the data to a reader. This would enable scene reconstruction or other video analysis to take place (offline or otherwise).

Bibliography

[1] Toumaz Microsystems Ltd, "Telran TZ1053: Toumaz extremely low power radio network," Electronic, February 2012.

[2] R. Harrison and C. Charles, "A low-power low-noise CMOS amplifier for neural recording applications," *IEEE Journal of Solid-State Circuits*, vol. 38, no. 6, pp. 958–965, June 2003.

[3] I. F. Akyildiz, T. Melodia, and K. R. Chowdhury, "A survey on wireless multimedia sensor networks," *Computer Networks*, vol. 51, no. 4, pp. 921–960, 2007.

[4] G. Mathur, P. Desnoyers, P. Chukiu, D. Ganesan, and P. Shenoy, "Ultra-low power data storage for sensor networks," *ACM Transactions on Sensor Networks*, vol. 5, no. 4, pp. 33:1–33:34, Nov. 2009. [Online]. Available: http://doi.acm.org/10.1145/1614379.1614385

[5] V. Pop, R. de Francisco, H. Pflug, J. Santana, H. Visser, R. Vullers, H. de Groot, and B. Gyselinckx, "Human++: wireless autonomous sensor technology for body area networks," in *Proceedings of the 16th Asia and South Pacific Design Automation Conference*, ser. ASPDAC 2011. Piscataway, NJ, USA: IEEE Press, 2011, pp. 561–566.

[6] R. R. Harrison, H. Fotowat, R. Chan, R. J. Kier, R. Olberg, A. Leonardo, and F. Gabbiani, "Wireless neural/EMG telemetry systems for small freely moving animals," *IEEE Transactions on Biomedical Circuits and Systems*, vol. 5, no. 2, pp. 103 – 111, April 2011.

[7] S. J. Thomas, R. R. Harrison, A. Leonardo, and M. S. Reynolds, "A battery-free multi-channel digital neural/EMG telemetry system for flying insects," in *IEEE Biomedical Circuits and Systems Conference*, 2011, pp. 229 – 232.

[8] ——, "A battery-free multichannel digital neural/EMG telemetry system for flying insects," *IEEE Transactions on Biomedical Circuits and Systems*, vol. 6, no. 5, pp. 424–436, October 2012.

[9] V. Liepa and T. Senior, "Modification to the scattering behavior of a sphere by reactive loading," *Proceedings of the IEEE*, vol. 53, no. 8, pp. 1004 – 1011, August 1965.

[10] A. E. Fuhs, *Radar Cross Section Lectures*. AIAA, New York, NY, 1982.

[11] J. Blacksmith, P. and R. Mack, "On measuring the radar cross sections of ducks and chickens," *Proceedings of the IEEE*, vol. 53, no. 8, p. 1125, August 1965.

[12] D. M. Pozar, *Microwave Engineering*, 3rd ed. John Wiley & Sons Ltd, 2005 (Chapter 13).

[13] C. A. Balanis, *Antenna Theory*, 3rd ed. John Wiley & Sons, Inc., Hoboken, New Jersey, 2005 (Chapter 2).

[14] EPC Global US, "Class 1 Generation 2 UHF RFID protocol for operation at 860MHz-960MHz, version 1.0.9," Available online, *http://www.epcglobalus.org/*, 2005.

[15] S. J. Thomas, E. Wheeler, J. Teizer, and M. S. Reynolds, "Quadrature amplitude modulated backscatter in passive and semipassive UHF RFID systems," *IEEE Transactions on Microwave Theory and Techniques*, vol. 60, no. 4, pp. 1175–1182, April 2012.

[16] S. J. Thomas and M. S. Reynolds, "A 96 Mbit/sec, 15.5 pJ/bit 16-QAM modulator for UHF backscatter communication," in *2012 IEEE International Conference on RFID*, April 2012, pp. 185–190.

[17] S. Thomas and M. Reynolds, "QAM backscatter for passive UHF RFID tags," in *2010 IEEE International Conference on RFID*, April 2010, pp. 210 – 214.

[18] B. Otis, Y. Chee, and J. Rabaey, "A 400μw-RX, 1.6mW-TX super-regenerative transceiver for wireless sensor networks," in *IEEE International Solid-State Circuits Conference*, 2005.

[19] W. Kluge, F. Poegel, H. Roller, M. Lange, T. Ferchland, L. Dathe, and D. Eggert, "A fully integrated 2.4-GHz IEEE 802.15.4-compliant transceiver for ZigBee^{TM} applications," *IEEE Journal of Solid-State Circuits*, vol. 41, no. 12, pp. 2767–2775, December 2006.

[20] R. Staszewski, C. Hung, K. Maggio, J. Wallberg, D. Leipold, and P. Balsara, "All-digital phase-domain TX frequency synthesizer for Bluetooth radios in 0.13μ CMOS," in *IEEE International Solid-State Circuits Conference*, 2004.

[21] J. Jensen, R. Sadhwani, A. Kidwai, B. Jann, A. Oster, M. Sharkansky, I. Benbassat, O. Degani, S. Porat, A. Fridman, H. Shang, C. Chu, A. Ly, and M. Smith, "Single-chip WiFi b/g/n 1x2 SoC with fully integrated front-end and PMU in 90nm digital CMOS technology," in *IEEE Radio Frequency Integrated Circuits Symposium*, 2010.

[22] A. C. W. Wong, G. Kathiresan, C. K. T. Chan, O. Eljamaly, O. Omeni, D. McDonagh, A. Burdett, and C. Toumazou, "A 1V wireless transceiver for an ultra-low-power SoC for biotelemetry applications," *IEEE Journal of Solid-State Circuits*, vol. 43, no. 7, pp. 1511–1521, 2008.

[23] B. Cook, A. Berny, A. Molnar, S. Lanzisera, and K. Pister, "Low-power 2.4-GHz transceiver with passive RX front-end and 400-mV supply," *IEEE Journal of Solid-State Circuits*, vol. 41, no. 12, pp. 2757–2766, 2006.

[24] N. Cho, L. Yan, J. Bae, and H.-J. Yoo, "A 60 kb/s –10 Mb/s adaptive frequency hopping transceiver for interference-resilient body channel communication," *IEEE Journal of Solid-State Circuits*, vol. 44, no. 3, pp. 708–717, 2009.

[25] N. Cho, J. Bae, and H.-J. Yoo, "A 10.8 mW body channel communication/MICS dual-band transceiver for a unified body sensor network controller," *IEEE Journal of Solid-State Circuits*, vol. 44, no. 12, pp. 3459–3468, 2009.

[26] W. Wu, M. A. T. Sanduleanu, X. Li, and J. Long, "17 GHz RF front-ends for low-power wireless sensor networks," *IEEE Journal of Solid-State Circuits*, vol. 43, no. 9, pp. 1909–1919, 2008.

[27] C. Yoon, J. Lee, J. Lee, H. Park, J. Kim, J. S. Pak, and J. Kim, "Design of a low-noise UWB transceiver SiP," *IEEE Design Test of Computers*, vol. 25, no. 1, pp. 18–28, 2008.

[28] L. Xia, K. Shao, H. Chen, Y. Huang, Z. Hong, and P. Chiang, "0.15-nJ/b 3–5-GHz IR-UWB system with spectrum tunable transmitter and merged-correlator noncoherent receiver," *IEEE Transactions on Microwave Theory and Techniques*, vol. 59, no. 4, pp. 1147–1156, 2011.

[29] V. Pillai, H. Heinrich, D. Dieska, P. Nikitin, R. Martinez, and K. Rao, "An ultra-low-power long range battery/passive RFID tag for UHF and microwave bands with a current consumption of 700 na at 1.5 v," *IEEE Transactions on*

Circuits and Systems I: Regular Papers, vol. 54, no. 7, pp. 1500 – 1512, July 2007.

[30] S. J. Thomas, T. Deyle, R. Harrison, and M. S. Reynolds, "Rich-media tags: Battery-free wireless multichannel digital audio and image transmission with UHF RFID techniques," in *2013 IEEE International Conference on RFID*, 2013 (In Press).

[31] A. G. Bell, "Upon the production and reproduction of sound by light," *Journal of the Society of Telegraph Engineers*, vol. 9, no. 34, pp. 404–426, 1880.

[32] P. Nikitin, "Leon Theremin (Lev Termen)," *IEEE Antennas and Propagation Magazine*, vol. 54, no. 5, pp. 252 – 257, October 2012.

[33] H. Stockman, "Communication by means of reflected power," *Proceedings of the IRE*, vol. 36, no. 10, pp. 1196–1204, October 1948.

[34] E. M. Kennaugh, "The echoing area of antennas," Ohio State University Research Foundation Columbus Antenna Lab, Tech. Rep. Rpt. No. 601-14, December 1957.

[35] R. B. Green, "The general theory of antenna scattering," Ph.D. dissertation, Antenna Lab, The Ohio State University, United States – Ohio, 1963.

[36] R. E. Collin, "The receiving antenna," in *Antenna Theory, Part I*, R. E. Collin and F. J. Zucker, Eds. New York: McGraw-Hill Book Company, 1969.

[37] J. Tauritz, "A useful graphical representation in the theory of loaded scatterers," *IEEE Transactions on Antennas and Propagation*, vol. 18, no. 6, pp. 826 – 829, Nov 1970.

[38] R. Hansen, "Relationships between antennas as scatterers and as radiators," *Proceedings of the IEEE*, vol. 77, no. 5, pp. 659–662, May 1989.

[39] R. F. Harrington, "Theory of loaded scatterers," *Proceedings of the Institution of Electrical Engineers*, vol. 111, no. 4, pp. 617 – 623, April 1964.

[40] J. Schindler, R. Mack, and J. Blacksmith, P., "The control of electromagnetic scattering by impedance loading," *Proceedings of the IEEE*, vol. 53, no. 8, pp. 993 – 1004, August 1965.

[41] R. J. King, "An amplitude and phase measuring system using a small modulated scatterer," *Microwave Journal*, vol. 8, March 1965.

[42] A. Koelle, S. Depp, and R. Freyman, "Short-range radio-telemetry for electronic identification, using modulated RF backscatter," *Proceedings of the IEEE*, vol. 63, no. 8, pp. 1260 – 1261, August 1975.

[43] U. Karthaus and M. Fischer, "Fully integrated passive UHF RFID transponder IC with 16.7-μW minimum RF input power," *IEEE Journal of Solid-State Circuits*, vol. 38, no. 10, pp. 1602–1608, October 2003.

[44] K. Finkzenzeller, *RFID Handbook*, 2nd ed. The Atrium, Southern Gate, Chichester, West Sussex PO19 8SQ, England: John Wiley & Sons Ltd, 2003.

[45] R. Want, "Enabling ubiquitous sensing with RFID," *Computer*, vol. 37, no. 4, pp. 84–86, April 2004.

[46] A. Sample, D. Yeager, P. Powledge, A. Mamishev, and J. Smith, "Design of an RFID-based battery-free programmable sensing platform," *IEEE Transactions on Instrumentation and Measurement*, vol. 57, no. 11, pp. 2608–2615, Nov. 2008.

[47] D. Yeager, F. Zhang, A. Zarrasvand, N. George, R. Daniel, and B. Otis, "A 9μA, addressable Gen2 sensor tag for biosignal acquisition," *IEEE Journal of Solid-State Circuits*, vol. 45, no. 10, pp. 2198–2209, Oct. 2010.

[48] Y. Maguire and R. Pappu, "An optimal Q-algorithm for the ISO 18000-6C RFID protocol," *IEEE Transactions on Automation Science and Engineering*, vol. 6, no. 1, pp. 16–24, January 2009.

[49] M. Anderson, "RFID chips gain computing skills," *IEEE Spectrum*, vol. 46, no. 5, p. 15, May 2009.

[50] J. Hollerman, D. Yeager, R. Prasad, J. Smith, and B. Otis, "NeuralWISP: an energy-harvesting wireless neural interface with 1-m range," in *IEEE Biomedical Circuits and Systems Conference*, November 2008, pp. 37–40.

[51] V. T. Talla, M. Buettner, D. Wetherall, and J. Smith, "Hybrid analog-digital backscatter platform with high data rate, battery-free sensing," *IEEE Topical Meeting on Wireless Sensors and Sensor Networks (WiSNET)*, January 2013.

[52] V. Talla and J. Smith, "Hybrid analog-digital backscatter: A new approach for battery-free sensing," in *2013 IEEE International Conference on RFID*, May 2013 (In Press).

[53] J. G. Lee, D. Jung, J. Chu, S. J. Hwang, J. K. Kim, J. Ku, and S. W. Kim, "Applying passive RFID system to wireless headphones for extreme low power consumption," in *Proceedings of the 45th annual Design Automation Conference*. New York, NY, USA: ACM, April 2008, pp. 486–491.

[54] P. Mohseni, K. Najafi, S. Eliades, and X. Wang, "Wireless multichannel biopotential recording using an integrated FM telemetry circuit," *IEEE Transactions on Neural Systems and Rehabilitation Engineering*, vol. 13, no. 3, pp. 263 – 271, September 2005.

[55] N. Ando, I. Shimoyama, and R. Kanzaki, "A dual-channel FM transmitter for acquisition of flight muscle activities from the freely flying hawkmoth, *agrius convolvuli*," *Journal of Neuroscience Methods*, vol. 115, no. 2, pp. 181 – 187, 2002.

[56] D. Hogg, "Fun with the Friis free-space transmission formula," *IEEE Antennas and Propagation Magazine*, vol. 35, no. 4, pp. 33–35, August 1993.

[57] P. Nikitin and K. Rao, "Theory and measurement of backscattering from RFID tags," *IEEE Antennas and Propagation Magazine*, vol. 48, no. 6, pp. 212–218, 2006.

[58] K. Kurokawa, "Power waves and the scattering matrix," *IEEE Transactions on Microwave Theory and Techniques*, vol. 13, no. 2, pp. 194 – 202, March 1965.

[59] P. Nikitin, K. Rao, and R. Martinez, "Differential RCS of RFID tag," *Electronics Letters*, vol. 43, no. 8, pp. 431 – 432, April 2007.

[60] A. Bletsas, A. G. Dimitriou, and J. Sahalos, "Improving backscatter radio tag efficiency," *IEEE Transactions on Microwave Theory and Techniques*, vol. 58, no. 6, pp. 1502 – 1509, June 2010.

[61] C.-C. Yen, A. Gutierrez, D. Veeramani, and D. van der Weide, "Radar cross-section analysis of backscattering RFID tags," *IEEE Antennas and Propagation Letters*, vol. 6, pp. 279–281, 2007.

[62] S. Shrestha, M. Balachandran, M. Agarwal, L.-H. Zou, and K. Varahramyan, "A method to measure radar cross section parameters of antennas," *IEEE Transactions on Antennas and Propagation*, vol. 56, no. 11, pp. 3494 – 3500, Nov. 2008.

[63] J. Ahn, H. Jang, H. Moon, J.-W. Lee, and L. Bomson, "Inductively coupled compact RFID tag antenna at 910 MHz with near-isotropic radar cross-section (RCS) patterns," *IEEE Antennas and Wireless Propagation Letters*, vol. 6, pp. 518 – 520, 2007.

[64] P. Nikitin, K. Rao, S. Lam, V. Pillai, R. Martinez, and H. Heinrich, "Power reflection coefficient analysis for complex impedances in RFID tag design," *IEEE Transactions on Microwave Theory and Techniques*, vol. 53, no. 9, pp. 2721–2725, Sept. 2005.

[65] J. G. Proakis and M. Salehi, *Communication Systems Engineering*, 2nd ed. Upper Saddle River, New Jersey: Prentice-Hall, Inc., 2002.

[66] D. Dobkin, *The RF in RFID: passive UHF RFID in practice*. Elsevier, Inc., 2007.

[67] K. Rao, P. Nikitin, and S. Lam, "Impedance matching concepts in RFID transponder design," in *Fourth IEEE Workshop on Automatic Identification Advanced Technologies, 2005.*, 2005, pp. 39 – 42.

[68] J. Griffin and G. Durgin, "Complete link budgets for backscatter-radio and RFID systems," *IEEE Antennas and Propagation Magazine*, vol. 51, no. 2, pp. 11–25, April 2009.

[69] P. Nikitin and K. Rao, "Antennas and propagation in UHF RFID systems," in *2008 IEEE International Conference on RFID*, April 2008, pp. 277–288.

[70] D. Arnitz, U. Muehlmann, and K. Witrisal, "Characterization and modeling of UHF RFID channels for ranging and localization," *IEEE Transactions on Antennas and Propagation*, vol. 60, no. 5, pp. 2491 – 2501, May 2012.

[71] ——, "Wideband characterization of backscatter channels: Derivations and theoretical background," *IEEE Transactions on Antennas and Propagation*, vol. 60, no. 1, pp. 257–266, January 2012.

[72] G. Li, D. Arnitz, R. Ebelt, U. Muehlmann, K. Witrisal, and M. Vossiek, "Bandwidth dependence of CW ranging to UHF RFID tags in severe multipath environments," in *2011 IEEE International Conference on RFID*, 2011, pp. 19–25.

[73] J. Griffin and G. Durgin, "Multipath fading measurements at 5.8 GHz for backscatter tags with multiple antennas," *IEEE Transactions on Antennas and Propagation*, vol. 58, no. 11, pp. 3693 – 3700, November 2010.

[74] ——, "Link envelope correlation in the backscatter channel," *IEEE Communications Letters*, vol. 11, no. 9, pp. 735 – 737, September 2007.

[75] D. Arnitz and M. S. Reynolds, "Backscatter MIMO wireless power transfer optimization for mobile devices," *IEEE Microwave Theory and Techniques Letters*, (to appear).

[76] L. W. Mayer, M. Wrulich, and S. Caban, "Measurements and channel modeling for short range indoor UHF applications," in *Proceedings of the 1st IEEE European Conference on Antennas and Propagation*, November 2006, pp. 1–5.

[77] R. A. Shafik, S. Rahman, R. Islam, and N. S. Ashraf, "On the error vector magnitude as a performance metric and comparative analysis," in *2006 International Conference on Emerging Technologies*, 2006, pp. 27–31.

[78] "IEEE standard wireless LAN medium access control (MAC) and physical layer (PHY) specifications," *IEEE Std 802.11-2007*, 2007.

[79] M. Winkler, T. Faseth, H. Arthaber, and G. Magerl, "An UHF RFID tag emulator for preceise emulation of the physical layer," in *2010 European Wireless Technology Conference (EuWIT)*, Sept. 2010, pp. 273–276.

[80] J.-P. Curty, M. Declercq, C. Dehollain, and N. Joehl, *Design and Optimization of passive UHF RFID Systems*. Springer, 2007 (Chapters 3, 5, 6).

[81] Monza 4 tag chip datasheet. Online. Impinj Inc. [Online]. Available: http://www.impinj.com/Documents/Tag_Chips/Monza_4_Tag_Chip_Datasheet/

[82] Y. He, R. Yuan, X. Ma, and J. Li, "The IEEE 802.11 power saving mechanism: An experimental study," in *IEEE Wireless Communications and Networking Conference, 2008. WCNC 2008*, 2008, pp. 1362 – 1367.

[83] S. Qureshi, "Adaptive equalization," *Proceedings of the IEEE*, vol. 73, no. 9, pp. 1349 – 1387, Sept. 1985.

[84] D. Arnitz and M. S. Reynolds, "Wireless power transfer optimization for nonlinear passive backscatter devices," in *2013 IEEE International Conference on RFID*. Orlando, Florida USA: (In Press), May 2013.

[85] R. M. Olberg, A. H. Worthington, and K. R. Venator, "Prey pursuit and interception in dragonflies," *J Comp Physiol A*, vol. 186, no. 2, pp. 155–62, Feb 2000.

[86] T. A. Szuts, V. Fadeyev, S. Kachiguine, A. Sher, M. V. Grivich, M. Agrochao, P. Hottowy, W. Dabrowski, E. V. Lubenov, A. G. Siapas, N. Uchida, A. M. Litke, and M. Meister, "A wireless multi-channel neural amplifier for freely moving animals," *Nature Neuroscience*, vol. 14, no. 2, pp. 263–U363, Feb. 2011.

[87] R. E. Hampson, V. Collins, and S. A. Deadwyler, "A wireless recording system that utilizes Bluetooth technology to transmit neural activity in freely moving animals," *Journal of Neuroscience Methods*, vol. 182, no. 2, pp. 195–204, Sept. 2009.

[88] E. Greenwald, M. Mollazadeh, C. Hu, W. Tang, E. Culurciello, and N. V. Thakor, "A VLSI neural monitoring system with ultra-wideband telemetry for awake behaving subjects," *IEEE Transactions On Biomedical Circuits and Systems*, vol. 5, no. 2, pp. 112–119, Apr. 2011.

[89] G. Kutsch, G. Schwarz, H. Fischer, and H. Kautz, "Wireless transmission of muscle potentials during free flight of a locust," in *Journal of Experimental Biology*, vol. 185, 1993, pp. 367 – 373.

[90] H. Fischer, H. Kautz, and W. Kutsch, "A radiotelemetric 2-channel unit for transmission of muscle potentials during free flight of the desert locust, schistocerca gregaria," *Journal of Neuroscience Methods*, vol. 64, no. 1, pp. 39 – 45, 1996.

[91] Y. Kuwana, N. Ando, R. Kanzaki, and I. Shimoyama, "A radiotelemetry system for muscle potential recordings from freely flying insects," in *Proceedings of the IEEE BMES/EMBS Conference*, vol. 2, October 1999, p. 846.

[92] A. Nieder, "Miniature stereo radio transmitter for simultaneous recording of multiple single-neuron signals from behaving owls," *Journal of Neuroscience Methods*, vol. 101, no. 2, pp. 157 – 164, 2000.

[93] P. Mohseni, K. Nagarajan, B. Ziaie, K. Najafi, and S. Crary, "An ultralight biotelemetry backpack for recording EMG signals in moths," *IEEE Transactions on Biomedical Engineering*, vol. 48, no. 6, pp. 734 – 737, June 2001.

[94] S. Takeuchi and I. Shimoyama, "A radio-telemetry system with a shape memory alloy microelectrode for neural recording of freely moving insects," *IEEE Transactions on Biomedical Engineering*, vol. 51, no. 1, pp. 133 – 137, January 2004.

[95] Z. Xiao, C. Tang, C. Dougherty, and R. Bashirullah, "A 20μW neural recording tag with supply-current modulated AFE in 0.13μm CMOS," in *Proceedings of the IEEE International Solid-State Circuits Conference*, 2010, pp. 122–123.

[96] M. Lewicki, "A review of methods for spike sorting: the detection and classification of neural action potentials," *Network computation in neural systems*, vol. 9, no. 4, pp. 53–78, 1998.

[97] Z. S. Zumsteg, R. E. Ahmed, G. Santhanam, K. V. Shenoy, and T. H. Meng, "Power feasibility of implantable digital spike-sorting circuits for neural prosthetic systems," *Proceedings of the IEEE Engineering Medical Biology Society*, vol. 6, pp. 4237–40, 2004.

[98] R. Olberg, "Identified target-selective visual interneurons descending from the dragonfly brain," *Journal Of Comparative Physiology A*, vol. 159, pp. 827–840, 1986.

[99] G. De Vita and G. Iannaccone, "Design criteria for the RF section of UHF and microwave passive RFID transponders," *IEEE Transactions on Microwave Theory and Techniques*, vol. 53, no. 9, pp. 2978 – 2990, September 2005.

[100] K. Seemann, G. Hofer, F. Cilek, and R. Weigel, "Single-ended ultra-low-power multistage rectifiers for passive RFID tags at UHF and microwave frequencies," in *2006 IEEE Radio and Wireless Symposium*, January 2006, pp. 479–482.

[101] S. Mandal and R. Sarpeshkar, "Low-power CMOS rectifier design for RFID applications," *IEEE Transactions on Circuits and Systems I: Regular Papers*, vol. 54, no. 6, pp. 1177–1188, June 2007.

[102] Federal Communications Commission, "OET bulletin 65: Evaluating compliance with FCC guidelines for human exposure to radiofrequency electromagnetic fields," August 1997.

[103] R. Harrison, "The design of integrated circuits to observe brain activity," *Proceedings of the IEEE*, vol. 96, no. 7, pp. 1203–1216, July 2008.

[104] Datasheet, S9028 circularly polarized RFID panel antenna. Laird Technologies. [Online]. Available: http://www.lairdtech.com/WorkArea/linkit.aspx?LinkIdentifier=id&ItemID=3865

[105] R. Stampfl, "The Nimbus spacecraft and its communication system as of September 1961," *NASA Technical Note D-1422*, 1963.

[106] NOAA Satellite and Information Service, "Polar operational environmental satellite," 2013, [Online; accessed 4-January-2013]. [Online]. Available: http://www.oso.noaa.gov/poes/

[107] M. Bruchanov, "Image communication on short waves," Available online, http://www.sstv-handbook.com, September 2012.

[108] J. Dickson, "On-chip high-voltage generation in MNOS integrated circuits using an improved voltage multiplier technique," *IEEE Journal of Solid-State Circuits*, vol. 11, no. 3, pp. 374–378, June 1976.

[109] S. Thomas, M. Reynolds, and J. Teizer, "Electromagnetic energy harvesting for sensing, communication, and actuation," *Proceedings of the 27th International Association for Automation and Robitics in Construction (ISARC)*, pp. 182–192, 2010.

[110] A. Sample and J. Smith, "Experimental results with two wireless power transfer systems," in *IEEE Radio and Wireless Symposium, 2009. RWS '09.*, January 2009, pp. 16–18.

[111] R. Barnett, J. Liu, and S. Lazar, "A RF to DC voltage conversion model for multi-stage rectifiers in UHF RFID transponders," *IEEE Journal of Solid-State Circuits*, vol. 44, no. 2, pp. 354–370, February 2009.

[112] Y. Yao, J. Wu, Y. Shi, and F. F. Dai, "A fully integrated 900-MHz passive RFID transponder front end with novel zero-threshold RF-DC rectifier," *IEEE Transactions on Industrial Electronics*, vol. 56, no. 7, pp. 2317–2325, July 2009.

[113] C. Boyer and S. Roy, "Coded QAM backscatter modulation for RFID," *IEEE Transactions on Communications*, vol. 60, no. 7, pp. 1925 – 1934, July 2012.

[114] M. Trotter, C. Valenta, G. Koo, B. Marshall, and G. Durgin, "Multi-antenna techniques for enabling passive RFID tags and sensors at microwave frequencies," in *2012 IEEE International Conference on RFID*, April 2012.

[115] M. Philipose, J. Smith, B. Jiang, A. Mamishev, S. Roy, and K. Sundara-Rajan, "Battery-free wireless identification and sensing," *IEEE Pervasive Computing*, vol. 4, no. 1, pp. 37–45, January-March 2005.

[116] D. Holcomb, W. Burleson, and K. Fu, "Power-up SRAM state as an identifying fingerprint and source of true random numbers," *IEEE Transactions on Computers*, vol. 58, no. 9, pp. 1198–1210, September 2009.

[117] S. Thomas, J. Teizer, and M. Reynolds, "Smarthat: A battery-free worker safety device employing passive UHF RFID technology," in *2011 IEEE International Conference on RFID*, April 2011, pp. 85–90.

[118] S. J. Thomas, J. S. Besnoff, and M. S. Reynolds, "Modulated backscatter for ultra-low power upinks from wearable and implantable devices," in *Proceedings of the 2012 ACM workshop on medical communication systems*. ACM, August 2012, pp. 1–6.

[119] K. Gudan, S. Chemishkian, J. J. Hull, M. S. Reynolds, and S. J. Thomas, "Feasibility of wireless sensors using ambient 2.4 GHz RF energy," in *2012 IEEE Sensors*. IEEE, October 2012, pp. 1–4.

[120] M. S. Reynolds and S. J. Thomas, "The blue devil WiSP: Expanding the frontiers of the passive RFID physical layer," in *WISP Summit (in conjunction with ACM SenSys)*, Berkeley, California USA, November 2009.

Biography

Stewart Jennings Thomas was born in Little Rock, Arkansas USA. After a brief stay in Memphis, TN, he moved to Louisville, KY which he considers to be his childhood home. He received the B.S. degree (cum laude) from the University of Louisville in Louisville, KY USA in 2006 and the M.Eng. degree (magna cum laude) from the University of Louisville in 2008. Stewart Thomas received the Ph.D degree from Duke University, Durham, NC USA in 2013 and his dissertation, titled *Modulated Backscatter for Low-Power High-Bandwidth Communication,* was written under the direction of Dr. Matthew S. Reynolds.

While working on his M.Eng degree, Stewart received the ECE Departmental Alumni Award awarded by the J.B. Speed School Alumni Association. At the time of publication of this dissertation, Stewart has authored 2 journal articles [8, 15], 8 peer-reviewed conference proceedings articles [7, 16, 17, 30, 109, 117–119], and a workshop presentation [120].

Stewart has been a student member of the IEEE since 2006, student member of the IEEE MTT society since 2008, former student member of the IEEE Communications Society (2009 – 2010), and member of Eta Kappa Nu since 2006. He plans on continuing work at Duke University as a Postdoctoral Associate.